Technical Physics Letters, Vol. 26, No. 12, 2000, pp. 1027–1028. Translated from Pis'ma v Zhurnal Tekhnicheskoĭ Fiziki, Vol. 26, No. 23, 2000, pp. 1–4.

The Effect of Periodic Bending on the X-ray Beam Channeling

T. A. Bobrova and L. I. Ognev

Nuclear Fusion Institute, Kurchatov Institute of Atomic Energy,
State Scientific Center of the Russian Federation, Moscow, 123182 Russia;
e-mail: ognev@nfi.kiae.ru

Received April 4, 2000

Abstract—The X-ray radiation passage through randomly arranged narrow (submicron) channels in a solid was studied by the method of numerical modeling taking into account the diffraction and reduced coherency effects. It was found that the X-ray transmission is markedly deteriorated in the channels subject to periodic deformation. The randomization effects are interpreted within the framework of the statistical theory of X-ray scattering in a rough transitional layer. An anomaly in the energy dependence of the X-ray transmission through a thin (1620 Å) Cr/C/Cr channel observed for a 17 keV mode is explained by small periodic bending perturbations and related interferences in the structure. *© 2000 MAIK "Nauka/Interperiodica".*

In contrast to the case of multimode waveguides for the soft X-ray radiation [3], we have considered a limited number of modes at very small glancing angles. The X-ray mode passage can be described in terms of the "parabolic" equation for the electric field vector $A(x, z)$ [4]:

$$2ik\frac{\partial A}{\partial z} = \Delta_\perp A + k^2\frac{\varepsilon - \varepsilon_0}{\varepsilon_0}A, \qquad A(x, z = 0) = A_0(x), \tag{1}$$

where z and x are the coordinates measured along and across the channel (the consideration is restricted to the case of 2D channels) and $k = \sqrt{\varepsilon_0}\frac{\omega}{c}$ is the wavenumber. In this case, the quantities ε_0 and ε_1 represent the dielectric permittivities of the "channel" and "wall," respectively. According to the model adopted [4], the scattering at large angles is ignored. Evolution of the channeled X-ray beam was calculated by direct numerical integration of the "parabolic" equation as described in [5]. The dielectric permittivity of a rough channel surface with random shape $x = \xi(z)$ was described by the function $\varepsilon(x, z) = \varepsilon_1 + (\varepsilon_0 - \varepsilon_1)H(x - \xi(z))$, where $H(x)$ is a stepwise function. The roughness heights were assumed to be distributed according to the normal law.

An analytic description of attenuation of the coherent X-ray beam component as a result of scattering on the channel roughnesses can be obtained by statistically averaging Eq. (1). It can be shown that attenuation of the lower channeled modes as a result of the incoherent scattering is proportional to σ [6]:

$$\beta_{\text{scat}} \sim k^2(\varepsilon_0 - \varepsilon_1)^2\sigma\int_{-\infty}^{\infty} dz'\int_{-\infty}^{0}\exp(-\xi^2/2)\,d\xi \times \int_0^{\frac{-R(z')\xi}{(1-R^2(z'))^{1/2}}}\exp(-\eta^2/2)d\eta,$$

where $R(z)$ is the autocorrelation coefficient.

The results of experiments in a Cr/C/Cr channel with a length of $L = 3$ mm and a carbon layer thickness of $d = 1620$ Å [1] showed a nonmonotonic energy dependence for the mode "0" transmission (Fig. 1,

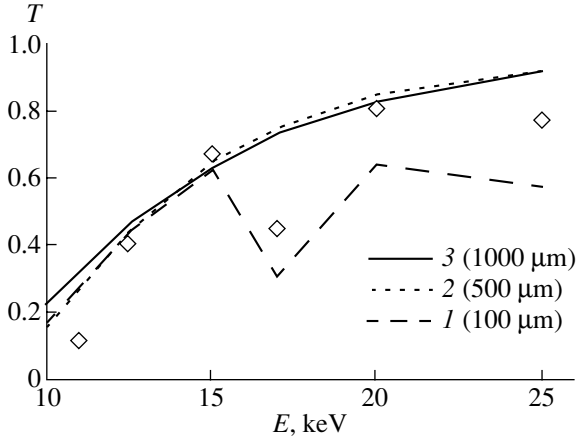

Fig. 1. Plots of the X-ray mode "0" transmission versus energy E for a Cr/C/Cr channel with $L = 3$ mm, $d = 1620$ Å, $\sigma = 0$, and the deformation amplitude $a = 120$ Å and period $\Lambda = 100$ (*1*), 500 (*2*), and 1000 μm (*3*). Rhomb symbols present the experimental data taken from [1].

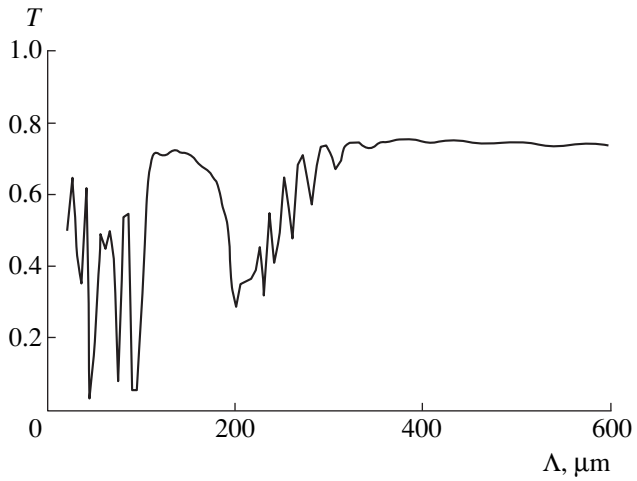

Fig. 2. A plot of the X-ray mode "0" transmission at E = 17 keV versus the deformation period Λ in a Cr/C/Cr channel with L = 3 mm, d = 1620 Å, σ = 0, and the deformation amplitude a = 120 Å.

rhomb symbols); note that the interface roughness was assumed not to exceed σ ~10 Å [1].

We have performed direct numerical modeling of the X-ray beam passage using Eq. (1) for the modes "0" and "1" and determined the transmission as function of the roughness amplitude. Taking into account the channel roughness decreased the transmission of the mode with E = 17 keV mode only by 1.3 and 5% for σ = 10 and 20 Å, respectively, which cannot explain the drop in the experimental plot (Fig. 1) even for much worse interface characteristics (taking into account that the transmission attenuation coefficient grows linearly with the roughness height).

In order to explain the anomalous energy dependence of the 17-keV mode transmission observed in the Cr/C/Cr channel, we took into account the possible periodic perturbations of the channel [2]. The results of this analysis are also presented in Fig. 1 for the deformation with an amplitude of a = 120 Å and a period of Λ = 100 (curve *1*), 500 (*2*) and 1000 μm (*3*).

Figure 2 shows a plot of the X-ray transmission at E = 17 keV versus the deformation period Λ for a = 120 Å in a channel without roughness (as indicated above, this factor is insignificant). As seen, there are several resonances in the region of short periods Λ. Note that the results depicted in Figs. 1 and 2 look much like the pattern observed upon a strong reconstruction of the wavefunction of channeled electrons in superlattices [5].

Thus, the drop in the X-ray transmission at E = 17 keV observed ion [1] and depicted in Fig. 1 can be explained by periodic perturbations in the Cr/C interface and the interference of the resulting higher wave modes, which lead to increase in the X-ray radiation losses.

REFERENCES

1. W. Jark, S. Di Fonzo, G. Soullie, *et al.*, J. Alloys Compd. **286**, 9 (1999).
2. T. A. Bobrova and L. I. Ognev, in *Abstracts of the International Conference Current Status of Synchrotron Radiation in the World, Moscow, 2000*, p. 54.
3. S. V. Kukhlevsky, G. Lubkovics, K. Negrea, and L. Kozma, Pure Appl. Opt. **6**, 97 (1997).
4. T. A. Bobrova and L. I. Ognev, Pis'ma Zh. Éksp. Teor. Fiz. **69**, 686 (1999) [JETP Lett. **69**, 734 (1999)].
5. T. A. Bobrova and L. I. Ognev, Phys. Status Solidi B **203** (2), R11 (1997).
6. L. I. Ognev, Pis'ma Zh. Tekh. Fiz. **26** (2), 47 (2000) [Tech. Phys. Lett. **26**, 67 (2000)].

Translated by P. Pozdeev

Technical Physics Letters, Vol. 26, No. 12, 2000, pp. 1029–1031. Translated from Pis'ma v Zhurnal Tekhnicheskoĭ Fiziki, Vol. 26, No. 23, 2000, pp. 5–10.

A Coherent Trough in the Envelope of a Signal Formed by the Interferometer with a Partially Coherent Radiation Source

M. I. Lobachev*, D. V. Lyakin, and V. P. Ryabukho*,****

** Institute of Precision Mechanics and Control, Russian Academy of Sciences, Saratov, 410028 Russia*

*** Saratov State University, Saratov, 410026 Russia;*

e-mail: rvp@sgu.ssu.runnet.ru

Received June 9, 2000

Abstract—When a mixed radiation from physically different sources with substantially different widths of spectral lines is used in an interferometer, a single trough can appear under certain conditions in the envelope of the time-dependent interference signal. This trough can be used as a measurement signal. © *2000 MAIK "Nauka/Interperiodica".*

A mixed radiation from two or more light sources with slightly different center frequencies is used in the low-coherence interferometry to broaden the radiation spectrum contour and accordingly narrow the temporal coherence function and sharpen the interference signal [1, 2]. However, if the center frequencies differ by more than the spectrum contour width and the spectrum of mixed radiation contains distinct local maxima, the envelope of the interference signal may exhibit oscillations because the temporal coherence function of the radiation with such spectrum has an oscillating character [3]. In interferometers with substantially different arms, including laser interferometers, these oscillations of the signal envelope represent a disturbing factor [4]; however, they can be used in measurements [5].

The purpose of this study was to determine conditions required for the formation of a single minimum (trough) in the envelope of the time-dependent interference signal.

Under conditions of the mutual spatial coherence of the interfering waves, we can write the following simplified expression for the interferometer signal $u_p(\Delta t)$ (e.g., for the Michelson interferometer):

$$u_p(\Delta t) \sim I_R + I_S + 2|\Gamma(\Delta t)|\cos(\bar{\omega}\Delta t + \alpha), \qquad (1)$$

where I_R, I_S, and $\Gamma(\Delta t)$ are the wave intensities and the temporal coherence function of the interfering waves, respectively; $\alpha = \arg\Gamma(\Delta t)$; and $\bar{\omega}$ is the center frequency of the radiation spectrum. The $|\Gamma(\Delta t)|$ function plays the role of the interference signal envelope.

For the modulus of the temporal coherence function of a mixed radiation generated by two physically different and, consequently, mutually incoherent sources, we can write an expression that (this is important to note) has the form of the interference equation:

$$|\Gamma(\Delta t)|^2 = |\Gamma_1(\Delta t)|^2 + |\Gamma_2(\Delta t)|^2 + 2|\Gamma_1(\Delta t)||\Gamma_2(\Delta t)|\cos(\Delta\omega_{12}\Delta t + \Delta\Phi). \qquad (2)$$

Here, $\Gamma_1(\Delta t)$ and $\Gamma_2(\Delta t)$ are the temporal coherence functions for radiations of the two sources, $\Delta\omega_{12} = \bar{\omega}_1 - \bar{\omega}_2$ is the difference of frequencies of these radiations, and $\Delta\Phi$ is the phase difference for the waves corresponding to the center frequencies of the mixed radiations.

If $\Delta\Phi = 0$ and $2\pi/\Delta\omega_{12} < \min(\tau_{s1}, \tau_{s2})$, where τ_{s1} and τ_{s2} are the coherence times of the considered radiations, there appear local minima in the signal envelope $|\Gamma(\Delta t = 0)|$. If the parameters τ_{s1} and τ_{s2} are substantially different, a trough to the zero level in the function $|\Gamma(\Delta t)|$ can only be formed for a single pair of symmetric minima when

$$|\Gamma_1(\Delta t)|\exp(i\bar{\omega}_1\Delta t) = -|\Gamma_2(\Delta t)|\exp(i\bar{\omega}_2\Delta t).$$

In order to obtain a single trough over the whole interval Δt in which the interference signal may exist, with $|\Delta t| \le \max(\tau_{s1}, \tau_{s2})$, the phase shift $\Delta\Phi$ must be nonzero and the following condition must be satisfied:

$$2\min(\tau_{s1}, \tau_{s2}) < 2\pi/\Delta\omega_{12}. \qquad (3)$$

This inequality means that the oscillation period exceeds the total width of the correlation function for a radiation with the smallest correlation length τ_s. If $\Delta\Phi = \pi$, the trough in the interference signal envelope must be observed for a zero path difference ($\Delta t = 0$).

In order to verify experimentally the possibility of observing a single trough in the interference signal, we used a Michelson interferometer with an HLMP-8103 red light–emitting diode ($\bar{\lambda}_1 = 0.6354$ μm) and a He–Ne laser ($\bar{\lambda}_2 = 0.6328$ μm) as light sources. The

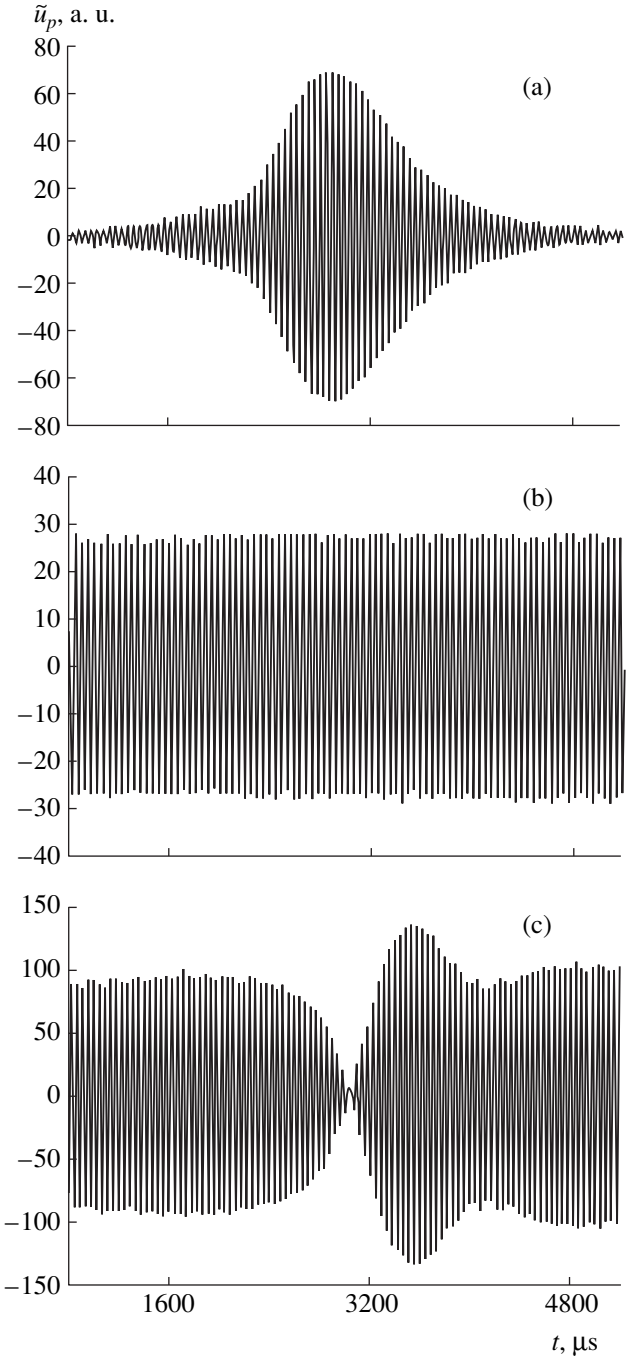

Fig. 1. Experimental digital oscillograms of the signal obtained from a Michelson interferometer using (a) a low-coherence (broadband-spectrum) LED radiation, (b) laser radiation, and (c) mixed radiation.

halfwidth of the light-emitting diode (LED) radiation spectrum was $\Delta\lambda_1 \approx 13$ nm and the corresponding coherence length was $l_{s1} = c\tau_{s1} \approx 7$ μm. In order to create the time-dependent interferometer output signal, we used a reference mirror vibrating with large amplitude $l_a > 2l_{s1}$.

Figure 1 presents experimental digital oscillograms of a variable component of the interferometer signal $\tilde{u}_p$, which were obtained using (a) only the LED radiation, (b) the laser radiation, and (c) a mixed radiation of both LED and the laser. Relationships between the difference of wavelengths (frequencies) of the two sources and the coherence length (time) of the LED radiation satisfy condition (3) necessary to observe a single trough in the signal envelope.

A nonzero phase shift $\Delta\Phi$ for the waves with different frequencies can form in the interferometer only as a result of different optical path lengths for these waves. This difference may be caused by the presence of a layer of dispersive medium in one of the interferometer arms. For example, in order to obtain phase difference $\Delta\Phi = \pi$ in a K-8 glass with the dispersion $dn/d\lambda = -3.4 \times 10^{-5}$ nm^{-1} at $\bar{\lambda} = 0.63$ μm, it would suffice to take a layer with a thickness of $h \approx 140$ μm. Here, we take into account the fact that the light propagating in the Michelson interferometer passes twice through the layer. Note that this layer may appear because of inaccuracy in the manufacturing of the beam-splitting cube, which was observed in the experiment.

The trough halfwidth is determined by the difference between center frequencies of the mixed radiations and can be substantially smaller than the halfwidth of the envelope of the radiation with a shorter coherence length (see Figs. 1a and 1b). This specific feature of the signal with trough can be used to increase the precision of the interferometric determination of the position of an object. One can also measure the phase difference $\Delta\Phi$ and, consequently, determine the position of the trough in the interference signal depending on the optical thickness of a dispersive medium in the interferometer and use this function in high-precision interferometric measurements. If $\Delta\Phi$ changes by $\delta(\Delta\Phi)$, the trough shifts by $\delta m = \delta(\Delta\Phi)\bar{\omega}/2\pi\Delta\omega_{12}$ on the scale of interference signal oscillations, where $\bar{\omega} = (\bar{\omega}_1 + \bar{\omega}_2)/2$ is the center frequency of the mixed radiation.

A single trough in the interference signal envelope can be obtained not only by mixing radiations from two physically different sources but by means of the interferometric transformation of the radiation spectrum created by a wideband source as well [6]. For this purpose, it is necessary to implement a mutual wave delay in the preliminary (illuminating) interferometer (e.g., in the Michelson interferometer), such that it would be comparable to the coherence time $\Delta t \approx \tau_s$ obtained at a phase difference of π rad for the center frequencies in the initial radiation spectrum.

Since the interferometer considered above implements the noncoherent mixing of two interference signals with slightly different oscillation periods in a photoreceiver, the formation of a trough in the envelope of the resulting signal can be considered as a result of beatings of these signals. Consequently, a similar result can be obtained by electrically mixing the photoelectric

signals from two interferometers with low-coherence radiation that are synchronized by the motion of a common reference mirror. In this case, it is not necessary to use radiations with different frequencies: in order to obtain interference oscillations of signals with different periods, it would suffice to introduce a small angular detuning into the illumination direction in one of the interferometers. This system of two interferometers will play the role of an "optical balance" providing a response with a submicron sensitivity to the relative variation of the difference of optical paths in the interferometers.

Acknowledgments. This work was supported by the Russian Foundation for Basic Research (project no. 00-15-96667) and the "Leading Scientific Schools of the Russian Federation" Program.

REFERENCES

1. J. M. Schmitt, S. L. Lee, and K. M. Yung, Opt. Commun. **142**, 203 (1997).
2. D. N. Wang, Y. N. Ning, K. T. V. Grattan, *et al.*, Appl. Opt. **33**, 7326 (1994).
3. I. G. Steward, *Fourier Optics: an Introduction* (Ellis Horwood, Chichester, 1983; Mir, Moscow, 1985).
4. O. I. Kotov, L. B. Liokumovich, V. M. Nikolaev, *et al.*, Pis'ma Zh. Tekh. Fiz. **23** (20), 61 (1997) [Tech. Phys. Lett. **23**, 801 (1997)].
5. A. N. Golubev and A. M. Chekhovsky, Opt. Eng. **36** (8), 2229 (1997).
6. M. Born and É. Wol'f, *Principles of Optics* (Pergamon, Oxford, 1969; Nauka, Moscow, 1973).

Translated by A. Kondrat'ev

Technical Physics Letters, Vol. 26, No. 12, 2000, pp. 1032–1033. Translated from Pis'ma v Zhurnal Tekhnicheskoĭ Fiziki, Vol. 26, No. 23, 2000, pp. 11–15.

The Ablation Threshold in Amorphous Diamondlike Carbon Films Exposed to an ArF Excimer Laser Radiation

N. A. Kaliteevskaya, O. I. Kon'kov, E. I. Terukov, and R. P. Seĭsyan

Ioffe Physicotechnical Institute, Russian Academy of Sciences, St. Petersburg, 194021 Russia

Received July 13, 2000

Abstract—An experimental study of the laser-induced ablation threshold in amorphous diamondlike carbon films is reported. The aim is to assess the possibility of using the material as a photoresist in vacuum-ultraviolet laser lithography. Grown on silicon substrates, 10-nm films were irradiated by 20-ns pulses of a 193-nm ArF excimer laser with variable pulse energy per unit area E_p. It is found that the etch rate is very low if $E_p < 20$ mJ/cm^2, whereas a single pulse suffices to remove the film completely if $E_p = 60$ mJ/cm^2. This is attributed to an increase in the thermal ablation component. © *2000 MAIK "Nauka/Interperiodica".*

Further progress in microelectronics necessitates developing novel techniques to transfer patterns from masks to a substrate surface. With photolithography, it seems promising to employ ablation, that is, the removal of a photoresist by means of intense ultraviolet radiation, typically that produced by an excimer laser [1]. An advantage of this strategy is that it requires no chemical processing of the resist after exposure, the material being directly removed by irradiation, so that the photolithographic process entails fewer steps.

There are different types of ablation. The photoablation runs at a modest incident intensity, such that the material disintegrates due to the breakage of chemical bonds under the action of ultraviolet radiation quanta.

The photothermal ablation occurs when the incident intensity is so high that the material undergoes sublimation as a result of instantaneous local heating.

For the laser-induced ablation lithography to be successful, it is essential that a proper material would serve as a photoresist. Recent years have seen an extensive search for candidate materials. In particular, attention was given to glassy chalcogenide semiconductors [1, 2] and diamondlike films [3].

This experimental study aimed at establishing the ablation threshold in amorphous diamondlike films processed with a pulsed ArF excimer laser operating at a wavelength of 193 nm.

Diamondlike carbon films are remarkable for their chemical inertness and high values of hardness, optical transmittance, and ohmic resistance. They are compatible with almost any substrate material and can be deposited onto a large area at modest temperatures. For this reason, the diamondlike carbon films are preferable to diamond films in some cases. Also, the former can be synthesized by simple and inexpensive techniques [4]. The experiment reported here was carried out on films of amorphous hydrogenated carbon (α-C:H). Although the α-C:H film synthesis and physical properties are widely covered in the literature, there is still an insufficient understanding of how the structure of these films is formed and how it is connected with the observed physical properties. Depending on the deposition technique, the α-C:H films may contain considerable amounts of fixed and free hydrogen. Thus, the hydrogen content is a key factor governing the structure and physical properties of the films [5–7].

In our experiment, α-C:H films with a thickness of 0.01–0.02 μm were synthesized by decomposition of a 10%CH_4 + Ar/H_2 gas mixture in a glow-discharge plasma, with the products deposited onto substrates made of a KDB-7.5 crystalline silicon. The films were exposed to 20-ns pulses of a vacuum-ultraviolet laser radiation. A beam-splitting plate was used to direct 6% of laser power to an IMO power meter, whereas the main portion was incident onto a specimen under study, having passed through a rectangular diaphragm (Fig. 1).

Irradiated specimens were examined with a DEKTAK 3030 profilometer with a metal point scanning over the sample surface. The instrument provided images of the surface topography after ablation so that we were able to estimate the depth to which the material was removed.

It was established that the dose necessary to remove the surface film essentially depends on the incident UV radiation intensity. Figure 2 shows the etch rate $\delta h/\delta H$ as a function of the incident pulse energy per unit area E_p, where h is the film thickness and H is the irradiation dose. It is seen that, if $E_p < 20$ mJ/cm^2, then $\delta h/\delta H < 10^{-6}$ cm^3/mJ. With such a low etching efficiency, more

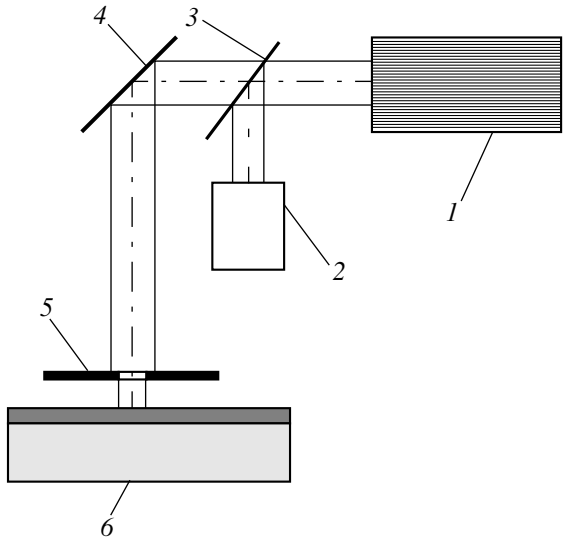

Fig. 1. Experimental setup: (*1*) excimer laser; (*2*) power meter; (*3*) beam-splitting plate; (*4*) rotational mirror; (*5*) diaphragm; and (*6*) specimen (diamondlike carbon film on silicon substrate).

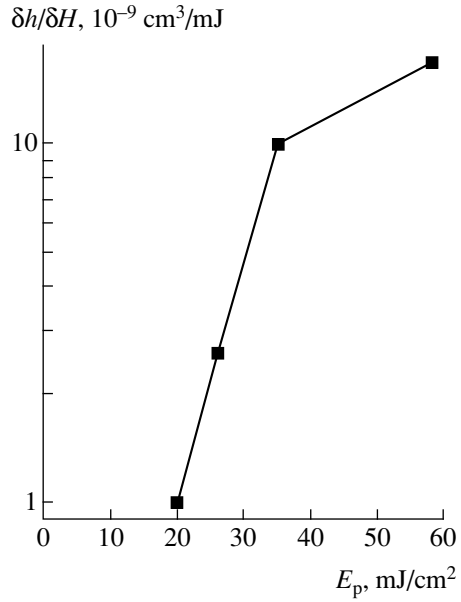

Fig. 2. Etching efficiency vs. incident pulse energy per unit area.

than 50 pulses are required to remove the film. With E_p being raised, the etch rate grows exponentially:

$$\delta h/\delta H = A\exp(E_p/E_{th}), \quad (1)$$

where E_{th} is the threshold pulse energy per unit area (E_{th} = 6.5 mJ/cm^2) and A is a constant equal to 4.5×10^{-11} cm^3/mJ. As soon as E_p reaches 40 mJ/cm^2, a kink appears in the graph. A similar pattern of the etching efficiency variation was observed in [1], where it had been found that the kink indicates the transition from photo to thermal ablation. Finally, at E_p = 58 mJ/cm^2, a single pulse suffices to remove the film completely. Under these conditions, the substrate can be transported continuously, since the pulse width is as small as 20 ns. Thus, for a constant pulse duration of 20 ns the dose required to remove a 10-nm film drops by a factor of 17 when the E_p value is increased from 20 to 58 mJ/cm^2.

Acknowledgments. The support of the Russian Foundation for Basic Research is gratefully acknowledged.

REFERENCES

1. E. G. Barash, A. Yu. Kabin, V. M. Lyubin, and R. P. Seĭsyan, Zh. Tekh. Fiz. **62** (3), 106 (1992) [Sov. Phys. Tech. Phys. **37**, 292 (1992)].
2. L. G. Gladysheva, N. A. Kaliteevskaya, R. P. Seĭsyan, and D. V. Smirnov, Pis'ma Zh. Tekh. Fiz. **22** (15), 91 (1996) [Tech. Phys. Lett. **22**, 640 (1996)].
3. M. Rothschild and D. J. Ehrlich, J. Vac. Sci. Technol. B **5** (1), 389 (1987).
4. I. O. Kon'kov, I. N. Trapeznikova, and E. I. Terukov, Fiz. Tekh. Poluprovodn. (St. Petersburg) **28** (8), 1406 (1994) [Semiconductors **28**, 791 (1994)].
5. A. Callegari, A. T. Pomerene, H. J. Hovel, *et al.*, J. Vac. Sci. Technol. B **11** (6), 2697 (1993).
6. I. O. Kon'kov, I. N. Kapitonov, I. N. Trapeznikova, and E. I. Terukov, Pis'ma Zh. Tekh. Fiz. **23** (1), 3 (1997) [Tech. Phys. Lett. **23**, 9 (1997)].
7. O. I. Kon'kov, E. I. Terukov, and I. N. Trapeznikova, Fiz. Tekh. Poluprovodn. (St. Petersburg) **30** (12), 2183 (1996) [Semiconductors **30** (12), 1138 (1996)].

Translated by A. Sharshakov

Technical Physics Letters, Vol. 26, No. 12, 2000, pp. 1034–1037. Translated from Pis'ma v Zhurnal Tekhnicheskoĭ Fiziki, Vol. 26, No. 23, 2000, pp. 16–23.

Analytical Solution of a Gas Sliding Problem Using a New Kinetic Equation

A. V. Latyshev and A. A. Yushkanov

Moscow State Pedagogical University, Moscow, Russia;

e-mail: latyshev@orc.ru

Received April 25, 2000

Abstract—A new kinetic equation leading to a correct (true) value of the Prandtl number (Pr) is derived. Based on this equation, an analytical solution to the gas sliding problem is obtained and the isothermal and thermal sliding velocities are calculated, the corresponding formulas being derived in an explicit form. The results of numerical calculations indicate that the proposed model is compatible with the existing theories: the results obtained for the thermal sliding fall between data calculated within the framework of the Bhatnagar–Gross–Kruck (BGK) model with constant collisional frequency and the BGK model with constant mean free path. The new model can be referred to as a model with an intermediate character of the collisional frequency as the function of the velocity of molecules. An important advantage of the proposed model is the presence of a parameter that may correspond to the true Prandtl number. The values of the sliding coefficients K_{sl} and K_{Tsl} in this kinetic model possess essentially a new qualitative status. Indeed, the "old" quantities were obtained using a model with incorrect Prandtl number and had to be recalculated for the correct Pr value, this procedure introducing an element of uncertainty. The results obtained using the proposed model, involving the correct Pr value, are free of this disadvantage. © *2000 MAIK "Nauka/Interperiodica".*

Let us consider a gas filling the halfspace $x > 0$ over a flat wall in a Cartesian coordinate system with the x axis perpendicular to the wall and (y, z) plane coinciding with the wall surface. The gas motion is set by a mass velocity gradient g_v along the y axis determined at a large distance from the wall. Once set, the mass velocity gradient induces the gas flow along the wall, this motion referred to as isothermal. The gas flow is considered in the absence of a tangential pressure gradient; the mass velocity has a single tangential component that varies by a linear law at a large distance from the wall. Deviation from the linear variation takes place near the wall, in the layer (frequently called the Knudsen layer) with a thickness on the order of an average mean free path l. Outside the Knudsen layer, the gas flow is described by the Navier–Stokes equations that must be supplemented with the boundary conditions on the wall surface. These conditions are usually taken in the form of an extrapolated hydrodynamic sliding velocity at the wall (U_{sl}). For a small velocity gradient, we may write $U_{sl} = K_{sl} l g_v$. The task of finding the isothermal sliding velocity proceeding from the Boltzmann equation for the Knudsen layer is called the Kramers problem.

By thermal sliding we imply the gas motion in the vicinity of a nonuniformly heated wall surface. Here, the gas flow appears as a result of collisions between gas molecules from the near-wall (Knudsen) layer and the nonuniformly heated wall. At a large distance from the wall, the system is characterized by a preset temperature gradient. Here, the sliding velocity is determined as the limit

$$U_{sl} = \lim_{x \to \infty} U_y(x).$$

For the first time, the Kramers problem was analytically solved by Cercignani within the framework of the Bhatnagar–Gross–Kruck (BGK) model with constant collisional frequency [1]. This was followed by a solution for the same model with a variable frequency of collisions (including the case when this frequency is proportional to the velocity of molecules) [2]. The thermal sliding was originally considered by Loyalka and Cipolla [3]. Both sliding velocity problems for some model kinetic equations with the collisional frequency proportional to the velocity of molecules were also considered in our previous papers [4, 5]. Numerical results for the sliding problems obtained using a nonlinear Boltzmann equation were originally reported in [6, 7].

In a linearized stationary approximation, the distribution function can be presented in the form of $f(\mathbf{r}, \mathbf{v}) = f_0(y)(1 + \varphi(\mathbf{r}, \mathbf{v}))$, where $f_0(y)$ is the local Maxwell distribution function:

$$f_0(y) = n(y)\left(\frac{m}{2\pi k T(y)}\right)^{3/2} \exp\left(-\frac{m v^2}{2kT(y)}\right).$$

For the sliding problems under consideration, the linearized stationary kinetic equation can be written in the

following form:

$$\mathbf{C}\nabla\varphi + C_y(C^2 - 5/2)g_t = J[\varphi],$$

where $\mathbf{C} = \sqrt{\beta}\,\mathbf{v}$ is the dimensionless velocity f molecules, $\beta = m/2kT$, and g_t is the logarithmic temperature gradient. For the BGK model with constant collisional frequency, the collision integral is as follows:

$$J[\varphi] = \sqrt{\beta}\nu\left[2\mathbf{CU} + \frac{\delta n}{n_0} + \left(C^2 - \frac{3}{2}\right)\frac{\delta T}{T_0} - \varphi\right].$$

Here,

$$\mathbf{U} = \pi^{-3/2}\int \exp(-C^2)\mathbf{C}\varphi d^3C,$$

$$\frac{\delta n}{n_0} = \pi^{-3/2}\int \exp(-C^2)\varphi d^3C,$$

$$\frac{\delta T}{T_0} = \frac{2}{3}\pi^{-3/2}\int \exp(-C^2)\left(C^2 - \frac{3}{2}\right)\varphi d^3C.$$

For the BGK model with collisional frequency proportional to the velocity of molecules (here, the mean free path is constant), the collision integral can be written as [9]

$$J[\varphi] = \sqrt{\beta}\nu\left[\frac{3}{4}\sqrt{\pi}\mathbf{CU}_* + \frac{\sqrt{\pi}}{2}\frac{\delta n_*}{n_0} + \frac{\sqrt{\pi}}{4}(C^2 - 2)\frac{\delta T_*}{T_0} - \varphi\right],$$

where

$$\mathbf{U}_* = \pi^{-3/2}\int C'\exp(-C'^2)\mathbf{C}'\varphi d^3C',$$

$$\frac{\delta n_*}{n_0} = \pi^{-3/2}\int C'\exp(-C'^2)\varphi d^3C',$$

$$\frac{\delta T_*}{T_0} = \pi^{-3/2}\int C'\exp(-C'^2)(C'^2 - 2)\varphi d^3C'.$$

In this paper, we will consider a simplest nontrivial generalization of the above collision integrals taking into account the possibility of a more complicated relationship between the collisional frequency and the velocity of molecules.

Consider the following linearized collision integral:

$$J[\varphi] = \sqrt{\beta}\nu\left[2\alpha_{11}C\mathbf{CU}_* + 2\alpha_{12}\mathbf{CU}_* + 2\alpha_{21}C\mathbf{CU} + 2\alpha_{22}\mathbf{CU} + \frac{\sqrt{\pi}}{2}C\frac{\delta n_*}{n_0} + \frac{\sqrt{\pi}}{4}C(C^2 - 2)\frac{\delta T_*}{T_0} - C\varphi\right].$$

Containing the above models as particular cases, this integral corresponds to an intermediate character of the collisional frequency dependence on the velocity of molecules.

The collision integral must obey the following condition [8]:

$$\int \exp(-C^2)\varphi J[\psi]d^3C = \int \exp(-C^2)\psi J[\varphi]d^3C. \quad (1)$$

Equation (1) implies the symmetry of coefficients entering into the collision integral: $\alpha_{12} = \alpha_{21}$. In addition, this integral must satisfy the laws of conservation of the number of molecules and the system momentum and energy [8]. Talking these conditions into account, we arrive at the following expression for the collision integral:

$$J[\varphi] = \sqrt{\beta}\nu C\left[\frac{\sqrt{\pi}}{2}\frac{\delta n_*}{n_0} + \frac{\sqrt{\pi}}{2}(C^2 - 2)\frac{\delta T_*}{T_0} + 2a_2\mathbf{CU}_* + 2a\frac{\mathbf{CU}}{C} + 2a_1\frac{\mathbf{CU}_*}{C} + 2a_1\mathbf{CU}\right], \quad (2)$$

where $a_1 = -2\alpha a$, $a_2 = 2\alpha(1 + 2\alpha a)$, and $\alpha = 3\sqrt{\pi}/16$. The parameter a is related to the Prandtl number by a relationship

$$\mathrm{Pr} = \frac{8\alpha(1 + 2a) - 2a}{9\alpha - 2a(1 - 9\alpha^2)}.$$

In the sliding problems, the distribution function can be presented as $\varphi = C_y h$ [8]. In view of the symmetry of the problem, the function h depends only on the absolute velocity value, the cosine of the angle between the velocity vector (i.e., the direction of molecular motion) and the surface normal $\mathbf{n}$ ($\mu = (\mathbf{Cn})/C$), and a single spatial coordinate x: $h = h(x, C, \mu)$. Then the stationary kinetic equation with the collision integral (2) acquires the following form:

$$\mu\frac{\partial h}{\partial x} + h(x, \mu, C) + g_t\left(C - \frac{5}{2C}\right) = \int k(C, C')h(x, \mu')dm, \quad (3)$$

$$k(C, C') = \frac{a}{C} + a_1 + a_1\frac{C'}{C} + a_2C',$$

$$dm = 2\pi^{-1/2}\exp(-C'^2)C'^4(1 - \mu'^2)dC'd\mu'.$$

For $a = 0$, Eq. (3) converts into a well-known equation [9], Eq. (1.2) representing a BGK model with the collisional frequency proportional to the velocity of molecules. In deriving Eq. (3), we have performed integration with respect to the azimuth angle (in the (C_y, C_z) plane). It should be noted that the true Prandtl number corresponds to $a = 3\alpha/(1 - 6\alpha^2)$.

The boundary conditions are formulated so as to express a diffuse reflection of molecules from the wall surface:

$$h(0, \mu, C) = 0, \quad 0 < \mu < 1,$$
$$h(x, \mu, C) = h_{as}(x, \mu, C) + o(1),$$
$$x \longrightarrow \infty, \quad -1 < \mu < 0,$$

where

$$h_{as}(x, \mu, C) = 2U_{sl} + 2g_v(x - \mu)g_t(b_0/C + b_1 - C + 5/(2C)),$$

$$b_1 = -\frac{1 + 2\alpha a}{8\alpha - 2a(1 - 9\alpha^2)}, \quad b_0 = \frac{a}{8\alpha - 2a(1 - 9\alpha^2)}.$$

For the true Prandtl number (Pr ≈ 2/3), we have $b_1 = -1/2\alpha$, $b_0 = 3/2$.

Let us consider projections of the sliding problem onto three orthogonal directions:

$$e_1(C) = 1, \quad e_2(C) = 1/C, \quad e_3(C) = C - x_1 - x_2/C.$$

The quantities $x_1 = \alpha/(1 - 8\alpha^2)$ and $x_2 = 2(1 - 10\alpha^2)/(1 - 8\alpha^2)$ were obtained using the orthogonality conditions:

$$\int_0^\infty \exp(-C^2)e_j(C)e_3(C)dC = 0, \quad j = 1, 2.$$

We will find the function h in the following form:

$$h(x, \mu, C) = \sum_{j=1}^{3} \psi_j(x, \mu)e_j(C).$$

Now the sliding problem is equivalent to two problems, one of these representing a vector problem with respect to the vector-column $\psi = [\psi_1\psi_2]^t$ (t denotes the transposition), and the other, a scalar problem with respect to ψ_3. The vector problem consists of the equation

$$\mu\frac{\partial\psi}{\partial x} + \psi(x, \mu) = \frac{3}{4}K\int_{-1}^{1}(1 - \mu'^2)\psi(x, \mu')d\mu', \quad (4)$$

where

$$K = \begin{bmatrix} 1 & \gamma_1 \\ 0 & \gamma_2 \end{bmatrix}, \quad \gamma_1 = 2\alpha - \frac{1}{2}a\beta, \quad \gamma_2 = \frac{4a\beta}{3\sqrt{\pi}},$$
$$\beta = 1 - \alpha^2$$

and the boundary conditions

$$\psi(0, \mu) = \mathbf{0}, \quad 0 < \mu < 1, \quad \mathbf{0} = \begin{bmatrix} 0 \\ 0 \end{bmatrix}, \quad (5)$$

$$\psi(x, \mu) = \psi_{as}(x, \mu) + o(1), \quad x \longrightarrow \infty,$$
$$-1 < \mu < 0, \quad (6)$$

where

$$\psi_{as}(x, \mu) = \begin{bmatrix} 2U_{sl} + 2g_v(x - \mu) + g_t(b_1 - x_1) \\ g_t(5/2 + b_2 - x_2) \end{bmatrix}.$$

Omitting the procedure of solving the boundary problem (4)–(6) as described in [4, 5], we only present the final formula for the sliding velocity:

$$U_{sl} = V_1 g_v + \frac{1}{4(4\alpha - a\beta)}g_t. \quad (7)$$

For $g_t = 0$, formula (7) gives a solution to the Kramers problem:

$$U_{sl} = 0.58195 g_v. \quad (8)$$

Formula (8) coincides with an expression for the isothermal sliding velocity in a gas with the collisional frequency proportional to the velocity of molecules [4].

For $g_v = 0$, formula (7) gives a solution to the problem of thermal sliding:

$$U_{sl} = \frac{1}{16\alpha - 4a\beta}g_t. \quad (9)$$

Taking $a = 0$ in formula (9), we obtain $U_{sl} = (1/3\sqrt{\pi})g_t = 0.18806 g_t$, which coincides with the thermal sliding velocity in a gas with the collisional frequency proportional to the velocity of molecules [4].

For the true Prandtl number, formula (9) yields

$$U_{sl} = \frac{1 - 6\alpha^2}{4\alpha}g_t = 0.25375 g_t.$$

Finally, for a gas with a constant collisional frequency we obtain $U_{sl} = 1.0161 g_v$ and $U_{sl} = 0.3881 g_t$.

Upon going to the dimensional variables and determining the mean free path (according to Cercignani [8]) as $l = (\eta/\rho)\sqrt{\pi m/2kT}$, we obtain the coefficients of isothermal and thermal sliding:

$$K_{sl} = \frac{15}{8}V_1 = 1.09115,$$

$$K_{T\,sl} = \frac{15}{8}\sqrt{\pi}(0.25375) = 0.84330,$$

where

$$V_1 = \frac{3}{4}\int_0^1 \frac{x(1-x^2)\left(1+\frac{7}{2}x^2+\frac{3}{2}x^3\ln\frac{1-x}{1+x}\right)}{\left[1-\frac{3}{2}x^2+\frac{3}{4}x(1-x^2)\ln\frac{1-x}{1+x}\right]^2+\left[\frac{3}{4}\pi x(1-x^2)\right]^2}dx.$$

According to the results of numerical calculations, $V_1 = 0.581946$. For a comparison, consider the numerical results obtained for the Boltzmann equation [6]: $K_{sl} = 1.11414$, $K_{Tsl} = 1.00866$.

A comparison with the results reported previously, shows that the values obtained as described above fall (for the thermal sliding) between data for the BGK models with constant collisional frequency and with constant mean free path. The new model can be referred to as the one with an intermediate character of the collisional frequency as function on the velocity of molecules. An important advantage of the proposed model is the presence of a parameter that may correspond to the true Prandtl number. The values of the sliding coefficients K_{sl} and K_{Tsl} in this kinetic model possess essentially a new qualitative status. Indeed, the "old" quantities were obtained using a model with incorrect Prandtl number and had to be recalculated for the correct Pr value, this procedure introducing an element of uncertainty. The results obtained using the proposed model, involving the correct Pr value, are free of this disadvantage.

Acknowledgments. The work was partly supported by the Russian Foundation for Basic Research, project no. 99-01-00336.

REFERENCES

1. C. Cercignani, Ann. Phys. **20** (3), 219 (1962).
2. C. Cercignani, Ann. Phys. **40** (3), 469 (1966).
3. S. K. Loyalka and J. W. Cipolla, Phys. Fluids **14** (8), 1656 (1971).
4. A. V. Latyshev and A. A. Yushkanov, *Rigorous Solutions of the Boundary Problems for the Model Boltzmann Equations with Variable Collisional Frequency (A Monograph)*, Available from VINITI No. 1360–V96 (1996).
5. A. V. Latyshev and A. A. Yushkanov, Zh. Vychisl. Mat. Mat. Fiz. **37** (4), 483 (1997).
6. T. Ohwada, Y. Sone, and K. Aoki, Phys. Fluids A **1** (9), 1588 (1989).
7. S. K. Loyalka, Physica A (Amsterdam) **163**, 813 (1990).
8. C. Cercignani, *Theory and Application of the Boltzmann Equation* (Elsevier, New York, 1975; Mir, Moscow, 1978).
9. A. V. Latyshev and A. A. Yushkanov, Izv. Akad. Nauk, Ser. Mekh. Zhidk. Gaza, No. 3, 140 (1996).

Translated by P. Pozdeev

Technical Physics Letters, Vol. 26, No. 12, 2000, pp. 1038–1040. Translated from Pis'ma v Zhurnal Tekhnicheskoĭ Fiziki, Vol. 26, No. 23, 2000, pp. 24–29.

Ultradisperse Powders Obtained by Sputtering a Target with High-Power Nanosecond Pulsed Ion Beam

G. E. Remnev, A. N. Zakutaev, Yu. F. Ivanov, V. A. Makeyev, A. V. Potemkin, and V. M. Matvienko

Research Institute of Nuclear Physics, Tomsk Polytechnic University, Tomsk, Russia;
e-mail: remnev@ephc.npi.tpu.ru

Received April 13, 2000

Abstract—We present the results of experiments on the obtaining of ultradisperse powders by sputter ablation of aluminum and stainless steel targets bombarded with high-power pulsed ion beams of nanosecond pulse duration. For an ion beam with an energy of 300 keV, a current density of 250–300 A/cm^2, and a pulse width of 60 ns, the sputtered particles range in size from 2.5 to 700 nm and are emitted within an angle of 30°–40°. A specific beam energy consumption for the powder production by sputtering an aluminum target amounts to 6 (kW h)/kg. © *2000 MAIK "Nauka/Interperiodica".*

The production, characterization, and application of ultradisperse powders (UDPs) are still among currently important problems. Among numerous technologies used for obtaining these materials [1, 2], the one closest to the method considered below is the electric explosion in semiconductors characterized by a specific power consumption for the UDP production on the order of 10 (kW h)/kg [3]. Pulsed nanosecond beams of high-energy charged particles acting upon metal and dielectric materials can also provide for the energy concentration sufficient to produce explosion-like fracture of the near-surface target layer.

In some experiments (see, e.g., [4] and references therein), high-power pulsed ion beams were used for the ultrafast deposition of thin films from an ablation plasma generated by the beam–target interaction. Plasma generated by an ion beam at the target surface can be used to obtain microscopic oxide particles upon interaction of the plasma species with oxygen [5]. It should be noted that the use of high-power ion beams for explosive erosion of the target surface has two significant advantages: (i) there are no special requirements on the shape and size of targets and (ii) this method is applicable to the sputtering of any solids, including composite and dielectric compounds.

Below we present the results of our experiments on using high-power pulsed ion beams (ion energy, ~300 keV; beam current density on the target, 250–300 A/cm^2; pulse duration, ~50 ns) for the production of UDPs. The experiments were conducted using a scheme outlined previously [4]. The setup was based on a Temp-2 particle accelerator with the following ion beam parameters: ion energy, ~350 keV; beam current density, ~250 A/cm^2; pulse duration, ~60 ns. The sample targets were made of a commercial-purity aluminum and the Hadfield steel (Fe–1.2C–12.6Mn–0.97Ni–0.32Si–0.29Cr–0.005S, wt %). The samples of sputtered materials were prepared by collecting these species on standard carbon films deposited by a conventional method in a VUP-2k vacuum system, followed by their mounting on special copper grids for the electron-microscopic examination. The morphological, granulometric, and phase analyses were carried out by methods of transmission electron diffraction microscopy using an EM-125 electron microscope (Russia).

The material sputtered from an ablated target includes two components: vapor–plasma species and microscopic particles. According to experimental data, the weight ratio of these components is determined by the pulsed beam power density and the degree of defectness in the surface layer of the target. Note that characteristics of the surface layer may depend to a considerable extent on the number of preceding pulses of current to the target. Note also a different character of the angular distribution of microparticles (Fig. 1, curve *1*) and the total sputtered material (Fig. 1, curve *2*). An analysis of the experimental data for an aluminum target presented in Fig. 1 indicated that half-angle of the particle emission is $\theta_{1/2} \approx 15°–20°$, whereas the total sputtered material distribution is characterized by $\theta_{1/2} \approx 25°–30°$.

By their morphological characteristics, all the microparticles sputtered from a target can be conventionally divided into three groups. The first group includes single-crystal particles having the shape of flattened spheroids (Fig. 2a). These particles, with the size (diameter) varying typically within 300–700 nm, occur for the most part in the central region of the sputtered material. Particles of smaller size are randomly distributed over the entire ablation torch volume. The results of the electron-microscopic microdiffraction

1063-7850/00/2612-1038$20.00

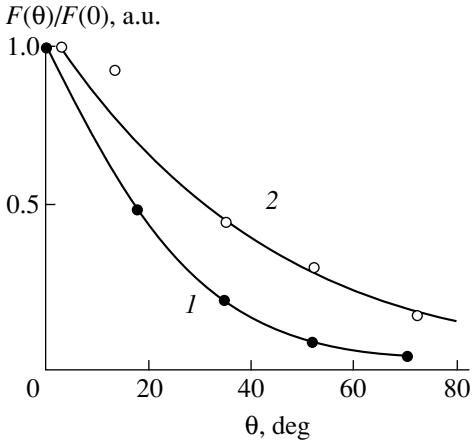

Fig. 1. Angular distribution of (*1*) a spheroidal (droplike) fraction and (*2*) the total material sputtered from a copper target by a high-power ion beam. Points represent the experimental data and solid curves, the approximation functions: (*1*) exp(–2.5|θ|); (*2*) exp(–1.4|θ|).

measurements showed that particles of the first group are made of aluminum.

The second group represents particles with an irregular shape—fragments possessing a polycrystalline structure (Fig. 2b) with dimensions within the same range as above (300–700 nm). The size of crystalline grains constituting the particles is 40–50 nm. The microdiffraction data indicate that these particles are composed of aluminum oxides and carbide, the former having a coarser polycrystalline structure than the latter.

The third group includes particles of a spheroidal shape with dimensions predominantly within the 20- to 60-nm range (Fig. 2c) According to the microdiffraction data, these particles are made of aluminum. Analysis of the particle mass distribution in the peripheral region of the ablation torch (Fig. 3) indicated that the third group accounts for ~30% of the total number of particles in this zone.

The films obtained upon deposition of the material sputtered from a target made of the Hadfield steel exhibited an amorphous structure (Fig. 2d). The microdiffraction patterns from these films clearly revealed particles with dimensions in the nanometer range on the amorphous background, with a minimum detectable crystal size of 2.5 nm. As demonstrated previously [6], the stoichiometric composition of the sputtered material corresponds to the target stoichiometry.

Thus, the above data show that material sputtered from a solid material with a high-energy ion beam contains, among all others, an ultradisperse powder fraction. The microparticles exhibit different surface morphologies (fragments, spheroids), internal structures (single and polycrystals), dimensions (ranging from 2.5 to 700 nm, Fig. 3), and phase compositions (pure metals, oxides, carbides). We may suggest that microparticles with the fragment morphology appear as a result of explosive fracture of the surface layer of the target. The carbide and oxide phases are formed by interaction of the target material with carbon and oxygen atoms adsorbed on the target surface. Microparticles possessing a spheroidal (droplike) shape appear as a result of fusion of the above fragments under the beam action upon their detachment from the target surface. Finally, spheroidal nanoparticles are probably formed upon spraying of the melted target material and disintegration of the large particles.

In view of the possible application of this ion sputter method to the UDP production, it was of interest to estimate the specific energy consumption of the process.

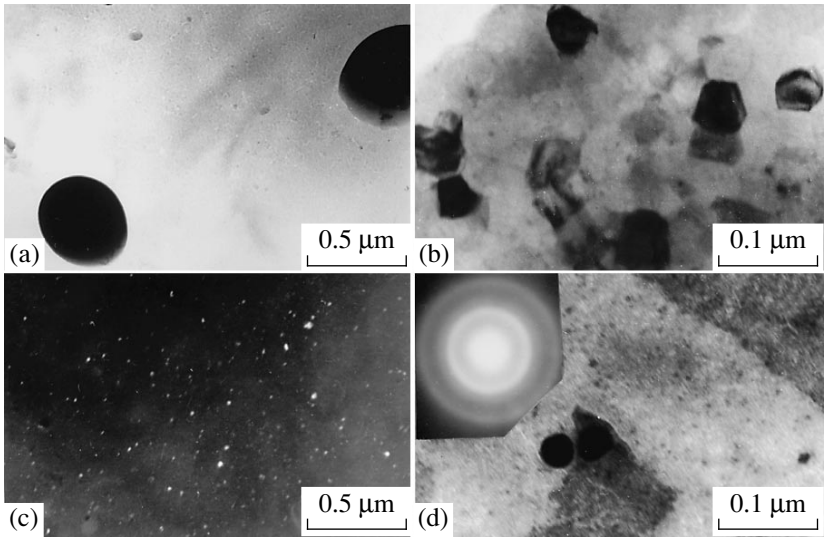

Fig. 2. Electron-microscopic images of UDPs formed upon sputtering metal targets with high-power pulsed ion beams: (a, b, d) bright-field images; (c) dark-field image in the [111] Al reflection (see the text for explanations).

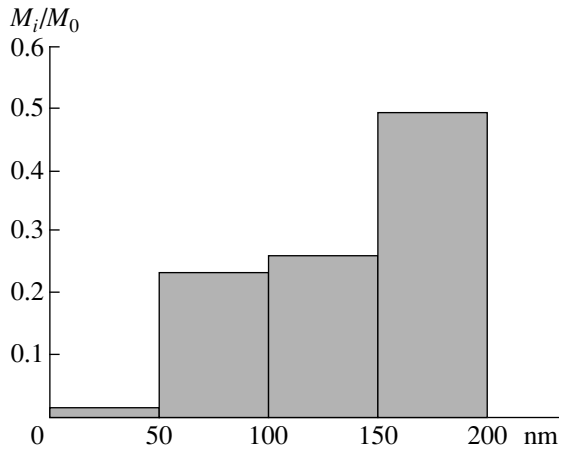

Fig. 3. Relative particle weight distribution in the peripheral region of an ablation torch of the sputtered material.

These estimates were obtained by weighing the target before and after sputtering. For an aluminum target, the specific beam energy consumption was ~6 kW h per kg of sputtered material. Note that this is an integrated characteristic not optimized with respect to the beam parameters. Thus, we have demonstrated the possibility of UDP production by sputtering metallic materials with high-power pulsed ion beams. The resulting particle dimensions range from 2.5 to 700 nm. The particle yield is characterized by a narrow angular distribution ($\theta_{1/2} \approx 15°$–$20°$), which facilitates the task of collecting the sputtered material.

REFERENCES

1. I. D. Morokhov, L. I. Trusov, and V. N. Lapovok, *Physical Phenomena in Superdispersed Media* (Énergoizdat, Moscow, 1984).
2. A. I. Gusev, *Nanocrystalline Materials: Production Methods and Properties* (Ural. Otd. Ross. Akad. Nauk, Yekaterinburg, 1998).
3. Physics and Chemistry of Ultradispersed Powders, in *Interinstitution Collection of Scientific Works* (Nauchno-Issled. Inst. Vys. Napryazheniĭ, Tomsk. Politekh. Univ., Tomsk, 1990), Part 1.
4. G. E. Remnev, A. N. Zakutaev, Yu. F. Ivanov, *et al.*, Pis'ma Zh. Tekh. Fiz. **22** (8), 68 (1996) [Tech. Phys. Lett. **22**, 336 (1996)].
5. A. A. Bukaemskiĭ, in *Ultradispersed Materials. Production and Properties* (Krasnoyarsk, 1990), pp. 81–91.
6. I. F. Isakov, G. E. Remnev, and A. N. Zakoutaev, in *Proceedings of the 9th International Conference on High-Power Particle Beams "Beams-92"* (NTIS, Springfield, 1992), pp. 1966–1970.

Translated by P. Pozdeev

Technical Physics Letters, Vol. 26, No. 12, 2000, pp. 1041–1044. Translated from Pis'ma v Zhurnal Tekhnicheskoĭ Fiziki, Vol. 26, No. 23, 2000, pp. 30–37.

Mechanical and Electrical Properties of Fluorine-Containing Niobate Ferroelectric Ceramics

M. I. Kovalenko, L. A. Reznichenko, O. N. Razumovskaya, V. A. Aleshin, L. A. Shilkina, and S. O. Kramarov

Institute of Physics, Rostov State University, Rostov-on-Don, Russia

Rostov State Pedagogical University, Rostov-on-Don, Russia;

e-mail: mary@tdu.donpac.ru

Received April 11, 2000; in final form, July 5, 2000

Abstract—The presence of fluorine impurity in alkali metal niobate ceramics sharply deteriorates both mechanical and electrical properties of these ferroelectric materials. This effect is related to the separation of a glassy phase and the formation of an inhomogeneous microstructure, these factors giving rise to local stresses in the structural elements. It is concluded that intact niobate ferroelectric articles can be made of technical-grade Nb_2O_5 only provided that the initial material contains a minimum amount of fluorine impurity (below 0.2 wt %). © *2000 MAIK "Nauka/Interperiodica".*

The elemental base of modern piezoelectronics markedly increased upon the development of new ferroelectric ceramics based on alkali metal niobates (niobate ferroelectric ceramics, NFCs), which made it possible to create a number of ultrasonic transducers and related devices employing bulk and surface waves and capable of operating in the (previously hardly accessible) superhigh frequency range. This progress has become possible due to an advantageous combination of properties (not provided by the presently employed ZTS systems): a low dielectric permittivity ($\varepsilon_{33}^T/\varepsilon_0 \leq 100$) at a sufficiently high electromechanical coupling coefficient ($K_p \geq 0.35$), a high sound velocity ($V_R \sim 6$ km/s), and a broad spectrum of the mechanical Q factor ($Q_M = 50$–1500) [1].

Some features of the tasks encountered in the applications of ferroelectric ceramics require that the active elements be fabricated in the form of very thin plates, which implies very stringent requirements to the strength of these elements. In the case of NFCs, generally susceptible to self-fracturing [2], the mechanical properties become critical in determining the possible working conditions for both materials and devices. In this context, knowledge of the factors deteriorating the mechanical properties of NFCs and the conditions favoring their optimum characteristics are obviously of importance.

Previously [3], we have established that fluorine (a possible impurity in Nb_2O_5) may significantly affect the microstructure and hence the mechanical and electrical properties of NFCs. Since no quantitative data on the fluorine content were included at that time in the manufacturer's quality certificate on Nb_2O_5 of the NBO-PT grade, it was impossible to establish relationships between changes in the properties of commercial NFCs and variations in the fluorine impurity content. For this reason, we modeled the effects of this impurity by introducing specially synthesized Nb_3O_7F and KF compounds into fluorine-free Nb_2O_5 samples. In recent years, the fluorine content is indicated in the NFC quality certificates. This circumstance helped us follow variations in the NFC parameters in a more justified manner.

The experiments were performed with a PKR-35 material developed by us based on solid solutions of the (Na, Li)NbO_3 system. Using the standard techniques, we assessed the microstructural state and determined the lattice parameters, volumes (V') and deformations (δ) of the unit cells, as well as the phase ratio $\mu = Rh/R$ (i.e., the relative content of the rhombohedral and orthorhombic phases), the density (including the measured ρ_1, X-ray ρ_2, and relative ρ_3 values), and the electrical properties of the NFC samples studied. The sample strength was tested using a coaxial bending method, which provided evaluation of the ultimate tensile strength σ.

Figures 1–4 present data on the structural, electrical, and mechanical characteristics; densities; and strengths of NFCs based on Nb_2O_5 of the NBO-PT grade with various fluorine concentrations (by data of the manufacturer) and of the compositions based on Nb_2O_5 from various manufacturers (special purity grade) with fluorine additives (Nb_3O_7F or KF) introduced into the initial charge in the stage of component mixing. As seen

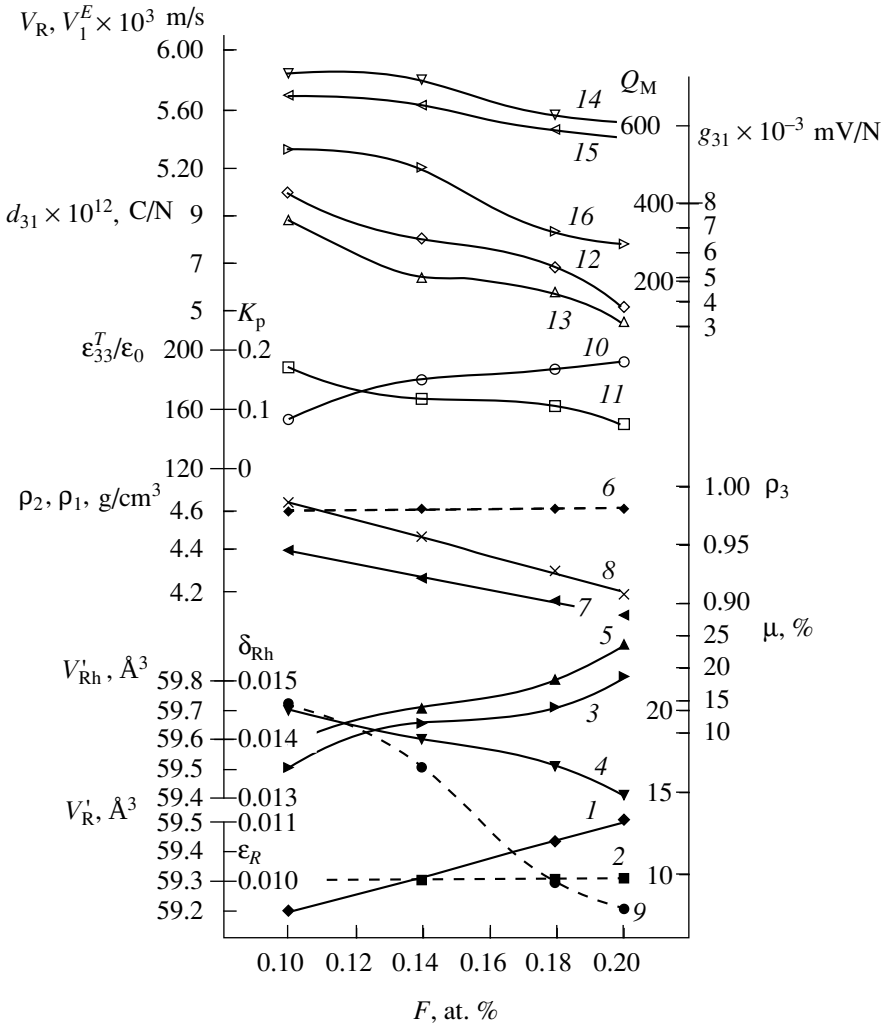

Fig. 1. Variation of the structural, electrical, and mechanical characteristics, densities, and strengths of solid solutions based on Nb_2O_5 of the NBO-PT grade depending on the fluorine impurity content (by data of the manufacturer): (*1*) V'_R; (*2*) δ_R; (*3*) V'_{Rh}; (*4*) δ_{Rh}; (*5*) μ; (*6*) ρ_2; (*7*) ρ_1; (*8*) ρ_3; (*9*) σ; (*10*) $\varepsilon_{33}^T/\varepsilon_0$; (*11*) K_p; (*12*) d_{31}; (*13*) g_{31}; (*14*) V_R; (*15*) V_1^E; (*16*) Q_M. Here d_{31} and g_{31} are the piezoelectric modulus and sensitivity, respectively; V_R and V_1^E are the sound (longitudinal oscillation mode) velocities measured of disks and plates (bars), respectively.

from these experimental data, an increase in the content of fluorine impurity in the solid solution sharply deteriorates ρ_1, ρ_3, and σ values of NFCs; the samples containing 0.2–0.4 wt % of fluorine were highly brittle. The same results were obtained for the solid solutions synthesized from both coarse and fine Nb_2O_5 fractions separated by washing the initial powder on an 0053 sieve. The coarse-grained samples exhibited lower strength than the fine-grained ones, which was related to a higher fluorine content in the former case (by thermogravimetric data).

The fluorine effect can be explained as follows. An analysis of the microstructure of tested samples showed that an increase in the fluorine impurity content in Nb_2O_5 leads to the formation of inhomogeneously distributed liquid phase [4]. This results in the appearance of a very inhomogeneous solid microstructure featuring new elements in the form of grain agglomerates and in the development of unusual intermittent secondary recrystallization process leading to the growth of separate grains with different composition [3] and abnormally large size [5]. These processes render the final solid solution sharply heterophase, featuring liquid phases of various types [4], crystalline phases with different compositions, and a gaseous phase filling the pores. As we have pointed out in [2], the natural difference in the thermal expansion coefficients of various phases and the anisotropic deformation of crystallites lead to the development of local stresses in the structural elements of samples on heating and cooling. The

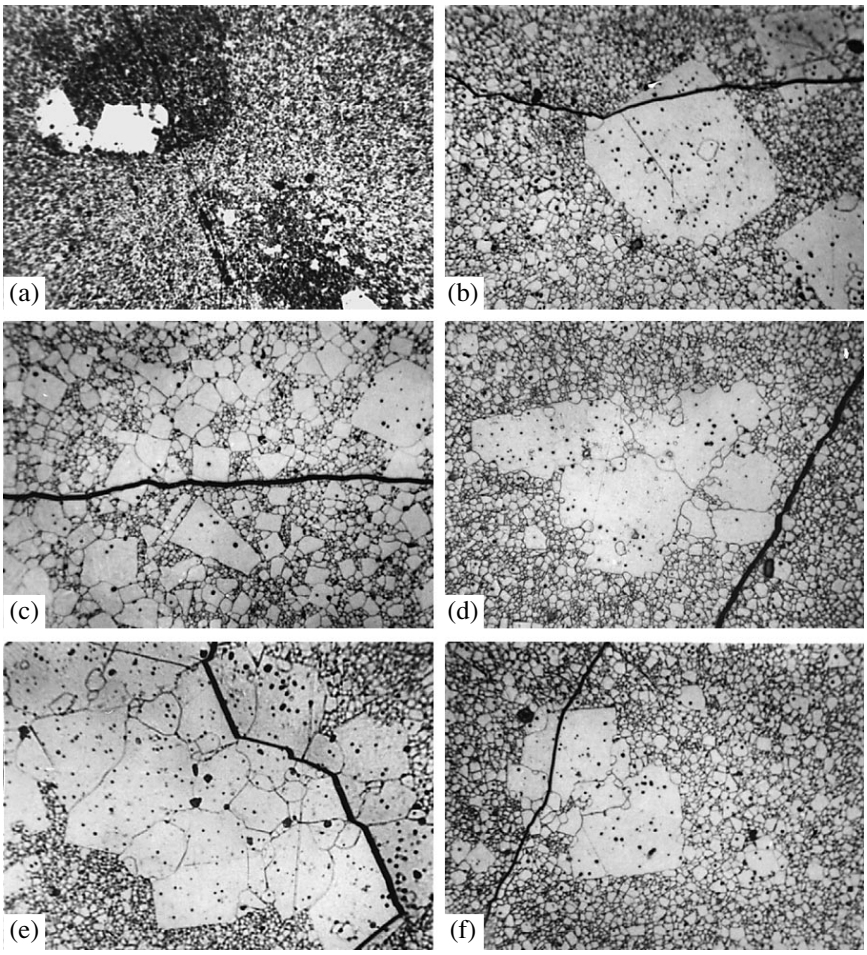

Fig. 2. Micrographs illustrating the crack formation in niobate ceramics (see the text for comments).

magnitude of these stresses depends both on the differential properties and the temperature variations. It is the development of these stresses that accounts for the formation of microcracks and the loss of strength.

The process of crack formation in NFCs is illustrated in Fig. 2. As seen from these micrographs, the cracks either appear in the vicinity of large individual grains (a), pass through such grains (b), or originate from the grain pileups and agglomerates (c). Although in some cases the cracks propagate via grain boundaries (d), they more frequently cleave the grain bodies (e). A large number of grains originate from grain boundaries of various types, including those in various stages of recrystallization (f). The phenomenon of desquamation (flake peeling) observed in the ceramic articles cooled upon sintering is also explained by crack development in the surface layers of samples, where the largest grains form and extensively grow during heat treatments.

Another remarkable fact is a change in the parameter μ representing the relative content of the rhombohedral (Rh) and orthorhombic (R) phases in the solid solution (Figs. 3 and 4). This is evidence that the phase diagram of the initial system is subject to changes when the solid solution is contaminated with fluorine. The μ value increases with the fluorine content in Nb_2O_5 of the NBO-PT grade and with the amount of fluorine introduced with Nb_3O_7F into Nb_2O_5 of the special purity grade. On the other hand, the μ value decreases upon introducing fluorine in the form of KF and upon separating Nb_2O_5 fractions. The latter observations probably reveal an additional influence of the additive composition and Nb_2O_5 dispersity upon the phase equilibrium in the solid solution studied. The loss of strength and a change in the pattern of phase equilibria in the initial solid solution are apparently related to deterioration of its electrical characteristics. The data in Fig. 1 show that an increase in the fluorine content in Nb_2O_5 is accompanied by a decrease in K_p, d_{31}, g_{31}, V_R, and Q_M values and by an increase in $\varepsilon_{33}^T/\varepsilon_0$, which markedly decreases the working performance of NFCs.

Thus, the results of our experiments showed that intact niobate ferroelectric articles can be made of technical-grade Nb_2O_5 only provided that the initial mate-

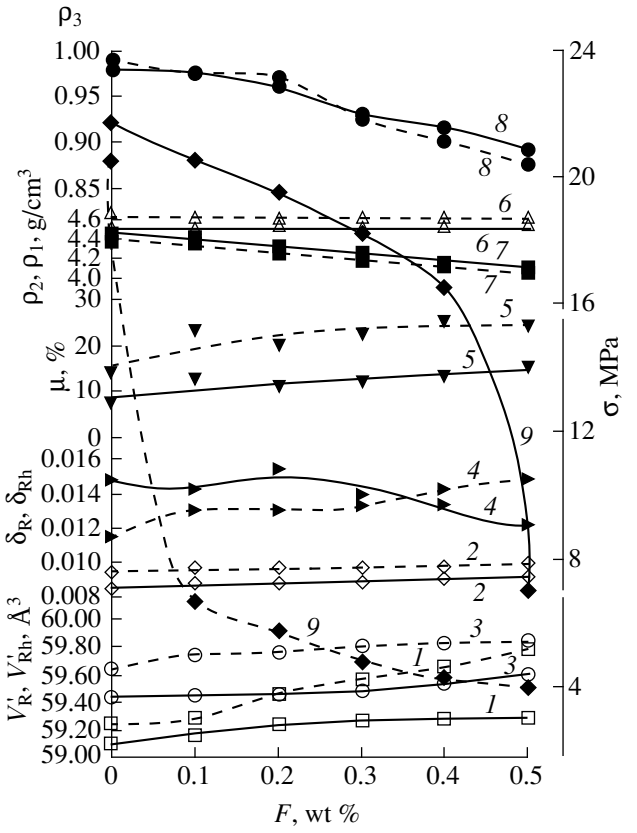

Fig. 3. Variation of the structural and mechanical characteristics, densities, and strengths of Nb_2O_5-based solid solutions depending on the fluorine content (introduced in the form of Nb_3O_7F additives): (*1*) V'_R; (*2*) δ_R; (*3*) V'_{Rh}; (*4*) δ_{Rh}; (*5*) μ; (*6*) ρ_2; (*7*) ρ_1; (*8*) ρ_3; (*9*) σ. Solid and dashed curves show data for Nb_2O_5 of the special purity grade obtained from the Apatity ceramics plant (Kola peninsula) and from the Institute of Steel and Alloys (Moscow), respectively.

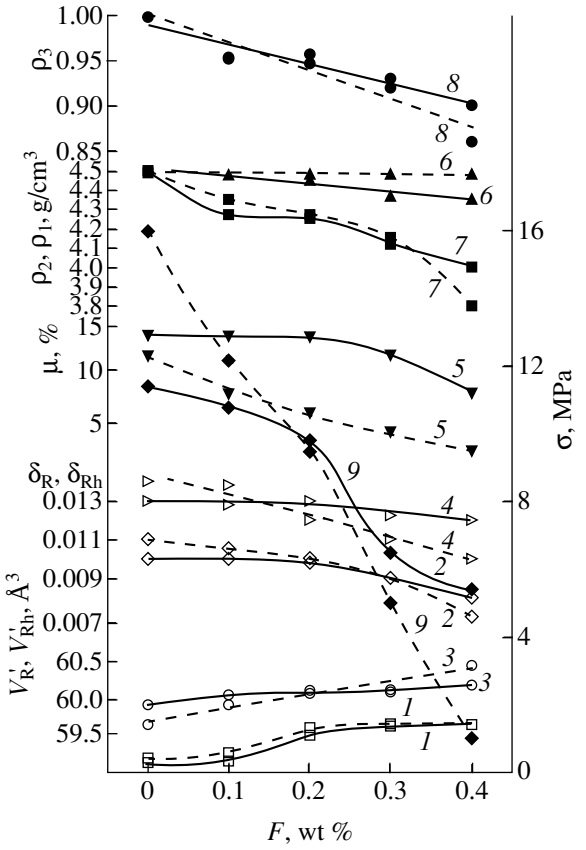

Fig. 4. Variation of the structural and mechanical characteristics, densities, and strengths of Nb_2O_5-based solid solutions depending on the fluorine content (introduced in the form of KF additives): (*1*) V'_R; (*2*) δ_R; (*3*) V'_{Rh}; (*4*) δ_{Rh}; (*5*) μ; (*6*) ρ_2; (*7*) ρ_1; (*8*) ρ_3; (*9*) σ. Solid and dashed curves show data for Nb_2O_5 of the special purity grade obtained from the Pyshma ceramics plant (Urals region) and from the Krasnyĭ Khimik plant (St. Petersburg), respectively.

rial contains a minimum amount of fluorine impurity (below 0.2 wt %).

Acknowledgments. The work was partly supported by the Russian Foundation for Basic Research, project no. 99-02-17575.

REFERENCES

1. E. G. Fesenko, A. Ya. Dantsiger, L. A. Reznichenko, *et al.*, Zh. Tekh. Fiz. **52** (11), 2262 (1982) [Sov. Phys. Tech. Phys. **27**, 1389 (1982)].
2. E. I. Bondarenko, V. D. Komarov, L. A. Reznichenko, and V. A. Chernyshkov, Zh. Tekh. Fiz. **58** (9), 1771 (1988) [Sov. Phys. Tech. Phys. **33**, 1071 (1988)].
3. L. A. Reznichenko, O. N. Razumovskaya, and L. A. Shilkina, Izv. Akad. Nauk SSSR, Neorg. Mater. **24** (10), 1708 (1988).
4. L. A. Reznichenko, O. N. Razumovskaya, *et al.*, in *Proceedings of the 7th International Workshop on the Physics of Ferroelectric Semiconductors, Rostov-on-Don, 1996*, Vol. 6, p. 149.
5. L. A. Reznichenko, V. A. Aleshin, *et al.*, in *Proceedings of the 7th International Workshop on the Physics of Ferroelectric Semiconductors, Rostov-on-Don, 1996*, Vol. 6, p. 170.

Translated by P. Pozdeev

Technical Physics Letters, Vol. 26, No. 12, 2000, pp. 1045–1048. Translated from Pis'ma v Zhurnal Tekhnicheskoĭ Fiziki, Vol. 26, No. 23, 2000, pp. 38–46.

Ion Recombination on Dust Particles in a Dense Gas Plasma Excited by a Hard Ionizing Factor

S. I. Yakovlenko

Institute of General Physics, Russian Academy of Sciences, Moscow, Russia

Received June 27, 2000

Abstract—A theoretical model is proposed that describes the main kinetic mechanisms operating in a dust plasma formed upon the bulk ionization of a dense gas by a hard factor. An expression is derived for the ion density distribution around a charged dust particle. It is shown that ions in the plasma recombine with charged dust particles according to the Langevin mechanism. A condition is established under which the dust particles are bearing all the negative charge in the plasma, compensated by the positive charge of ion clouds. A new criterion for manifestation of the collective properties in the dust plasma is formulated. © *2000 MAIK "Nauka/Interperiodica".*

Introduction

Recently, Fortov *et al.* [1] reported on the collective phenomena observed in a dust plasma formed as a result of the dense gas ionization by nuclear fission fragments. The present study is devoted to analysis of the process of ion recombination on the surface of dust plasma particles and is aimed at establishing a criterion for manifestation of the collective properties in this plasma. The analysis is based on the theory of a thermoemissive plasma described in [2–5].

We will consider the following pattern of phenomena. A hard ionizing factor (e.g., an electron or ion beam, fission fragments from nuclear reactions) [6] produces ionization of dense gas containing suspended dust particles. The dust particles are negatively charged in the ionized gas as a result of different average velocities of ions and electrons. If the density of powder particles is sufficiently high, electrons and ions would mostly recombine on the dust particles at a certain special value of the gas ionization rate. The mechanism of recombination is determined by the diffusion and drift of ions in the field of a charged dust particle.

As was demonstrated previously [4], interaction of the charged centers surrounded by clouds of oppositely charged particles results in the mutual attraction of these centers, which is caused by the polarization forces. This factor accounts for the collective phenomena in the system under consideration.

Ion Recombination and Charge Distribution Around Dust Particles

Basic equations. Let us first consider the process of ion charge neutralization on a dust particle bearing a given charge eZ_p, where e is the electron charge. We assume that ions produced by ionization in the volume diffuse as a result of collisions with neutrals and drift toward the dust particle, being attracted by the electric field of the negatively charged particle. The latter field may be partly shielded by the charge of ions drifting toward the dust particle. These processes are described by a set of equations including the equation of ion momentum transfer, the continuity equation, and the Poisson equation. Accordingly, the initial set of equation is as follows [6, 7]:

$$\begin{gathered}\mathbf{u}_i = eb_i\mathbf{E} - (D/N_i)\operatorname{grad}(N_i); \quad \operatorname{div}(N_i\mathbf{u}_i) = G; \\ \operatorname{div}(\mathbf{E}) = 4\pi eN_i,\end{gathered} \tag{1}$$

where $\mathbf{u}_i$ is the average ion velocity vector, b_i is the ion mobility, D is the diffusion coefficient ($D = b_iT$, T being the gas temperature), N_i is the number density of ions, $\mathbf{E}$ is the electric field vector, and G is the rate of gas ionization by the external hard factor.

We assume the gas particle to possess a spherical shape with the radius r_0. Selecting r_0 as the unit length, introducing the spherical coordinate system centered at the particle, and considering a total electric charge $E(r)r^2$ inside a sphere with the radius r instead of the radial electric field strength $E(r)$, we obtain the following set of dimensionless equations for the number density of electrons and the total charge inside the sphere:

$$\begin{gathered}\frac{dn_i(x)}{dx} = -\frac{n_i(x)z(x)}{x^2} + g\frac{1-n_px^3}{x^2}; \\ \frac{dz(x)}{dx} = -dn_i(x)x^2.\end{gathered} \tag{2}$$

Here, $n_i(x) = N_i(r)r_0^3$ is the dimensionless number density of ions; $x = r/r_0$ is the radial coordinate measured in r_0 units; $z(x) = (er_0/T)E(r)r^2$ is the dimensionless charge inside the sphere with the radius r; $g = (Gr_0^2/4\pi b_iT)$ is the dimensionless average ionization density; n_p =

$(4\pi/3)N_p r_0^3$ is the dimensionless average density of dust particles, N_p is the number density of dust particles; and $d = (4\pi e^2/Tr_0)$ is the ratio of the Coulomb target parameter to the dust particle radius.

A boundary condition for the number density of ions is determined assuming that an ion striking the dust particle is lost. By equating the ion flux to the total surface of particles $4\pi r_0^2 N_i(r_0)u_i$ to the ionization rate per unit volume G, we obtain a condition for the number density of ions on a spherical wall surface:

$$n_i(x = 1) \equiv n_{i0} = Gr_0(4\pi u_i), \quad (3)$$

where m_i is the ion mass and $u_i = (T/4\pi m_i)^{1/2}$ is the average projection of the ion velocities onto the axis perpendicular to the wall surface for the Maxwell ion velocity distribution.

A boundary condition for the dimensionless charge is as follows:

$$z(x = 1) \equiv z_0 = Z_p(e^2/r_0T). \quad (4)$$

Approximate solution. Assuming that the radius of dust particles is much smaller than the distance between them ($n_p \ll 1$) and that the particle charge eZ_p is sufficiently large to ignore the charge shielding at a distance on the order of r_0 and take $z(x) \approx z_0$ (a condition sufficient for this are formulated below), we may obtain a solution to the diffusion equation in an analytical form:

$$n_i(x) = \frac{g}{z_0}\left\{1 - \left(1 - \frac{n_{i0}z_0}{g}\right)\exp\left[-z_0\left(1 - \frac{1}{x}\right)\right]\right\}. \quad (5)$$

This solution corresponds to the rate of ion recombination obeying to the Langevin law [8, 9]. Indeed, for $x \longrightarrow \infty$ and sufficiently large z_0, that is, when

$$(1 - n_{i0}z_0/g)\exp(-z_0) \ll 1, \quad (6)$$

we obtain $n_i(\infty) = g/z_0$ or

$$G = (4\pi Z_p e^2 b_i)N_i(\infty). \quad (7)$$

In other words, the number of ions per unit volume produced by ionization is equal to the number of ions lost as a result of recombination on the surface of dust particles; the quantity $\alpha_L \equiv 4\pi Z_p e^2 b_i$ is the well-known Langevin recombination coefficient [8, 9].

Note that the quantity $n_{i0}z_0/g = 4\pi Z_p e^2 b_i/(4\pi r_0^2 u_i)$ entering into the equation for $n_i(x)$ is essentially the ratio of the Langevin recombination coefficient to the coefficient of recombination that would be determined by the flux of ions onto the dust particle surface, provided that the number density of ions is independent of the distance to the particle. Here, both in the case of dominating Langevin's recombination coefficient ($n_{i0}z_0/g \gg 1$) and in the opposite case ($n_{i0}z_0/g \ll 1$), the resultant recombination flux $G = \alpha_L N_i(\infty)$ is determined by the Langevin mechanism. The two limiting cases differ only by the ratio of the ion number densities on the sphere and on the periphery: $n_{i0}/n_i(\infty) = n_{i0}z_0/g$.

Note that condition (6) is valid for sufficiently large $z_0 = Z_p(e^2/r_0T)$, which is provided either by small r_0 (as in the case of the usual ion–ion recombination by the Langevin mechanism) or by large z_p (as in the case of recombination on dust particles considered in this work).

Ionization–Recombination Balance

Dust particle charging. Let us consider characteristics of the dust plasma. A negative charge on the dust particle surface may arise due to a difference between average velocities of electrons and ions. This phenomenon is well known in physical electronics (see, e.g., [10, p. 43]). Assuming the Maxwell velocity distribution and equating the flux of ions to the particle surface $N_i u_i$ to that of electrons $N_e u_e \exp(-e\varphi/T_e)$, we obtain

$$\varphi_0 = (T_e/2e)\ln(N_i m_i T/N_e m_e T_e) \approx \ln(m_i/m_e).$$

Here, φ_0 is the dust particle potential; $u_i = (T/4\pi m_i)^{1/2}$ and $u_e = (T_e/4\pi m_e)^{1/2}$ are the average projections of the velocities of ions and electrons onto the axis perpendicular to wall surface; T_e and T are the electron and gas temperatures. Using this potential value, we may formally determine the charge of the particle:

$$Z_p = r_0\varphi_0/e = (r_0T_e/2e^2)\ln(N_i m_i T/N_e m_e T_e). \quad (8)$$

This estimate applies well to a gas-discharge plasma, but may lead to considerable errors in the case of a plasma produced by a hard ionizing factor (see below).

Charge kinetics. The number densities of ions $N_i = N(\infty)$ and electrons N_e in the dust plasma are described by the charge balance equation and the quasilinearity condition. In the case under consideration, these relationships can be written as follows:

$$dN_i/dt = G - \alpha_d N_i N_e - \alpha_L N_i N_p,$$
$$N_e = N_i - Z_p N_p,$$

where α_d is the dissociative recombination coefficient and α_L is the Langevin recombination coefficient mentioned above. This simple model is usually applied to describing a dense ideal gas.

Under quasistationary conditions ($dN_i/dt = 0$), we may solve the above quadratic equation and present the

ratio of the ion number density N_i to the charge density on a dust particle Z_pN_p in the following form:

$$\beta \equiv \frac{N_i}{Z_pN_p} = \sqrt{\left(\frac{a-1}{2}\right)^2 + a\tilde{g}} - \frac{a-1}{2} = \begin{cases} a\tilde{g}/(a-1), & 4a\tilde{g}/(a-1) \ll 1, \\ \sqrt{a\tilde{g}}, & 4a\tilde{g}/(a-1) \gg 1. \end{cases} \quad (9)$$

Here, $a = \alpha_L/(Z_p\alpha_d)$ is a parameter characterizing the ratio of the rates of the Langevin and dissociative recombinations (for $a \gg 1$, recombination on the dust particles dominates) and $\tilde{g} = G/(\alpha_L Z_p N_p)$ is the reduced rate of ionization produced by the external factor.

Note an important circumstance: for an ionization rate satisfying the condition $\tilde{g} = 1$, or

$$G = \alpha_L Z_p N_p, \quad (10)$$

all the negative charge in the system is concentrated on the dust particles ($N_e = 0$, $N_i = Z_pN_p$), while the gas contains only positive ions.

Experiments with Dust Plasma Excited by Nuclear Fission Fragments

Experimental results. Now we will apply the above theory to description of the characteristics of a dust plasma in experiments using nuclear fission fragments as a hard ionization source [1]. In one of these experiments, the plasma was excited by Cf^{252} fission fragments and in the other, by products of the Ce^{141} β-decay. We will concentrate on the latter data. The dust was composed of CeO_2 particles with an average radius of $r_0 = 0.5$ μm. The gravity force was compensated by applying an external electric field with a strength of 10 V/cm. The system featured large regions of particles levitating over a time period of several minutes, exhibiting a short-range order in the spatial structure.

The results of measurements performed using a digitized video image of the structure of these zones, the number density of particles within a 150-μm-thick flat layer was 10^{-7} μm^{-2}. Accordingly, the volume number density of dust particles was $N_p \sim 6 \times 10^4$ cm^{-3}. The average charge of these particles, determined from the balance of gravitational and electrical forces, was $Z_p \approx 400$. The density of the charge of dust particles was $Z_pN_p \sim 2.4 \times 10^7$ cm^{-3}. The ion number density, determined by measuring the current between electrodes and using the known ion drift velocity, was $N_i \sim 10^8$ cm^{-3}.

The charge of dust particles. Using formula (8) and taking the electron temperature equal to the room temperature ($T_e = T \approx 300$ K = 0.026 eV), we obtain $Z_p \approx 100$. This estimate is about one-fourth of the value obtained from the experimental data ($Z_p \approx 400$). Apparently, the discrepancy is related to the fact that the secondary electrons generated by hard ionization cannot rapidly cool and, hence, possess a temperature above the room temperature. Data on the electron energy distribution upon hard ionization can be found, for example, in [6]. Estimates of the mean path length necessary for cooling the electrons to room temperature by mechanism of elastic collisions yield $l_T \sim (10^{-16}$ cm^2 3×10^{19} cm^{-3} $2m_i/m_e)^{-1}$, which is markedly greater than the distance between dust particles ($l_T \sim 10$ cm $\sim 350\ N_i$) in the system studied. Of course, the electron cooling in a molecular gas by means of excitation of the vibrational and rotational degrees of freedom is approximately ten ties more effective than the cooling by elastic collisions. Nevertheless, it is evident that an average electron temperature may be several times greater than room temperature.

Mean number density of ions. In the experiments under consideration, the radioactive source provided ionization at a rate corresponding to 10^9 β-decays per second in a volume of 20 cm^3. Assuming that every β-decay event liberates an energy of $E_f = 138$ eV, we obtain the following estimate for the ionization rate per unit volume:

$$G \sim (10^9\ \text{s}^{-1}/20\ \text{cm}^3)(E_f/E_{pr})N_p \sim 3 \times 10^6\ \text{s}\ N_p \sim 2 \times 10^{11}\ \text{s}^{-1}\ \text{cm}^{-3},$$

where $E_{pr} = 36$ eV is the energy necessary for the ion pair production in air.

The coefficient of ion recombination on dust particles according to Langevin is $\alpha_L = 4\pi Z_p e^2 b_i \sim 0.064$ cm^3 s^{-1}. This estimate is obtained for the ion mobility $b_i = 2/(m_i N k_{ia})$, where $k_{ia} = (4/3)4 \times 10^{-16}$ cm^2 $(8T/\pi m_i)^{1/2} \sim 2.5 \times 10^{-11}$ cm^3/s is the frequency of collisions between ions and air molecules (considered as hard spheres with a cross section of 4×10^{-16} cm^2. Using this value of the ion mobility and Eq. (10), we obtain an estimate for the charge production (ionization) rate of $\alpha_L Z_p N_p \sim 10^{11}$ s^{-1} cm^{-3}, which corresponds to dominating negative charge on the dust particles (i.e., small density of negative ions in the plasma) and agrees in the order of magnitude with the values observed in experiments.

The number density of ions can be estimated by using the dissociative recombination coefficient equal to $\alpha_d \sim 3 \times 10^{-7}$ cm^3/s and taking into account that recombination on the dust particles dominates ($a = \alpha_L/(Z_p\alpha_d) \sim 530$) and the ion number density according to (9) is only twice ($\beta = 2$) as large as the dust particle charge density per unit volume ($Z_pN_p \sim 2.4 \times 10^7$ cm^{-3}). Thus, we obtain an estimate for the number density of ions $N_i \sim 0.5 \times 10^8$ cm^{-3}, which also agrees with the experimental values.

Charge distribution around dust particles. The ion number density and charge distribution around a dust particle were calculated by numerically solving

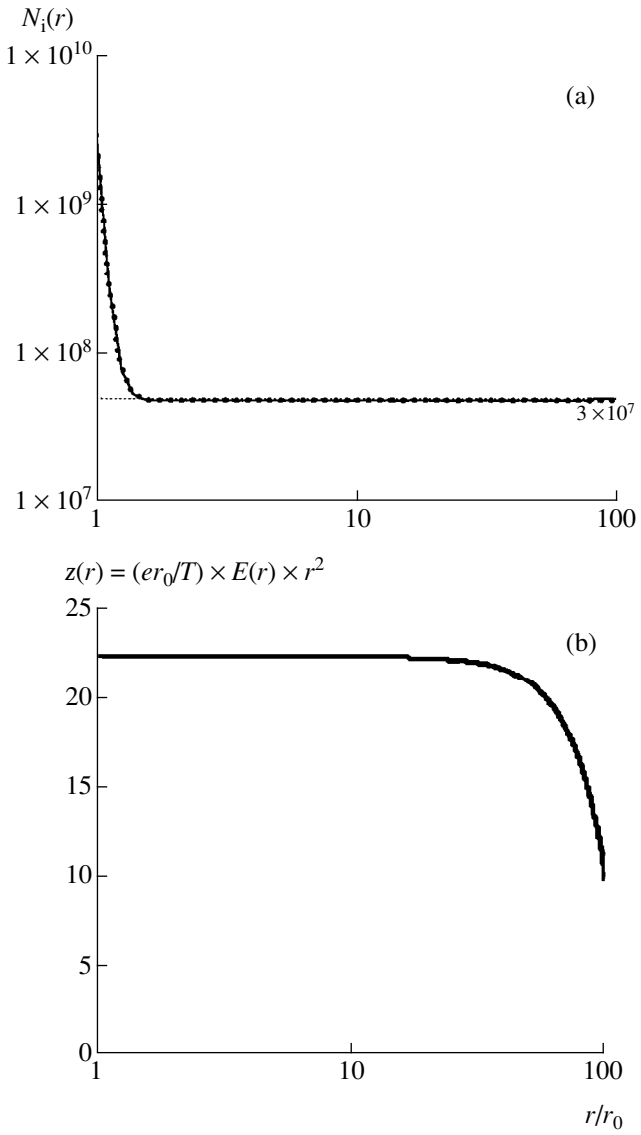

Fig. 1. Plots of the (a) ion number density and (b) reduced total charge inside a sphere versus the distance from a dust particle. Solid cures present the results of rigorous numerical calculation, dashed curves show the estimates obtained by Eq. (5) for $r_0 = 0.5$ μm and $z_0 = Z_p(e^2/r_0T) = 22.3$.

Eqs. (2) with the boundary conditions (3) and (4). The ion number density (Fig. 1a) agrees well with the approximate solution (5). This is explained by the fact that the particle charge shielding (Fig. 1b) becomes significant only at sufficiently large distances corresponding to about half of the average spacing between dust particles (over which range the integration was performed). The radius-average ion number density coincides with the value given by formula (9).

Conclusion

Thus, the proposed theory of the charge recombination in a dust plasma ionized by a hard factor provides characteristics that are in a good agreement with experimental data. The theory reveals one of the main reasons for manifestation of the collective properties in the dust plasma. A criterion for this is that a considerable proportion of charges of one sign must concentrate on the surface of dust particles. Once this condition is fulfilled, charges of the opposite sign form clouds around the dust particles that account for the forces of mutual attraction between the particles [4]. In a thermoemissive dust plasma, the particles bear a positive charge, which is compensated by thermoemission electrons [3–5]. In a dust plasma produced by a hard ionization source, only a special relationship between the number density of particles and the ionization rate (10) may allow the above condition to be fulfilled. A similar requirement (for the man charge to be carried by dust particles) would probably account for manifestation of the collective properties in a gas-discharge-ionized dust plasma.

REFERENCES

1. V. E. Fortov, V. I. Vladimirov, L. V. Deputatova, *et al.*, Dokl. Akad. Nauk **336** (2), 184 (1999) [Phys. Dokl. **44**, 279 (1999)].
2. A. N. Tkachev and S. I. Yakovlenko, Zh. Tekh. Fiz. **69** (1), 53 (1999) [Tech. Phys. **44**, 48 (1999)].
3. A. N. Tkachev and S. I. Yakovlenko, Pis'ma Zh. Tekh. Fiz. **25** (1), 52 (1999) [Tech. Phys. Lett. **25**, 21 (1999)].
4. S. I. Yakovlenko, Pis'ma Zh. Tekh. Fiz. **25** (16), 83 (1999) [Tech. Phys. Lett. **25**, 670 (1999)].
5. S. I. Yakovlenko, Pis'ma Zh. Tekh. Fiz. **26** (8), 47 (2000) [Tech. Phys. Lett. **26**, 337 (2000)].
6. L. I. Gudzenko and S. I. Yakovlenko, *Plasma Lasers* (Atomizdat, Moscow, 1978).
7. S. I. Braginskiĭ, in *Reviews of Plasma Physics*, Ed. by M. A. Leontovich (Gosatomizdat, Moscow, 1963; Consultants Bureau, New York, 1963), Vol. 1.
8. J. B. Hasted, *Physics of Atomic Collisions* (Butterworths, London, 1964; Mir, Moscow, 1965).
9. E. W. McDaniel, *Collision Phenomena in Ionized Gases* (Wiley, New York, 1964; Mir, Moscow, 1967).
10. V. L. Granovskiĭ, in *Electric Current in a Gas* (GITTL, Moscow, 1952), Vol. 1.

Translated by P. Pozdeev

Technical Physics Letters, Vol. 26, No. 12, 2000, pp. 1049–1052. Translated from Pis'ma v Zhurnal Tekhnicheskoĭ Fiziki, Vol. 26, No. 23, 2000, pp. 47–54.

Self-Excited Oscillation Processes in Porous-Silicon-Based Structures

A. N. Laptev, A. V. Prokaznikov, and N. A. Rud'

Yaroslavl State University, Yaroslavl, Russia;

e-mail: prok@iman.yaroslavl.su

Received June 27, 2000

Abstract—It was found that the dynamic current–voltage (*I–U*) characteristics of the *n*-type porous-silicon-based structures upon prolonged room-temperature storage exhibit negative differential conductivity. Exposure of the samples to a vapor of polar molecules led to the development of self-excited oscillations both during the *I–U* measurements and in the course of reverse current relaxation in the structure studied. The observed effects are explained by the formation of deep surface energy levels and their charging by an electric current passing upon exposure to the atmosphere containing polar molecules. © *2000 MAIK "Nauka/Interperiodica".*

The main attention of researchers engaged in the properties of porous silicon (por-Si) and related structures is traditionally devoted to the photoluminescence (PL) and electroluminescence (EL) phenomena and their dependence on the conditions of por-Si preparation and the structure and quality of the resulting porous semiconductor layers and metal contacts. Investigations of the electrical properties of the por-Si based structures are of importance for better understanding the EL process as such and the related charge transfer phenomena in por-Si.

Previously [1, 2], we reported on the hysteresis observed on both forward and reverse branches of the dynamic current–voltage (*I–U*) characteristics of the *p*- and *n*-type por-Si based structures possessing EL properties. Later [3], it was established tat this hysteresis is also observed in PL-active por-Si structures of the *p*-type. The hysteresis behavior was explained by the presence of slow traps for the major charge carriers in por-Si. Subsequent investigations showed that the hysteresis parameters depend to a considerable extent on the molecular properties of surrounding medium.

As is known, the action of molecules (atoms) of certain kind may significantly change the dynamics of processes taking place in various systems. Recently, Bernatskiĭ and Pavlov [4] reported on the self-excited oscillatory phenomena observed during the continuous field desorption of alkali metals (K, Cs) from a gold-coated tungsten surface. Fujii *et al.* [5] observed a negative conductivity region in the *I–U* curves of a nanofilament type structure exposed to air and explained this phenomenon by the presence of surface states related to the adsorption of water molecules.

Below we report on the results of investigation of the *I–U* characteristics and the reverse current relaxation in the *n*-type por-Si based structures upon prolonged (several months) storage in atmosphere with a relate humidity of 50–70%; also reported are the effects of polar molecules present in the atmosphere on the surface states in por-Si.

The pr-Si layers were prepared by method of electrochemical anodizing in single-crystal (100)-oriented *n*-Si wafers of the KEF-20 grade [6, 7]. A special technology used for obtaining por-Si samples possessing EL properties [2, 8, 9] involved two important aspects: controlled reproducible formation of the structure with a special por-Si layer morphology and the final EL structure creation by a special laser treatment of this layer.

A por-Si material of the B_5 type (the notation according to [2]) was used to prepare the sample structures of two types. The "dot" type (DT) structures contained a network of equidistant 20-μm-diam holes at a 100-μm step in the por-Si film. In the "square" type (ST) structures, the analogous network was formed by square holes with a side length of 20 μm spaced by the same distance. The upper contact represented a Pt layer on which the EL pattern was applied by the direct laser drawing technique. The structures of two types exhibited different characteristics. The DT structures had a visible emission switch-on potential of $U \approx 20$ V at $I \approx 30$ mA and showed a moderately bright uniform pale-blue emission. The DT sample resistance measured with a current passing across the structure (sandwich geometry) was on the order of $r_{\uparrow}^{(\bigcirc)} \cong 21$ kΩ for the negative Pt electrode potential (reverse bias) and $r_{\downarrow}^{(\bigcirc)} \cong 9.4$ kΩ for the "plus" sign on Pt (forward bias). The ST structures had $U \approx 50$ V at $I \approx 10$ mA and showed a nonuniform pale blue emission accompanied with bright red scintillations. The ST sample resistances measured in the sandwich geometry were $r_{\uparrow}^{(\square)} \cong 346$ kΩ (reverse bias) and $r_{\downarrow}^{(\square)} \cong 28.4$ kΩ (forward bias). These data

give evidence that the structures of both types contain insulating layers. However, the ST samples had apparently a greater thickness of this layer, as evidenced by higher values of the sample resistance and the visible emission switch-on potential at a lower current [8, 9].

The *I–U* characteristics of the samples were measured in a dynamic regime by applying a periodic linear +10 to –10 V sweep voltage. The sweep period could be varied from 10 to 10^3 s. As noted above, we have previously observed a hysteresis in the *I–U* curves of similar por-Si based structures [1, 2]. The hysteresis was relatively more pronounced for the reverse current (with more negative or positive potential applied to the single-crystal *p*- or *n*-Si contact, respectively, relative to the upper contact) than for the forward current. In addition, the reverse current hysteresis significantly depended on the sample prehistory, that is, on the charge previously transferred via the sandwich structure with forward current and on the reverse bias variation rate. Should the voltage sweep begin with application of a reverse bias, there is almost no hysteresis in the reverse current. At the same time, the forward current hysteresis was virtually independent of the prehistory.

We explain this behavior by trapping of the major charge carriers (electrons and holes in the *n*- and *p*-Si, respectively) on deep surface levels during the forward current passage, followed by their emission from the traps. This mechanism was quite sufficient to explain the *I–U* cures observed for the periodic linear bias variation. When the bias decreases (irrespective of the prehistory), the forward current may only be greater than that observed with increasing bias. For the reverse current, the pattern is opposite: the current is lower for decreasing than for increasing bias. A similar behavior of the dynamic *I–U* curves was previously observed for various EL structures based on both *n*- and *p*-Si [1, 2, 8, 9].

A prolonged (several months) storage of the *n*-type por-Si based structures at room temperature, normal pressure, and a relative humidity of 50–70% markedly changed the *I–U* curves of some samples. In B_5 por-Si structures of the "dot" type, the reverse-bias part of the *I–U* curves acquired a clearly pronounced region of negative differential conductivity (NDC) (Fig. 1b). The NDC region was observed in the 2I–*V* curves measured for various voltage sweep periods between 10 and 10^3 s. It was found that the NDC region appears in the reverse-bias part of the *I–U* characteristic only upon passage of the forward current, otherwise no such region in the reverse bias branch is observed (Fig. 1a). As is known, the presence of NDC may always give rise to oscillatory processes, provided a negative feedback exists in the system. Such an *I–U* curve with NDC was observed for a specially prepared silicon-on-insulator (SOI) air-bridge-type structure in [5], where the current relaxation in this system was studied at various bias voltages. The relaxation behavior was different for the bias voltages below and above a critical value V_p corresponding to the appearance of the NDC region in the *I–U* curves.

We have also studied the reverse current relaxation process upon switching the system from forward to reverse bias, preceding the appearance of the NDC region. Figure 2b shows a typical plot of the relaxation current versus time. Our investigations showed that the relaxation character depends very weakly on the reverse bias voltage. However, the relaxation current value at the instant of the bias sign reversal was affected by the forward bias magnitude. It should be noted that the current relaxation process includes a fast component (with a characteristic time below one second) and a slow component (with the characteristic times from a few seconds to several minutes). The forward current relaxation upon the bias sign reversal in the por-Si structure was also reported in [10], where the phenomenon was explained by the charging of deep levels present at the por-Si–SiO_2 interface.

Thus, all the investigations of dynamic *I–U* characteristics, as well as the direct and reverse current relaxation, in por-Si structures are indicative of a significant influence of the deep levels (acting as traps for the major carriers) that can be present both in por-Si proper and at the interface between por-Si and silicon oxide layers. Therefore, it is possible to affect these states by exposure to a medium containing polar molecules. Apparently, owing to some special features of the preparation procedure favoring the NDC manifestation, the por-Si structures are subject to considerable influence of the polar molecules (most probably, water) from atmosphere.

In order to verify this hypothesis, we placed a sample por-Si structure with NDC into an atmosphere containing ether molecules known to possess a greater dipole moment as compared to that of water molecules. We believed that these polar molecules would exhibit a stronger influence upon the surface states in por-Si and, hence, a pronounced effect on the electrical properties of samples will be observed in a shorter time. Indeed, a 1.5–2 h exposure produced a dramatic change in the *I–U* characteristics of the sample structures. Figure 1c shows a typical plot of the reverse current versus bias voltage measured upon the forward current passage (a sweep period was about 100 s). The *I–U* curve exhibits clearly manifested pronounced oscillations in the reverse current, which develop at a reverse bias voltage of $U \geq 5$ V and increase in amplitude with the absolute value of the bias voltage. The oscillations are most pronounced in the reverse branch (dashed curve in Fig. 1c). Note that the decay of oscillations in the reverse branch is observed at a lower bias value than their appearance in the forward branch. Since the *I–U* measurements involve a change in the bias voltage with time (sweep), we did not observe periodic oscillations of the reverse current in time. However, measurements of the reverse current relaxation upon the bias switching from forward ($U = +10$ V) reverse ($U \geq 5$ V) mode revealed a

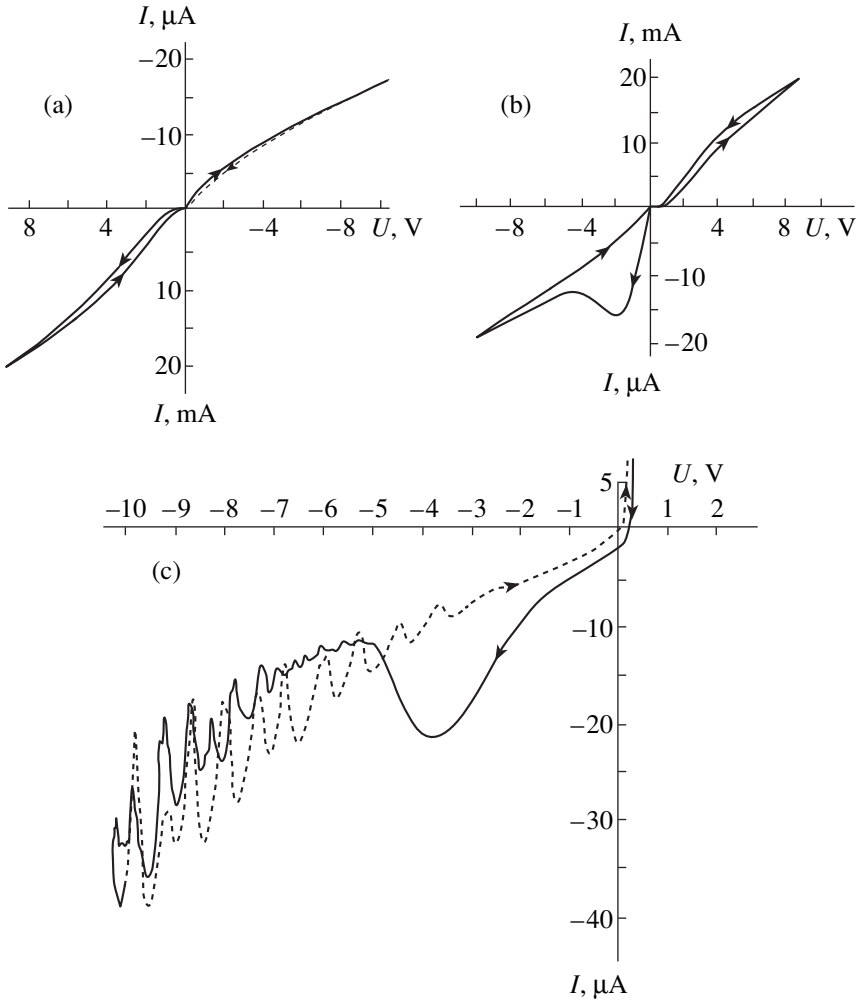

Fig. 1. The *I–U* curves of electroluminescent por-Si structures measured in air for the bias varied (a) from reverse (plus on Si, minus on Pt) to forward and (b) from forward (minus on Si, plus on Pt) to reverse; curve (c) was measured under the same conditions as (b) upon exposure to the air containing polar molecules.

pattern of strictly periodic oscillations of the reverse current with increasing amplitude at a fixed reverse bias (Fig. 2a). However, no such oscillations in the reverse current were observed at a bias voltage below 5 V, although the current relaxation still exhibited a rather complicated pattern (Fig. 2c). Note that the reverse current relaxation at a reverse bias of 4.5 V is apparently related to different mechanisms.

Let us briefly consider a theoretical model explaining the observed phenomenon. Molecules adsorbed from the atmosphere tend to build in a certain manner into the dielectric layer, thus forming the surface centers capable of changing their charged state under the action of either an external field or the adsorbed polar molecules. The results of our experiments (Figs. 1a and 1b) indicate that these surface states may lose electrons and acquire a positive charge under the action of an applied electric field of definite polarity. No such a charging of the surface states takes place for the reverse polarity (Figs 1a and 1b). This behavior allows us to judge the sign of charging of the surface states under the action of a definite polarizing field.

The number of surface states is sufficiently large, as evidenced by the depth of the "well" observed in the hysteresis curve (Fig. 1b). When the voltage polarity is changed and the charged states begin to operate, the reverse branch of the *I–U* curve exhibit the corresponding "bag." At a relative small potential, a part of electrons from adsorbed polar molecules occupy the surface states by tunneling. As a result, the polar molecules acquire a positive charge. As the potential increases, the surface states are gradually filled and the *I–U* curves exhibit a maximum current The value of the potential at this maximum corresponds to the optimum conditions for electron tunneling from polar molecules to the surface centers. When the most part of the surface centers is filled, the current begins to decrease with increasing potential and the *I–U* curve exhibits a region with negative differential conductivity. Here, the trapped charges leave the surface centers by diffusion

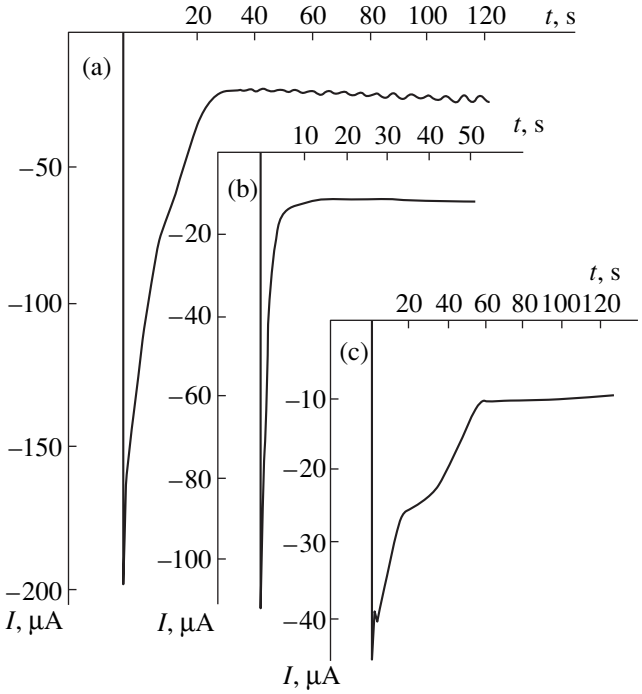

Fig. 2. The Time relaxation of the reverse current upon the bias switching from forward to reverse in the samples exposed to the air containing polar (ether) molecules: (a) $U \geq 5$ V; (c) $U \approx 4.5$ V; curve (b) was measured for $U =$ 10 V without additional exposure to polar molecules.

via the surface states (cf. [4]). For this mechanism to be operative, the system must possess a sufficiently large number of active surface states capable of accepting charge carriers of a definite sign, which is provided by applying a potential difference of certain polarity in the initial stage. The molecules charged in this activated manner desorb from the surface to leave the adsorption sites for the adsorption of new species and the process outlined above is continuously repeated.

In concluding, it should be noted that the proposed theoretical model admits analytical description. The results of this investigation, including a theoretical analysis, will be reported in more detail in further publications.

REFERENCES

1. A. N. Laptev, A. V. Prokaznikov, and N. A. Rud', Pis'ma Zh. Tekh. Fiz. **23** (11), 59 (1997) [Tech. Phys. Lett. **23**, 440 (1997)].
2. É. Yu. Buchin, A. N. Laptev, A. V. Prokaznikov, *et al.*, Pis'ma Zh. Tekh. Fiz. **23** (11), 70 (1997) [Tech. Phys. Lett. **23**, 445 (1997)].
3. É. B. Kaganovich, É. G. Manoĭlov, and S. V. Svechnikov, Fiz. Tekh. Poluprovodn. (St. Petersburg) **33** (3), 327 (1999) [Semiconductors **33**, 327 (1999)].
4. D. P. Bernatskiĭ and V. P. Pavlov, Pis'ma Zh. Tekh. Fiz. **26** (6), 22 (2000) [Tech. Phys. Lett. **26**, 233 (2000)].
5. H. Fujii, S. Kanemaru, T. Matsukawa, and J. Itoh, Jpn. J. Appl. Phys. **38**, 7237 (1999).
6. É. Yu. Buchin and A. V. Prokaznikov, Pis'ma Zh. Tekh. Fiz. **23** (6), 1 (1997) [Tech. Phys. Lett. **23**, 210 (1997)].
7. É. Yu. Buchin and A. V. Prokaznikov, Pis'ma Zh. Tekh. Fiz. **23** (6), 80 (1997) [Tech. Phys. Lett. **23**, 244 (1997)].
8. Yu. E. Babanov, A. V. Prokaznikov, N. A. Rud', and V. B. Svetovoĭ, Phys. Status Solidi A **162**, R7 (1997).
9. Yu. E. Babanov, E. Yu. Buchin, A. V. Prokaznikov, *et al.*, Phys. Low-Dimens. Struct. **7-8**, 77 (1999).
10. C. Cadet, D. Deresmes, D. Vuillaume, and D. Stlevenard, Appl. Phys. Lett. **64** (21), 2827 (1994).

Translated by P. Pozdeev

Technical Physics Letters, Vol. 26, No. 12, 2000, pp. 1053–1054. Translated from Pis'ma v Zhurnal Tekhnicheskoĭ Fiziki, Vol. 26, No. 23, 2000, pp. 55–58.

Optical Absorption in Cobalt-Containing Epitaxial Films of Gadolinium Gallium Garnet

V. V. Randoshkin, N. V. Vasil'eva, V. G. Plotnichenko, and Yu. N. Pyrkov

Joint Laboratory of Magnetooptoelectronics, Institute of General Physics, Russian Academy of Sciences, Mordovian State University, Saransk, Mordovia, 430000 Russia

Optical Research Center, Institute of General Physics, Russian Academy of Sciences, Moscow, 117942 Russia

Received July 3, 2000

Abstract—The optical absorption of di- and trivalent cobalt ions embedded in single-crystalline films of gadolinium gallium garnet was observed in the samples grown by liquid-phase epitaxy from supercooled solution melts based on $PbO–B_2O_3$ and $PbO–B_2O_3–GeO_2$ systems. *© 2000 MAIK "Nauka/Interperiodica".*

Single crystals of $MgAl_2O_4$ doped with Co^{2+} ions can be used as saturable absorption filters in the near-infrared (NIR) lasers [1]. This is due to the existence of a broad absorption band in the $\lambda = 1.3–1.6$ μm wavelength range in these materials.

The purpose of this study was to examine the possibility to achieve similar effect with single-crystalline films of gadolinium gallium garnet (GGG) doped with cobalt ions. To do this, cobalt-containing garnet films were synthesized by liquid-phase epitaxy from supercooled solution melts and their optical absorption spectra were measured. The films were grown on $Gd_3Ga_5O_{12}$ (GGG) (111)-oriented substrates from $PbO–B_2O_3$ (**I**) and $PbO–B_2O_3–GeO_2$ (**II**) solution melts. To provide for the charge compensation [2] in the first case, cobalt should be mainly in the trivalent state; only a small number of Co^{2+} ions can be present, to compensate for the charge of Pb^{4+} and Pt^{4+} impurity ions incorporated into the film from the solution melt. In the second case, cobalt ions should occur in the divalent state to compensate for the charge of Ge^{4+} ions, which are mainly incorporated into a tetrahedral sublattice of the garnet lattice.

The composition of solution melt **I** is determined by the molar ratios

$$R_1 = (Ga_2O_3 + Co_3O_4)/Gd_2O_3 \approx 14.42,$$

$$R_2 = PbO/B_2O_3 \approx 16.03,$$

$$R_3 = (Gd_2O_3 + Ga_2O_3 + Co_3O_4)/(Gd_2O_3 + Ga_2O_3 + Co_3O_4 + PbO + B_2O_3) \approx 0.08,$$

$$R_4 = Ga_2O_3/Co_3O_4 \approx 9.00;$$

the composition of solution melt **II** is determined by the ratios

$$R_1 = (Ga_2O_3 + GeO_2 + Co_3O_4)/Gd_2O_3 \approx 30.77,$$

$$R_2 = PbO/B_2O_3 \approx 16.03,$$

$$R_3 = (Gd_2O_3 + Ga_2O_3 + GeO_2 + Co_3O_4)/(Gd_2O_3 + Ga_2O_3 + GeO_2 + Co_3O_4 + PbO + B_2O_3) \approx 0.15,$$

$$R_4 = (Ga_2O_3 + GeO_2)/Co_3O_4 \approx 20.35.$$

The films grown from solution melt **I** were colored green and those grown from solution melt **II** were blue, which indicates that the cobalt ions incorporated into these films occur in different valence states. Parameters characterizing the film growth process are presented in the table, where T_g denotes the growth temperature, t_g the growth duration, and f_g the growth rate. For comparison, data regarding the film grown from solution melt **III**, based on a $PbO–B_2O_3$ system without cobalt [3], are also included.

The film thickness h was determined by weighing the substrate before and after the epitaxial growth [3, 4]. As in [4], a difference between the densities of the film and the substrate was neglected. The transmission spectra of the films were recorded with a Perkin-Elmer Lambda 900 spectrophotometer.

The figure represents transmission spectra of the films grown from solution melts **I**, **II**, and **III** (curves *1*, *2*, and *3*, respectively) and of the GGG substrate (curve *4*). One can see that sample 1 (see table) has a broad absorption band in the IR range at $\lambda = 0.9–1.63$ μm

Growth parameters of epitaxial single-crystalline films

Sample no.	Solution melt	T_g, °C	t_g, min	f_g, μm/min	$2h$, μm
1	**I**	937	60	0.8	92.3
2	**II**	874	120	0.2	44.6
3	**III**	914	10	0.8	15.9

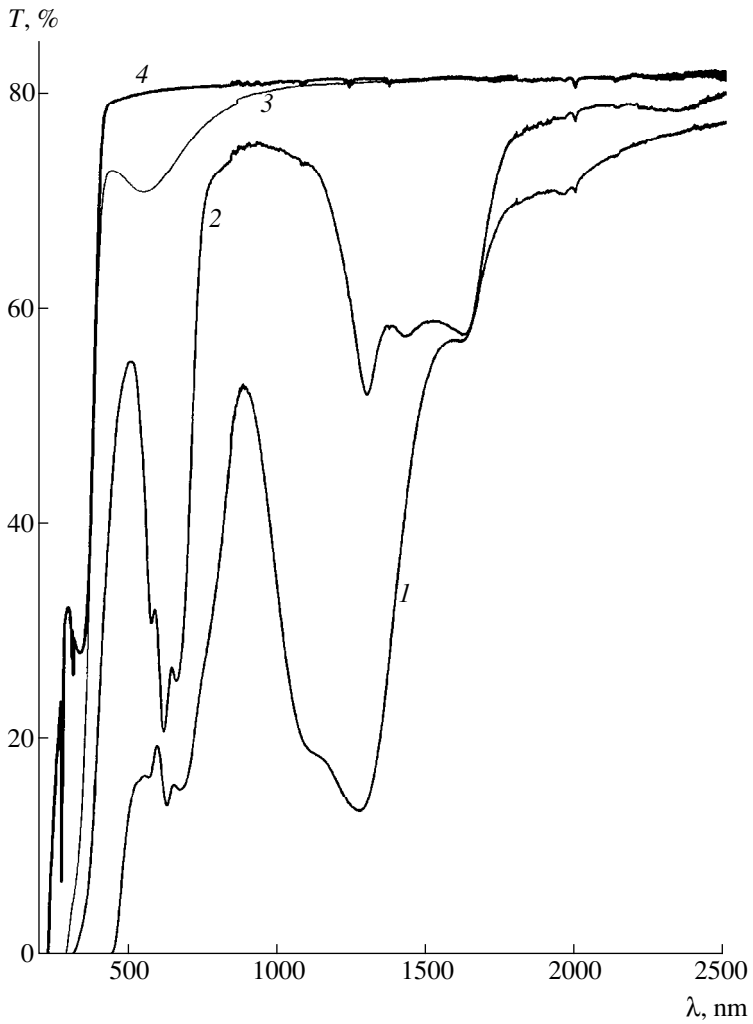

Spectra of the optical transmission $T(\lambda)$ for epitaxial films with the nominal compositions (*1*) $Gd_3(Ga, Co)_5O_{12}$, (*2*) $Gd_3(Ga, Ge, Co)_5O_{12}$, and (*3*) $Gd_3Ga_5O_{12}$ and (*4*) for the undoped $Gd_3Ga_5O_{12}$ substrate.

centered at $\lambda = 1273$ nm and relatively weak absorption peaks in the visible range centered at $\lambda = 565$, 626, and 670 nm. These absorption features can be related only to Co^{3+} ions. Sample 2 (see table) has a broad absorption band in the $\lambda = 1.2$–1.7 μm wavelength range and weak absorption peaks centered at $\lambda = 573$, 615, and 658 nm, the absorption minimum being at $\lambda = 504$ nm. As in [1], this broad absorption band can be attributed to transitions from the ground state $^4A_2(^4F)$ to the $^4T_1(^4F)$ state of the Co^{2+} ion. The short-wavelength edge in the transmission spectra of the films with the nominal compositions $Gd_3(Ga, Co)_5O_{12}$ (curve *1*) and $Gd_3(Ga, Ge, Co)_5O_{12}$ (curve *2*) is shifted to longer waves, as compared toward the substrate (curve *4*) and the film with the nominal composition $Gd_3Ga_5O_{12}$ (curve *3*).

Thus, it is shown in this study that epitaxial cobalt-containing single-crystalline films of gadolinium gallium garnet exhibit optical absorption that is necessary to create saturable absorption filters for the IR range.

Acknowledgments. The authors are grateful to A.V. Vasil'ev, M.I. Belovolov, and V.A. Mikhaĭlov for their help in carrying out this study and the discussion of results.

REFERENCES

1. B. I. Galagan, E. A. Godovikova, B. I. Denker, *et al.*, Kvantovaya Élektron. (Moscow) **26** (3), 189 (1999).
2. V. V. Randoshkin and A. Ya. Chervonenkis, *Applied Magnetooptics* (Énergoatomizdat, Moscow, 1990).
3. V. V. Randoshkin, N. V. Vasil'eva, A. M. Saveletskiĭ, and N. N. Sysoeva, Pis'ma Zh. Tekh. Fiz. **25** (17), 18 (1999) [Tech. Phys. Lett. **25**, 683 (1999)].
4. V. V. Randoshkin, A. M. Belovolov, M. I. Belovolov, *et al.*, Kvantovaya Élektron. (Moscow) **25** (3), 233 (1998).

Translated by M. Skorikov

Technical Physics Letters, Vol. 26, No. 12, 2000, pp. 1055–1057. Translated from Pis'ma v Zhurnal Tekhnicheskoĭ Fiziki, Vol. 26, No. 23, 2000, pp. 59–65.

Copper in α-C:H Films: Low Temperatures

T. K. Zvonareva, V. I. Ivanov-Omskiĭ, and K. F. Shtel'makh

Ioffe Physicotechnical Institute, Russian Academy of Sciences, St. Petersburg, 194021 Russia

St. Petersburg State Technical University, St. Petersburg, Russia

Received June 29, 2000

Abstract—Microwave power absorption in copper-modified α-C:H films (maximum copper content, 8%) was studied in the 3.8–20 K temperature range. The EPR spectrum is interpreted as being due to a strongly anisotropic absorption of isolated paramagnetic copper centers. A model for the formation of paramagnetic copper centers involving oxygen atoms is proposed. At temperatures above 18 K, the system exhibits a nonresonance absorption of the microwave power. The temperature dependence of this absorption signal is described by an exponential law with the parameter $\Delta E = 250 \pm 30$ K. This temperature dependence is explained assuming the existence of copper nanoclusters. The ΔE value can be considered as the depth of an energy well corresponding to the nanocluster formation. © *2000 MAIK "Nauka/Interperiodica".*

In recent years, a considerable interest of researchers is drawn to the encapsulation of metal nanoclusters in various media capable of protecting the metal particles from aggressive external media [1]. The possibilities of using amorphous hydrogenated carbon (α-C:H) as a universal material for protective coatings are well known, being favored by the high strength, excellent optical transparency in a broad spectral range, and chemical inertness of this material. Owing to the unique ability of carbon to exhibit different types of hybridization of the valence atomic orbitals, the α-C:H structure may accommodate various foreign inclusions, the metal nanoclusters among these. The purpose of this study was to identify the states of copper atoms, incorporated into the α-C:H films, by the EPR spectroscopy techniques.

The copper-modified α-C:H films were prepared as described elsewhere [2]. In order to decrease the probability of interaction between copper atoms, we have preliminarily selected the samples characterized by a minimum concentration of copper atoms. Data on the compositions of modified layers determined by the method of Rutherford backscattering (RBS) are presented in Table 1.

The EPR measurements were carried out on a Bruker ER220D X-band (3 cm) spectrometer in a temperature interval from 3.8 to 25 K. The samples were prepared as single layers with thicknesses ranging from 1 to 10 μm grown on sapphire and silicon substrates.

The results of our EPR measurements can be summarized as follows. At low temperatures, the EPR spectrum exhibits a single line with the parameters $g = 2.149 \pm 0.002$ and $\Delta H_{pp} = 25 \pm 3$ G. The line intensity variation with the temperature increasing up to $T \cong 18$ K is well described by the Curie law (Fig. 1). As the temperature approaches $T \sim 20$ K, the samples exhibit a nonresonance anisotropic absorption of the microwave power: a change in the sample orientation from parallel to perpendicular relative to the magnetic field, the intensity of absorption increases by a factor of 4. The temperature dependence of the nonresonance microwave absorption intensity (measured by the peak height) can be described (irrespective of the copper concentration) by an exponential law with the parameter $\Delta E = 250 \pm 30$ K (Fig. 2). It should be noted that the EPR measurements could not be conducted at temperatures above 25 K because of the extremely high intensity of the nonresonance absorption.

Data on the relative concentration C of the paramagnetic centers determined at $T = 8$ K and the intensity I of the nonresonance microwave absorption (reduced to the unit volume) are presented in Table 2. For comparison, Table 2 also gives the copper concentrations C_{Cu} determined by the Rutherford backscattering technique.

Thus, the results of our EPR measurements indicate that modification of the α-C:H layers with copper results in the appearance of paramagnetic centers. The results of analyses of the copper-modified samples suggest that the introduction of copper in large amounts leads to the formation of inclusions, which explains the

Table 1. Elemental compositions of the copper-modified α-C:H films (at. %) determined from the Rutherford backscattering data

Sample no.	Copper, at. %	Oxygen, at. %	Hydrogen, at. %	Carbon, at. %
325	0.2	7	24	68.8
365	1	7	24	68
366	8	17	24	51

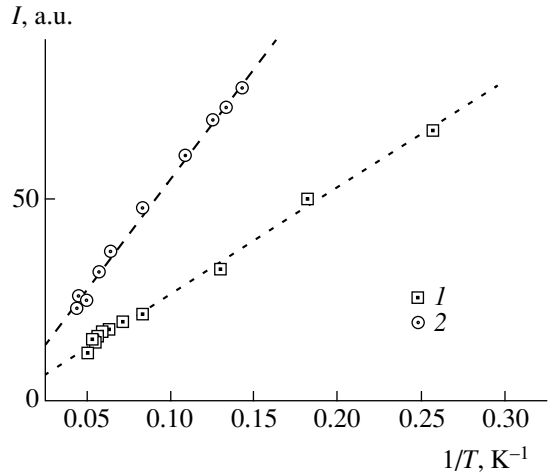

Fig. 1. Temperature variation of the EPR signal intensity from copper-modified α-C:H samples (*1*) no. 325 and (*2*) no. 365.

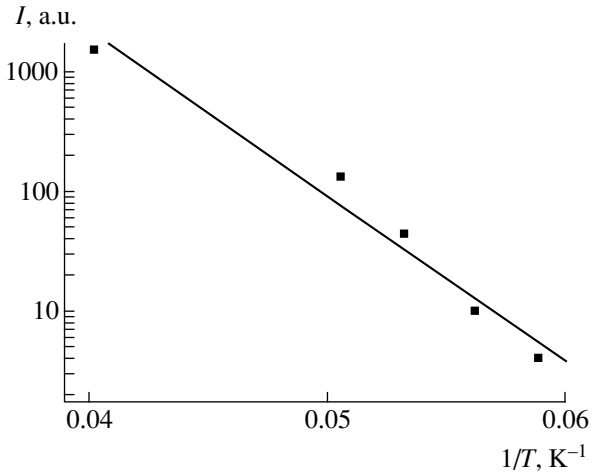

Fig. 2. Temperature variation of the nonresonance microwave absorption intensity in copper-modified α-C:H sample no. 365.

nonresonance microwave absorption. Taking into account the angular dependence (anisotropy) of this absorption intensity and the electron-microscopic data (Fig. 3), we may suggest that the nonresonance microwave absorption is related to the conduction channels oriented perpendicularly to the carbon layer. The activation energy of the nonresonance absorption should be considered as an average quantity characterizing the probability of the charge carrier jumping between metal inclusions.

An analysis of data on variation of the resonance (EPR signal) and nonresonance microwave absorption intensity with the copper concentration (Table 2) shows that a growth of the copper content is accompanied by saturation of the concentration of paramagnetic centers and gradual increase in the concentration of inclusions. It should be noted that, despite a considerable intensity of the nonresonance microwave absorption and, hence, a large content of copper entering into the inclusions, no EPR signals due to copper atoms in this state were detected. This implies that copper in the inclusions occurs in a diamagnetic state with an electron configuration of the $3d^{10}$ or $3d^{10}4s^2$ type.

Although the structure of inclusions cannot be determined from EPR data, we may suggest that the inclusions represent graphite fragments chemically bound to copper atoms. In this context, we may compare the results of calculations [3] and experimental measurements of the temperature dependence of the nonresonance microwave absorption intensity. Representing an inclusion by a rectangular potential well possessing a single discrete energy level and taking the electron activation energy from [4], we may determine the well power as $aU_0 = 6.4 \times 10^{-5}$ μm eV, where a and U_0 are the well size and depth, respectively. Taking the well dimensions equal to a characteristic graphite ring size $a = 3.8 \times 10^{-4}$ μm, we obtain an estimate $U_0 = 0.17$ eV. According to the results of calculations [3], the energy of a copper atom binding to a single graphite ring is 0.67 eV. However, if the graphite fragment entering into the inclusion contains several copper atoms bound to the rings, the electron activation energy must decrease due to the tunneling induced level spitting in the well. As a result, the electron binding energy in the fragment will decrease to the above U_0 value.

Table 2. Comparative data on the concentrations of paramagnetic centers (EPR data), nonresonance microwave absorption intensity (T = 20 K), and total copper content (RBS data) in the α-C:H films studied

Sample no.	C, 10^{20} cm^{-3}	C_{Cu}, at. %	I, arb. units
325	1.5	0.2	4.5
365	14.6	1	207
366	13.2	8	645

It is a more difficult task to explain the nature of the paramagnetic impurity centers. The observed EPR spectrum is due to isolated centers, which is indicated by the observed temperature variation of the EPR signal intensity. If this spectrum were due to the clusters of exchange-coupled copper ions, we would have to conclude that, first, the exchange integral is extremely high and, second, only the clusters containing an odd number of ions are observed. This is hardly probable, even for a considerable (Table 1) impurity concentration [5]. Taking into account a considerable shift of the g value, we may ascertain that the paramagnetic centers represent Cu^{2+} ions. In order to interpret the observed temperature variation of the EPR signal intensity, we have to explain the freezing of the orbital momentum in copper ions. This can only be done assuming the formation of bonds between these ions and either matrix elements

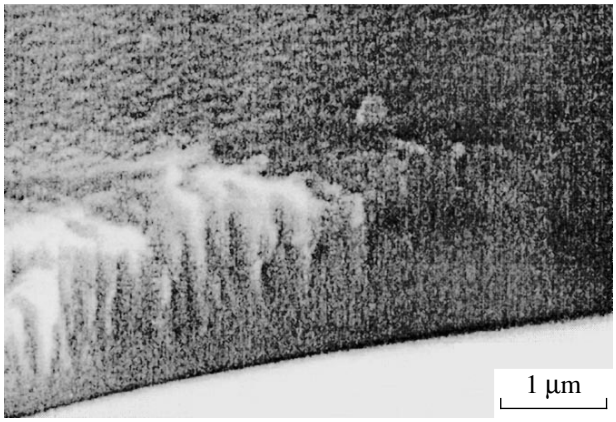

Fig. 3. Image of a cleaved α-C:H film sample obtained in a scanning electron microscope, showing a texture with predominant orientation along the normal to the film surface.

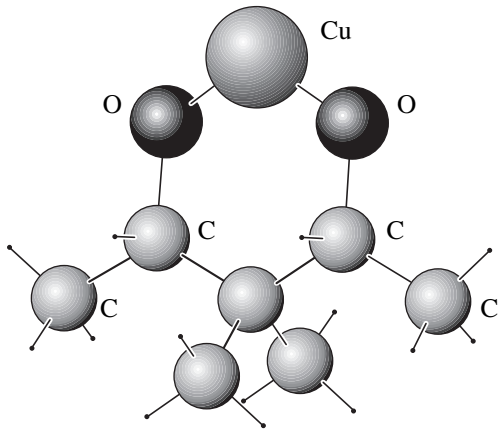

Fig. 4. One of the most probable variants of bonding between a copper atom and a graphite fragment in the α-C:H film. Copper occurs in a paramagnetic state.

or some other impurity. By analogy with the states of copper known in the coordination compounds [6], we may suggest that copper atoms interact with carbons via oxygen (bridging) rather than directly (this is indicated by the data of layer analysis). Because of a considerable electronegativity of oxygen, the ion copper is subject to action of a strong crystalline fed of low symmetry (Fig. 4). An alternative variant is offered by the formation of a bridge between carbon chains or some other low-dimensionality structures existing in the grown α-C:H films. In the latter case, the copper–carbon bonds can be distorted as a result of the Jahn–Teller effect.

The action of a strong crystalline field of low symmetry upon the ground state of the Cu^{2+} ion determines primarily the anisotropy of the magnetic moment of this ion [7] and the anisotropy of the spin density in the *d* electron shell. In particular, the *d*-shell spin configuration may become completely axial, whereby the component $A_\perp$ of the hyperfine coupling tensor would approach zero [7]. This assumption provides a quite reasonable explanation of the observed low-temperature EPR spectrum appearing analogous to a powder spectrum, while a transition with $g = 2.149$ should be considered as representing a component corresponding to $g_\perp$. The assumption concerning a strong anisotropy of the hyperfine coupling tensor *A* also explains a small width of this transition, provided the principal axes of the *A* and *g* tensors would coincide. The absence of a contribution due to the parallel component can be understood, taking into account a variety of the possible structural types that may favor freezing of the orbital moment of the copper ion. The line broadening due to the *g*-value scatter is probably not as large, but a considerable difference in the $A_\parallel$ tensor components would account for the additional EPR line broadening and, hence, for a decrease in the line intensity. Here, an additional factor is a very small sample volume (the signal-to-noise ratio during the EPR measurements was ~100 at 3.8 K).

Conclusions. (1) The introduction of copper into amorphous carbon films leads to the appearance of paramagnetic centers, probably, with a structure schematically depicted in Fig. 4. (2) At a sufficiently high concentration, copper atoms bind to graphite fragments and participates in the formation of diamagnetic inclusions, rendering the material textured with a predominant orientation perpendicular to the layer. This texture explains some features in the electric conductivity of copper-modified α-C:H films.

Acknowledgments. The work was partly supported by the Russian Foundation for Basic Research, project no. 00-02-17004.

REFERENCES

1. J. Jiao and S. Seraphin, J. Appl. Phys. **83** (5), 2442 (1998).
2. T. K. Zvonareva, V. I. Ivanov-Omskiĭ, A. V. Nashchekin, and L. V. Sharonova, Fiz. Tekh. Poluprovodn. (St. Petersburg) **34** (1), 96 (2000) [Semiconductors **34**, 98 (2000)].
3. V. I. Ivanov–Omskiĭ and É. A. Smorgonskaya, Fiz. Tekh. Poluprovodn. (St. Petersburg) **32** (8), 931 (1998) [Semiconductors **32**, 831 (1998)].
4. L. D. Landau and E. M. Lifshitz, *Quantum Mechanics: Non-Relativistic Theory* (Fizmatgiz, Moscow, 1963; Pergamon, Oxford, 1977, 3rd ed.).
5. M. M. Kreitman and D. L. Barnet, J. Chem. Phys. **43**, 364 (1965).
6. Yu. V. Yablokov, V. K. Voronkova, and L. V. Mosina, *Paramagnetic Resonance of Exchange Clusters* (Nauka, Moscow, 1988).
7. S. A. Al'tshuler and B. M. Kozyrev, *Electron Paramagnetic Resonance in Compounds of Transition Elements* (Nauka, Moscow, 1972; Halsted, New York, 1975).

Translated by P. Pozdeev

Technical Physics Letters, Vol. 26, No. 12, 2000, pp. 1058–1060. Translated from Pis'ma v Zhurnal Tekhnicheskoĭ Fiziki, Vol. 26, No. 23, 2000, pp. 66–70.

The Optical Characteristics of Plasma Formed by Laser Erosion of $CdGa_2Se_4$ and $CdGa_2S_4$ Crystals

A. K. Shuaibov, I. É. Kacher, and A. I. Dashchenko

Uzhgorod State University, Uzhgorod, Ukraine

Received July 4, 2000

Abstract—The optical emission from fragments formed during a laser-induced erosion of the surface of $CdGa_2Se(S)_4$ single crystals was studied. The laser plasmas were generated by pulsed radiation of a Nd laser with a beam power density of $(1–2) \times 10^9$ W/cm^2. The laser plasma exists in the form of a nucleus with a diameter of 2–3 mm, while no plasma torch is formed in the space above the target surface. In the 200–600 nm spectral range, the main emission lines observed in the spectrum of the plasma obtained from a laser-eroded $CdGa_2Se_4$ crystal corresponded to transitions from the lowest atomic energy levels of Ga(I), as well as to the intense transitions between the electron states of Se(II) and Se(III). The emission spectra of the plasma from a laser-eroded $CdGa_2S_4$ crystal surface exhibited a single intense line at 532.1 nm showing evidence of a prevailing contribution of the S(II) (4*s*–4*p*) transitions. The optical data agree with the results of the mass spectrometric analysis of the laser plasma generated from cadmium thiogallate crystals. The emission characteristics are of interest from the standpoint of the plasma diagnostics and optimization of the technology of laser sputter deposition of thin films with complicated compositions. © *2000 MAIK "Nauka/Interperiodica".*

The crystals of $CdGa_2Se_4$ and $CdGa_2S_4$ chalcogenides, possessing cationic sublattices containing transition elements and ordered defects, are wisely used in practice in both bulk and film devices [1–5]. The chalcogenide films of the best quality are fabricated by laser sputtering of single-crystal cadmium thiogallates in vacuum [6]. However, the need in further increasing the structural and stoichiometric quality of these materials stimulates more detailed investigations into the process of crystal sputtering.

Previously, the laser plasmas generated from $CdGa_2Se(S)_4$ single crystals were studied in much detail by the method of time-of-flight mass spectroscopy [7]. It was established that the plasmas contains elementary ion species, as well as the binary and ternary complex ions. The relative amount of ions in the laser erosion products was maximum for sulfur (or selenium), although calculations of the binding energies of components in the $CdGa_2S(Se)_4$ compounds give the values increasing from Cd to Ga and reaching maximum for sulfur and selenium atoms. Additional information about the main excited and ionized components of the laser plasma can be obtained by spectroscopic techniques. These data would be also of value for optimization of the process of laser sputter deposition and for the better understanding of mechanisms involved in the interaction between pulsed laser radiations and cadmium thiogallate crystals and in the process of film deposition onto various types of substrates. To our knowledge, no data were previously reported on the optical characteristics of such laser plasmas.

Below, we present the results of investigation of the emission spectra of a laser plasma generated from single-crystal cadmium thiogallates under the action of a YAG:Nd^{3+} laser radiation.

The plasmas were generated with the aid of a pulsed-periodic (f = 12 Hz) neodymium laser with a pulse energy of 10–30 mJ and a pulse duration of 20 ns. The laser beam focused onto a target surface produced a bright emitting nucleus with a diameter of 2–4 mm. The emission was taken from a regions spaced by r = 1–2 mm from the target surface. The target crystals were mounted in a vacuum chamber evacuated to a residual pressure of 3–7 Pa. The content of impurities in the chalcogenide single crystals studied did not exceed 10^{-5}–10^{-7}%. The samples were grown by a method similar to that described in [7]. The emission spectra were measured in the 200–600 nm wavelength range using a setup comprising an MDR-2 monochromator, a FEU-106 photomultiplier tube, and a KSP-4 recording amplifier. The registration system was preliminarily calibrated us g the spectra of hydrogen and band lamps [8]. The spectra were interpreted using the reference data [9–12]. The relative intensities of emission lines were measured with an error not exceeding 5%.

Figure 1 shows typical emission spectra of the laser plasma generated from cadmium thiogallates studied in this work. Data on the assignment of the emission lines and their relative intensities (J/k_λ) are given in the table. The maximum number of emission lines was observed in the spectrum of plasma obtained from a $CdGa_2Se_4$ crystal. In this spectrum, the main emission lines corre-

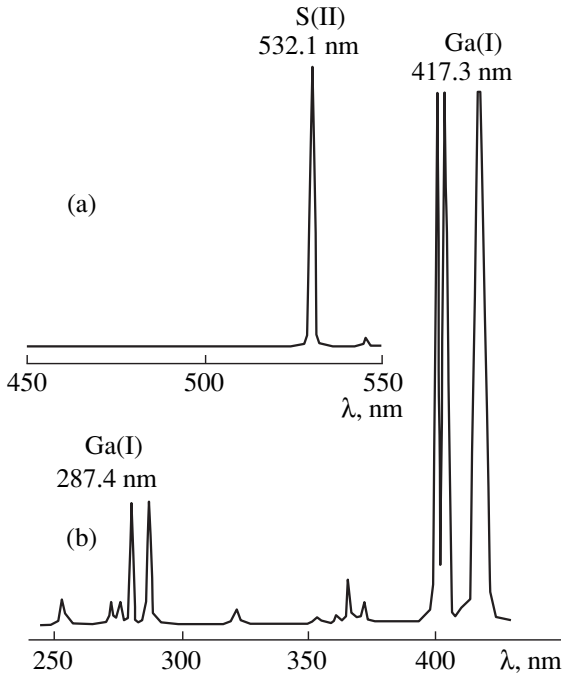

Fig. 1. Emission spectra of laser plasmas generated from the surface of (a) $CdGa_2S_4$ and (b) $CdGa_2Se_4$ single crystals.

sponded to electron transitions from the lowest atomic energy levels of Ga(I), as well as to transitions between the electron states of Se(II) and Se(III). The emission lines of Cd(I) at 372.9, 365.0, 283.7, and 261.7 nm had low intensities. The emission spectra of the laser plasma from a $CdGa_2S_4$ crystal exhibited virtually a single intense line at 532.1 nm showing prevailing contribution of the S(II) ($4s$–$4p$) transitions. A relative intensity of the line with $\lambda = 545.5$ nm corresponding to the $4s^4P_{5/2}$–$4p^4D^0_{7/2}$ transitions in S(I) did not exceed 5% of the intensity of emission at 532.1 nm.

Intensity distribution of the emission spectra of laser plasmas from cadmium thiogallates

λ (nm), atom or ion	Transition	E, eV	J/k, a.u.
	$CdGa_2Se_4$		
417.3 Ga(I)	$4^2P_{3/2}$–$5^2S_{1/2}$	3.07	1.00
406.2 Se(II)+	–	17.84	0.90
404.7 Se(III)	–	19.38	
403.3 Ga(I)	$4^2P_{1/2}$–$5^2S_{1/2}$	3.07	0.90
294.4 Ga(I)	$4^2P_{3/2}$–$4^2D_{3/2, 5/2}$	4.31	0.30
286.8 Gd(I)+	–	8.26	0.30
287.4 Ga(I)	$4^2P_{1/2}$–$4^2D_{3/2}$	4.31	
262.5 Ga(I)	–	4.82	0.10
	$CdGa_2S_4$		
532.1 S(II)	$4s'^2D_{1/2}$–$4p'^2F^0_{7/2}$	17.40	1.00

This character of the emission intensity distribution in the spectra of laser plasmas generated in cadmium thiogallates indicates that $CdGa_2S_4$ crystals are more stable as compared to the analogous selenium compounds, which agrees with the conclusion based on the mass spectrometric data. Indeed, the content of S^+ and Se^+ ions in the mass spectra of the corresponding laser plasmas was also maximum (38 and 46%, respectively) [7]. Doubly charged selenium ions were not found in the mass spectra, but weak spectral lines of Se(III) were detected in the emission spectra of the laser plasma ($\lambda = 357.0$ nm). The high content of excited sulfur and selenium ions in the products of laser erosion is indicative of a considerable activity of the laser-induced plasma jet, which is a factor favoring the formation of high-quality films with high adhesion to substrates. The emission lines of Ga(I), Se(II), Se(III), and S(II) are of interest from the standpoint of diagnostics of the laser plasmas of cadmium thiogallates (T_e, n_e, metastable level populations, densities of atomic species in the ground state, etc.) by methods of nonstationary emission and absorption spectroscopy.

The most probable mechanism of the formation of excited sulfur and selenium ions is that involving a combination of the recombination processes in the expanding plasma, which was previously proposed in [7]. Taking into account a high relative content of these ions and their large velocities and internal energies, we may suggest that these very ions determine the initial stages of formation of laser-deposited cadmium thiogallate films.

Thus, the results of our investigation of the laser plasmas of cadmium thiogallates show that sulfur-containing crystals are more stable than their selenium-containing counterparts with respect to erosion by the YAG:Nd^{3+} laser radiation. The main excited component in the plasma, which are most pronounced in the emission spectra, are Se(II), Se(III), and S(II) ions despite their having greater ionization energies as compared to these of Cd(I) and Cd(II). The observed emission characteristics are of interest from the standpoint of the plasma diagnostics and optimization of the technology of laser sputter deposition of thin cadmium thiogallate films.

REFERENCES

1. A. N. Georgibiani, S. I. Radautsan, and I. M. Tiginyanu, Fiz. Tekh. Poluprovodn. (Leningrad) **19** (2), 193 (1985) [Sov. Phys. Semicond. **19**, 121 (1985)].
2. V. V. Badikov, I. N. Matveev, S. M. Pshenichnikov, *et al.*, Kvantovaya Élektron. (Moscow) **8** (4), 910 (1981).
3. B. F. Levine, O. G. Bethea, and H. M. Kaspev, IEEE J. Quantum Electron. **10** (12), 904 (1974).

4. V. S. Donu and E. F. Zhitar', in *Physics of Layered Semiconductor Compounds (A Collection of Scientific Papers)* (Kishinev, 1979), pp. 102–104.
5. V. P. Mushinskiĭ, B. B. Pokatilov, and B. I. Rapoport, in *Future Development of Optoelectronics* (Sov. Radio, Moscow, 1977).
6. I. É. Kacher, *Kinetics of the Evaporation and Condensation of Cadmium Thio and Selenogallate Films*, Available from Ukr. NIINTI No. 149-88 (Kiev, 1988).
7. I. É. Kacher, I. I. Opachko, and M. Yu. Rigan, Ukr. Fiz. Zh. **34** (11), 1728 (1989).
8. A. K. Shuaibov, L. L. Shimon, I. V. Shevera, and A. J. Minja, J. Phys. Stud. **3** (2), 157 (1999).
9. M. A. El'yashevich, in *Atomic and Molecular Spectroscopy* (Moscow, 1962).
10. A. N. Zaĭdel', V. K. Prokof'ev, S. M. Raĭskiĭ, *et al.*, *Tables of Spectral Lines* (Nauka, Moscow, 1969; Plenum, New York, 1970).
11. A. P. Striganov and G. A. Odintsova, in *Tables of Spectral Lines of Atoms and Ions: A Reference Book* (Moscow, 1982).
12. L. L. Shimon, É. I. Nepiĭpov, V. L. Goldovskiĭ, and N. V. Golovchak, Ukr. Fiz. Zh. **20** (2), 232 (1975).

Translated by P. Pozdeev

Technical Physics Letters, Vol. 26, No. 12, 2000, pp. 1061–1064. Translated from Pis'ma v Zhurnal Tekhnicheskoĭ Fiziki, Vol. 26, No. 23, 2000, pp. 71–78.

Effects of the Nonlocal Electron Distribution in a Plasma Display Cell

V. V. Ivanov, Yu. A. Mankelevich, O. V. Proshina, and T. V. Rakhimova

Research Institute of Nuclear Physics, Moscow State University, Moscow, Russia

Received February 2, 2000

Abstract—A self-consistent hybrid model of discharge in a plasma display cell is proposed, which provides an adequate description of a nonlocal electron distribution in nonstationary cases. A comparative analysis of the results of calculations based on the hybrid (nonlocal) and local models reveals considerable differences both in the discharge structure and in the emission dynamics. © *2000 MAIK "Nauka/Interperiodica".*

A considerable interest of researchers in studying the alternating current discharge in a plasma display panel (PDP) cell is explained by both practical and fundamental reasons. On the one hand, knowledge of the complex electrodynamic and plasmachemical processes in PDP cells is necessary for developing new PDP-based control electronic devices with improved image quality and brightness. On the other hand, the PDP cell operation involves fundamental gas-discharge processes such as the electric breakdown, the formation and decay of the cathode and quasineutral plasma layers, and the charge transfer from plasma to dielectric surfaces.

An important feature of these systems is that, because of a small size of the PDP cells (~100 μm), the nonlocal and nonstationary character of the electron energy distribution function determines to a considerable extent the discharge electrodynamics and plasma kinetics [1, 2]. As a result, the traditional approaches used to model the stationary high-frequency and dc discharges may no longer be applicable to modeling the PDP cell discharge.

Below, we present a hybrid one-dimensional model for description of the alternating discharge in a PDP cell. An important difference of this PDP cell from cells in a collective user display (CUD) modeled in our previous study [3] consists in a much smaller interelectrode gap ($d \sim 100$ μm) in the present system.

For a typical operating voltage, the absolute value of the electric field strength in the cathode layer may be on the order of 10^{-14} V/cm^2 at a layer thickness of 10 μm. The electron energy relaxation distance in this region is comparable with a characteristic range of the electric field strength variation. As a result, a flux of high-energy electrons is generated at the cathode layer boundary, which pass without energy losses through the cathode layer and possess an anisotropic energy distribution. The ionization ability of these electrons at a given point in the space is not characterized by the electric field strength at this point. Therefore, neither the local field approximation not the mean electron energy approximation (used in the CUD model [3] to account for the nonlocal electron energy distribution function) can be used to describe ionization processes in the plasma.

In the proposed hybrid model, all electrons are conventionally divided into two groups, slow and fast, and the motion of fast electrons is described b solving a nonstationary inhomogeneous Boltzmann equation by the particle-in-cell Monte-Carlo (PICMC) method [4] that takes into account the nonlocal character of the electron energy distribution function. The transport of slow electrons, ions, and neutral particles is described in the diffusion–drift approximation analogous to that employed in [3]. The system of continuity equations for all components is closed by adding the Poisson equation describing the electric field

$$\begin{aligned} dE/dz &= 4\pi e(n_\mathrm{i} - n_{\mathrm{e(slow)}} - n_{\mathrm{e(fast)}}) \\ \int_0^d E\,dz &= -V_\mathrm{g}(t) \end{aligned} \qquad (1)$$

and an equation describing the external electric circuit

$$V_\mathrm{g}(t) = V_\mathrm{s} + V_\mathrm{d}(t) = V_\mathrm{s} + \left(\int_0^t j^*(t)\,dt\right)/C_\mathrm{d}. \qquad (2)$$

Here, n_i, $n_{\mathrm{e(slow)}}$, and $n_{\mathrm{e(fast)}}$ are the concentrations of positive ions and the slow and fast electrons, respectively; $V_\mathrm{g}(t)$ is the total voltage drop across the interelectrode gap; d is the gap width; V_s is the applied voltage; $V_\mathrm{d}(t)$ is the additional voltage due to the electric field of charges accumulated in dielectric layers; $C_\mathrm{d} = 230$ pF/cm^2 is the equivalent capacity per unit area of the dielectric layers; and $j^*(t) = (\int_0^d j(z, t)dz)/d$ is the mean electric current density.

1063-7850/00/2612-1061$20.00

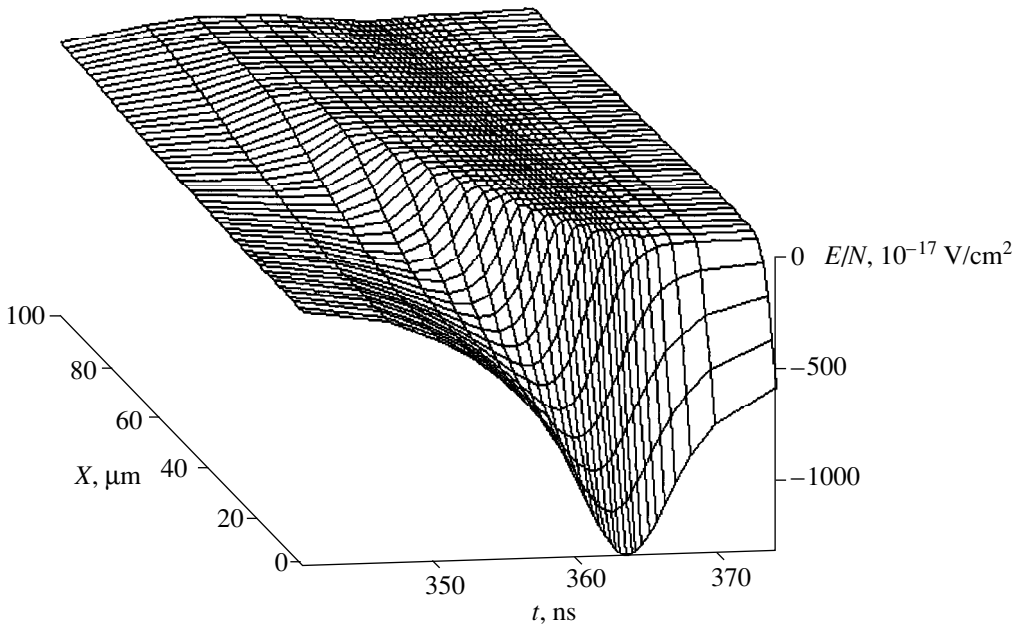

Fig. 1. The space–time evolution of electric field in the discharge calculated within the framework of the nonlocal model by the particle-in-cell Monte-Carlo method for a 90% Ne + 10% Xe gas mixture at a pressure of 560 Torr.

The PICMC calculations according to the model system of equations were performed for a 90% Ne + 10% Xe gas mixture at a total pressure of 560 Torr. In this work, we have used a periodic pulsed voltage with a frequency of 100 kHz with a rectangular pulse shape: $V_s = 273.5$ V during the first half-period and $V_s = 0$ during the second half-period. The calculation procedure was conducted until reaching a stationary regime, which was usually attained within 4–5 periods.

The transition of an electron from fast to slow group took place provided two conditions were satisfied:

$$|E(z)| < E_{tr}, \quad \varepsilon < \varepsilon_{tr}, \tag{3}$$

where $E(z)$ is the electric field strength at a point where the electron occurred and ε is the electron energy. The critical (transition) field strength E_{tr} in the first inequality (3) is selected so as to provide that electrons occurring within the cathode layer (where the field strength has a greater absolute value and a sharp spatial gradient) would be describes as belonging to the fast group. However, a weak-field region behind the cathode layer features the beam of high-energy electrons with anisotropic energy distribution function, which have to be also described by the PICMC method. For this reason, the second inequality in (3) introduces an energy threshold ε_{tr} for transition to the slow group. The ε_{tr} value is selected below the first inelastic threshold level.

Figure 1 shows a pattern of the space–time evolution of the electric field according to the nonlocal model proposed. As seen from this pattern, the field strength remains virtually constant in space for the time interval below 340 ns. The ion density increases with time to reach a level of 10^{12} cm^{-3}, which disturbs the initial electric field strength distribution and leads to the formation of a quasineutral plasma region near the anode. This region expands toward the cathode, with the plasma density and the discharge current density growing simultaneously.

A maximum discharge current density is attained at the time instant $t = 361$ ns. By that time, the electric field is clearly separated into two regions: a cathode layer (with a thickness of about 13 μm and a maximum field strength of 1.5×10^{-14} V/cm^2) and a quasineutral plasma region where the electric field strength is small as compared to that in the cathode layer. Note that, by this time instant, the voltage drop across the discharge gap has decreased to half of the initial level as a result of charging of the dielectric layers.

A comparison of the results of calculations according to the nonlocal and local models reveals two significant distinctions. First, the time of the cathode layer formation in the nonlocal model is ~360 ns, which exceeds the analogous value for the nonlocal model by a factor of 1.64. Second, the cathode layer width in the nonlocal model is about 2.5 times that in the local case (13 against 5 μm, respectively).

The nonlocal character of the electron energy distribution function is most clearly manifested by changes in the cathode layer structure. The electron density reaches approximately the same level in both models, but at different distances from the cathode: 5 and 13 μm for the local and nonlocal models, respectively. The nonlocal character of the electron energy distribution function near the cathode results in a markedly reduced ionization rate in this region. Indeed, electrons acquire

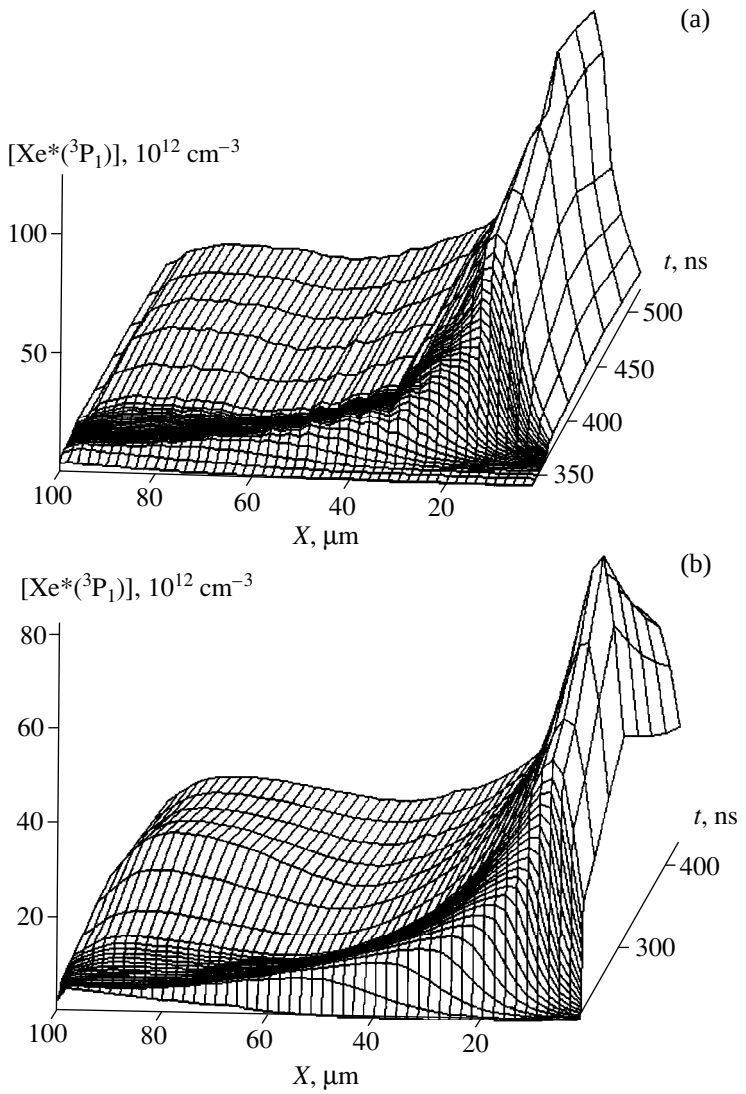

Fig. 2. The space–time evolution of the density of the radiative states Xe*($^3P_1$) of atomic xenon calculated by the particle-in-cell Monte-Carlo method according to the (a) nonlocal and (b) local models.

a considerable energy upon traveling in a strong near-cathode field. According to the local model, this energy is spent completely to produce ionization of the gas molecules immediately at the site where a given electron acquired this energy. In contrast, according to the nonlocal model this energy is spent mostly in the region of a weak field behind the cathode potential drop layer. This difference is just what accounts for a considerable shift in position of the electron density maximum. The fast electrons penetrating into the weak-field region provide for a significant level of gas ionization and excitation in this region, which results in the appearance of maxima in the density of states of atomic xenon [Xe*($^3P_1$) and Xe*($^3P_2$)] and xenon dimers [Xe_2^* ($^3\Sigma_n^+$)] at a considerable distance from the cathode.

Figures 2a and 2b show typical patterns of the space–time evolution of the density of the radiative states Xe*($^3P_1$) of atomic xenon calculated according to the nonlocal and local models, which clearly reveal a difference between the cathode layer structures in the two cases. In the nonlocal case, a maximum in the density of the radiative state is higher and is reached at a much greater distance from cathode than in the local model. In the region of a quasineutral plasma, the densities of radiative states in the two models are close to each other.

The observed distinctions can be interpreted by considering the energy balance of the discharge. First, note that an energy ($\sim 9 \times 10^{-6}$ J/cm^2) transferred to the electron component of the plasma accounts for 44 and 37% fraction of the total discharge energy in the local and nonlocal cases, respectively. It must be also noted that this difference does not imply a decrease in the plasma emission power in the nonlocal case. The electron energy component is only markedly redistributed,

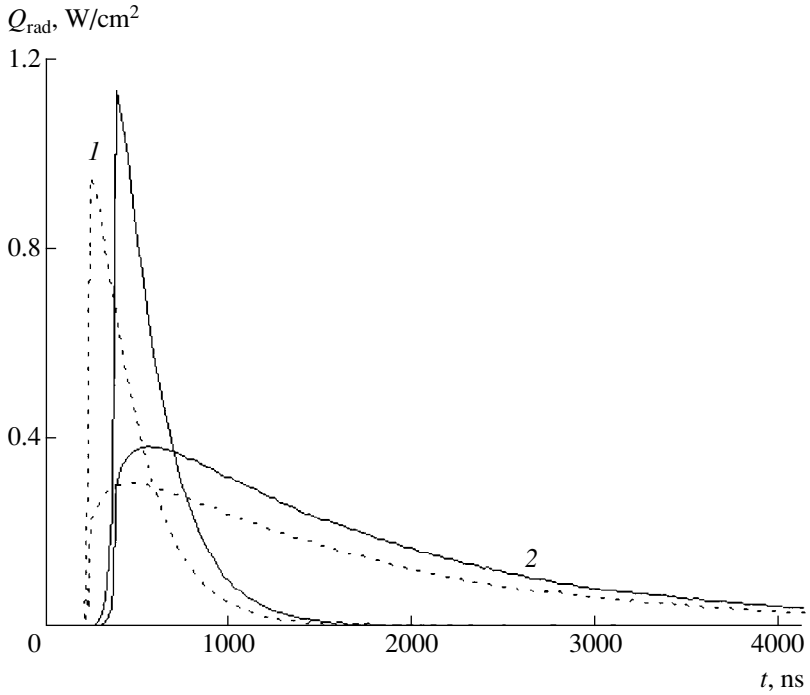

Fig. 3. Time variation of the radiant energy density Q_{rad} emitted from discharge in the (*1*) resonance (147 nm) and (*2*) dimer (173 nm) lines. Solid and dashed curves are calculated according to the nonlocal and local models, respectively.

whereby a greater proportion of this energy in the near-cathode region is spent for excitation of the radiative states and a smaller part, for ionization. In the weak-field region of the positive plasma column, the nonlocal and anisotropic effects are virtually not manifested and hence, the concentrations of excited states calculated by the two models are close to one another.

An increase in the emission yield observed in the nonlocal case is due to a higher proportion of energy transferred to the excited states of xenon. The influence of this factor on the total emission from discharge is illustrated in Fig. 3 showing dynamics of the space-integrated emission from plasma in the resonance and dimer lines calculated by the two models. The pattern for the nonlocal case exhibits, besides a time shift of the emission onset, a considerable increase in the emission intensity.

Acknowledgments. The work was supported by the Russian Foundation for Basic Research, project nos. 96-15-96447 and 98-02-16381.

REFERENCES

1. V. V. Ivanov, K. S. Klopovsky, Y. A. Mankelevich, *et al.*, in *Proceedings of the 23rd International Conference on the Phenomena in Ionized Gases (ICPIG), Toulose, France, 1997*, Ed. by M. C. Bordge and A. Gleizes (EDP Sciences, Les Ullis, 1997), Vol. 2, p. 234.
2. J. P. Boeuf, C. Punset, A. Hirech, and H. Doyeux, in *Proceedings of the 23rd International Conference on the Phenomena in Ionized Gases (ICPIG), Toulose, France, 1997*, Ed. by M. C. Bordge and A. Gleizes (EDP Sciences, Les Ullis, 1997), Vol. 7, p. C4.
3. V. V. Ivanov, Yu. A. Mankelevich, O. V. Proshina, *et al.*, Fiz. Plazmy **25** (7), 646 (1999) [Plasma Phys. Rep. **25**, 591 (1999)].
4. R. Hockney and J. Eastwood, *Computer Simulation Using Particles* (McGraw-Hill, New York, 1984; Mir, Moscow, 1987).

Translated by P. Pozdeev

Technical Physics Letters, Vol. 26, No. 12, 2000, pp. 1065–1066. Translated from Pis'ma v Zhurnal Tekhnicheskoĭ Fiziki, Vol. 26, No. 23, 2000, pp. 79–83.

Modeling of the Microlens Fabrication in Glasses by Field-Assisted Ion Exchange: The Space Charge Effects

V. A. Nikitin, A. V. Shevchenko, and N. A. Yakovenko

Kuban State University, Krasnodar, Russia;
e-mail: savmail@usa.net

Received July 12, 2000

Abstract—Effects of the space charge on the microlens formation in glasses using the electric-field-assisted ion exchange process have been analyzed by numerical methods. It is shown that the electric field strength in the substrate is inhomogeneously distributed and decreases with time. Since the field-assisted migration velocity depends on the field strength, these factors slow down the ion exchange rate and decrease the microlens diameter below the values calculated assuming a homogeneous field strength distribution in the substrate. © *2000 MAIK "Nauka/Interperiodica".*

Microlenses formed by ion exchange in glasses are widely used in various optoelectronic devices for the collimating focusing of light and for the coupling of optical channels [1–2]. A well-known technology for the fabrication of microlens structures is the electric-field-assisted ion exchange (FAIE) [1, 3, 4]. Various optical elements fabricated by the FAIE technology are frequently modeled with neglect of the possible effects of a space charge appearing as a result of the different mobilities of ions involved in the exchange [5]. Below, we will demonstrate that the presence of this space charge in a glass substrate may result in a considerable decrease in the rate of ion exchange in microlenses with a diameter of the order of several hundreds of microns, which must be taken into account for correctly modeling the corresponding technological process.

Let us consider the planar waveguide formation on a glass substrate using the FAIE process in a melt of an alkali metal (Me^+) nitrate (Fig. 1). In the course of the waveguide layer formation, sodium ions (Na^+) in the glass substrate are replaced by Me^+ ions from the nitrate melt. A refractive index profile formed in this system in the presence of an external electric field exhibits a stepwise shape. Let us divide the substrate into two parts, the waveguide and nonwaveguide. Since the chemical compositions of these layers are different, they will generally possess different resistivities. Below, d denotes the waveguide layer thickness and h, the thickness of the remaining (nonwaveguide) part of the substrate. Let v denote the part of the total constant voltage U applied to the substrate during the FAIE process, which drops across the waveguide layer.

Since the current densities in the two parts of the substrate are equal, while their resistivities are different, the waveguide–glass interface must feature a sharp change in the electric field strength. This change cannot be explained by an inhomogeneity in the dielectric permittivity profile, because experimental data indicate that a difference in refractive indices between the waveguide and the initial glass is on the order of 10%, while the resistivity may change (according to the Nernst–Einstein relationship) by a factor of several tens to hundreds. Therefore, it is a space charge formed at the waveguide–glass interface that accounts for a change in the electric field strength.

Over a time interval δt, the waveguide layer thickness d will change as described by the following relationship:

$$\delta d = \mu E \delta t, \tag{1}$$

where δd is the increment of the planar waveguide thickness, μ is the mobility of alkali metal ions Me^+, and E is the electric field strength in the waveguide layer. Since the current density can be expressed as $j = U/(\rho_1 d + \rho_2 h)$ (ρ_1 and ρ_2 being the resistivities of the wave

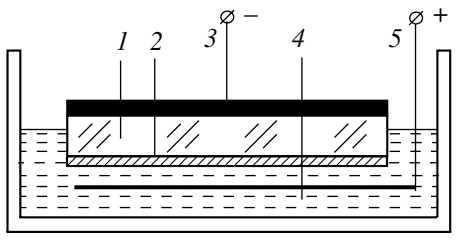

Fig. 1. Schematic diagram illustrating the process of planar waveguide formation by the field-assisted ion exchange method: (*1*) glass plate (substrate); (*2*) planar waveguide layer; (*3*) cathode; (*4*) melted alkali metal salt; (*5*) anode.

1063-7850/00/2612-1065$20.00 © 2000 MAIK "Nauka/Interperiodica"

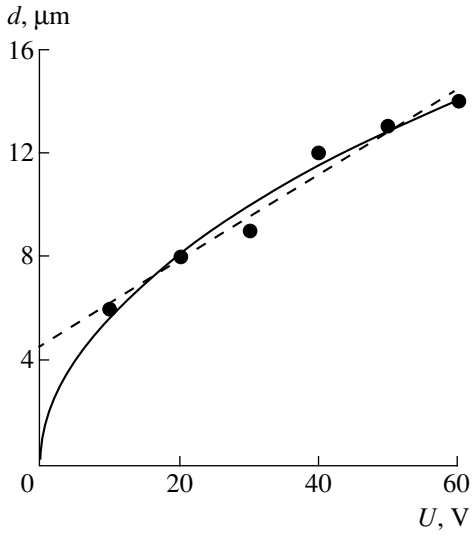

Fig. 2. Dependence of the planar waveguide thickness d on the applied voltage U: black circles show the experimental data, dashed line is the linear approximation, and solid curve is the approximation by formula (4).

guide layer and the initial glass, respectively), the voltage drop across the waveguide is given by the formula

$$v = \frac{Ud}{d + (\rho_2/\rho_1)h}. \quad (2)$$

Using formulas (1) and (2), we obtain

$$\delta t = \frac{d + (\rho_2/\rho_1)h}{\mu U}\delta d. \quad (3)$$

Upon integrating this relationship and solving the resulting square equation, we arrive at the formula

$$d = [(h\rho_2/\rho_1)^2 + 2\mu U t]^{0.5} - h\rho_2/\rho_1. \quad (4)$$

As seen from this formula, the waveguide thickness is a nonlinear function of the time and the applied voltage.

Figure 2 shows experimental data on the dependence of the planar wave guide thickness on the applied voltage measured in a glass substrate in the course of FAIE with an $AgNO_3$ melt. For comparison, these experimental data were approximated by least squares with a linear function and with a curve according to formula (4). According to the traditional approach assuming a homogeneous field distribution in the substrate, the linear plot must pass through the origin (zero waveguide in the absence of applied voltage) because the refractive index profile has a stepwise shape. However, the approximated line intersects the ordinate axis considerably above zero. In contrast, formula (4) well describes the experimental data and tends to zero with decreasing applied voltage. The error of approximation in both cases was about 0.5 μm. Formula (4) also qualitatively agrees with the results reported in [5, 6].

According to formula (4), the electric field strength decreases with time. The thickness of microlenses may reach several hundreds of microns for a substrate thickness of the order of one millimeter. According to experimental data [7] for a FAIE process of substituting Ag^+ ions for Na^+ ions in a glass substrate, the $k = \rho_1/\rho_2$ ratio may acquire the values above 10. Assuming that d = 300 μm, h = 1 mm, and k = 10, we may conclude that the field strength would differ from the initial value by a factor of 4. According to formula (1), this change would markedly slow the ion exchange rate.

For $v \gg U - v$, formula (4) simplifies to

$$d = (2\mu U t)^{1/2}. \quad (5)$$

For a microlens diameter ten times greater than a hole diameter in the metal mask, we may approximately consider the field as spherically symmetric. Then, for a constant electric field strength, the microlens radius is proportional to $t^{1/3}$, where t is the microlens formation (exchange) time [8]. However, taking into account that the field strength decreases with time, we may conclude from formula (5) that the lens radius is approximately proportional to $t^{1/6}$. Indeed, according to the experimental data [8], the effective field strength is about one-tenth of the value applied. This difference is well explained by the presence of the space charge leading to a decrease in the field strength with time.

Thus, we have demonstrated that modeling of the microlens fabrication by the field-assisted ion exchange method must take into account the space charge effects, which markedly slow the ion exchange rate.

REFERENCES

1. K. Iga and S. Misava, Appl. Opt. **25** (19), 3388 (1986).
2. Asako Sasaki *et al.*, Jpn. J. Appl. Phys. **31** (5B), 1611 (1992).
3. V. N. Ivanov, V. A. Nikitin, E. P. Nikitina, and N. A. Yakovenko, Zh. Tekh. Fiz. **53** (10), 2088 (1984) [Sov. Phys. Tech. Phys. **28**, 1279 (1984)].
4. Gladkiĭ *et al.*, Kvantovaya Élektron. (Moscow) **22** (10), 1027 (1995).
5. B. Pantchev and Z. Nikolov, IEEE J. Quantum Electron. **29** (1), 154 (1993).
6. Dong Cheng *et al.*, Opt. Commun. **137** (5), 233 (1997).
7. R. V. Ramaswamy and R. Srivastava, J. Lightwave Technol. **6**, 984 (1988).
8. Masahio Oikawa *et al.*, Appl. Opt. **23** (11), 1787 (1984).

Translated by P. Pozdeev

Technical Physics Letters, Vol. 26, No. 12, 2000, pp. 1067–1069. Translated from Pis'ma v Zhurnal Tekhnicheskoĭ Fiziki, Vol. 26, No. 23, 2000, pp. 84–90.

Magnetooptical Interference Effects in a Structure Featuring a 2D Electron Gas

V. V. Popov and T. V. Teperik

Saratov Department, Institute of Radio Engineering and Electronics, Russian Academy of Sciences, Saratov, Russia;

e-mail: popov@ire.san.ru

Received June 30, 2000

Abstract—Magnetooptical effects in a system with a 2D electron gas are considered, which are related to the interference resonances appearing in a plane-parallel plate exposed to a weak magnetic field. A new method is proposed for contactless measurements of the Hall conductivity in a 2D electron system. © *2000 MAIK "Nauka/Interperiodica".*

As is known, the magnetooptical effects observed for an electromagnetic wave incident on a two-dimensional (2D) magnetically active electron system are usually rather weakly pronounced [1–3] because the region featuring the interaction between the incident wave and the magnetically active medium is small. However, the magnitude of this effect may rise considerably upon excitation of a cyclotron resonance in the 2D electron system [4–6]. Here, the resonance magnetic field strength has a fixed value and is typically rather large (up to 10 T) for real semiconductor structures.

The purpose of this study was to analyze theoretically the magnetooptical effects in a structure with a 2D electron gas related to the interference (dimensional) resonances of the electromagnetic wave in the structure. In such a system, the resonance value of the external magnetic field is not fixed and may be markedly lower than that in the case of a cyclotron resonance.

Similarly to the case considered previously [6],we will consider a linearly polarized wave with a wavelength λ normally incident onto a plane-parallel dielectric plate (substrate) of thickness d featuring a 2D electron layer at one of the plate surfaces. The substrate is exposed to an external magnetic field with the induction vector $\mathbf{B}_0$ oriented perpendicularly to the plane of the 2D electron system.

Let us introduce the following complex coefficients of the wave conversion:

$$r_{pp} = \frac{E_r^{(p)}}{E_i^{(p)}}, \quad r_{sp} = \frac{E_r^{(s)}}{E_i^{(p)}}, \quad t_{pp} = \frac{E_t^{(p)}}{E_i^{(p)}}, \quad t_{sp} = \frac{E_t^{(s)}}{E_i^{(p)}}, \quad (1)$$

where $E_i^{(p)}$ is the complex electric field amplitude of the incident wave; $E_r^{(p)}$ and $E_t^{(p)}$ are the complex electric field amplitudes of the reflected and transmitter waves, respectively, with a linear polarization coinciding with that of the incident wave; and $E_r^{(s)}$ and $E_t^{(s)}$ are the complex electric field amplitudes of the reflected and transmitter waves, respectively, with a linear polarization perpendicular to that of the incident wave.

We also introduce the complex coefficients of the wave power conversion in the form of the energy flux ratios:

$$R_{pp} = \frac{P_r^{(p)}}{P_i^{(p)}}, \quad R_{sp} = \frac{P_r^{(s)}}{P_i^{(p)}}, \quad T_{pp} = \frac{P_t^{(p)}}{P_i^{(p)}}, \quad T_{sp} = \frac{P_t^{(s)}}{P_i^{(p)}}. \quad (2)$$

Here, the subscripts and superscripts have the same meaning as those in expressions (1). Obviously, the quantities r_{sp}, t_{sp}, R_{sp}, and T_{sp} also have a meaning of the coefficients of conversion of the wave polarization.

The values of the electric field amplitudes and the energy fluxes for the transmitted and reflected waves are calculated by solving the Maxwell equations in the substrate and in the surrounding media (with the corresponding boundary conditions at interfaces) taking into account the response of the magnetically active 2D electron system. The dielectric constants of the surrounding media are taken equal to unity. The components of the conductivity tensor for the 2D electron system interacting with the magnetic field are determined by the expressions

$$\sigma_\perp = \sigma_0 \frac{1 - i\omega\tau}{(\omega_c\tau)^2 + (1 - i\omega\tau)^2},$$
$$\sigma_x = -\sigma_0 \frac{\omega_c\tau}{(\omega_c\tau)^2 + (1 - i\omega\tau)^2}, \quad (3)$$

where ω is the circular frequency of the wave; $\omega_c = |e|B_0/m^*$ is the cyclotron frequency; $\sigma_0 = e^2N_s\tau/m^*$ is the dc conductivity of the 2D electron system in the absence of external magnetic fields; e, m^*, N_s, and τ are the charge, effective mass, surface concentration, and

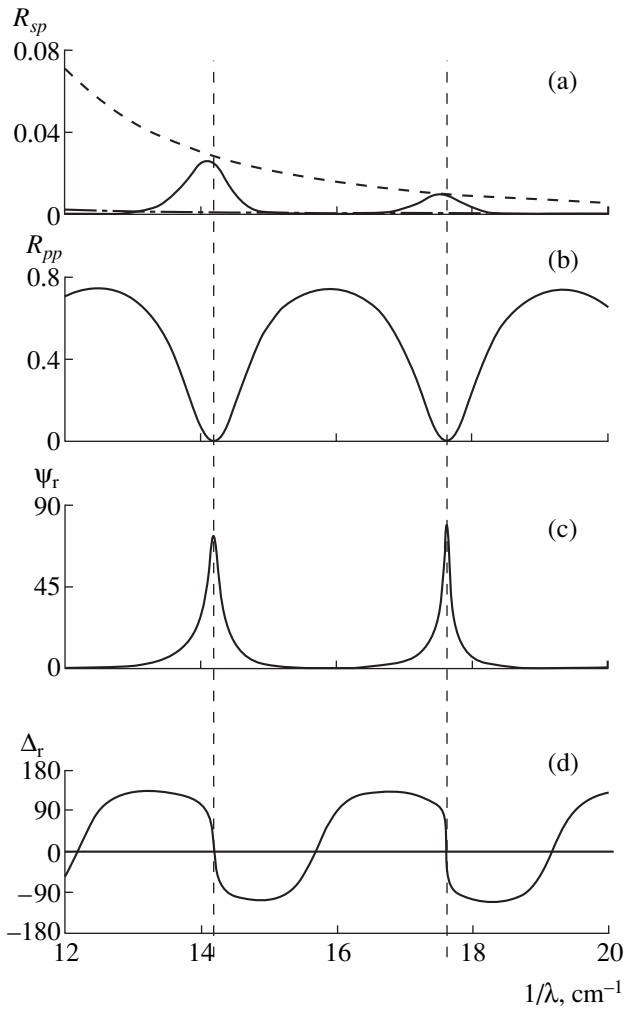

Fig. 1. The coefficients of conversion of the wave power and the polarization angles for the reflected wave calculated for $\varepsilon_s = 12.8$; $N_s = 10^{12}$ cm^{-2}; $d = 4 \times 10^{-2}$ cm; and $B_0 = 0.5$ T.

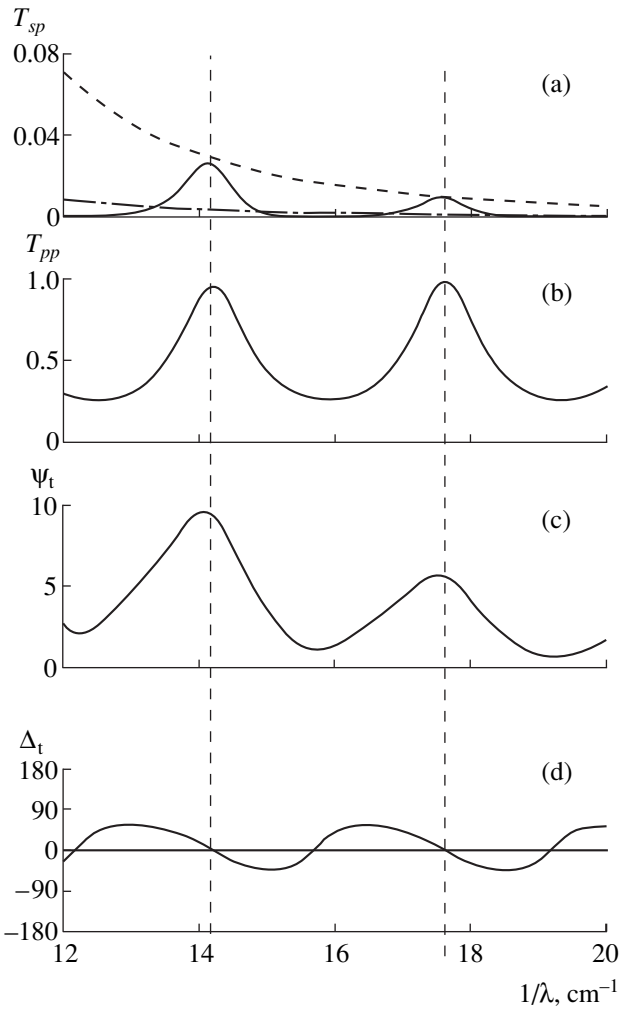

Fig. 2. The coefficients of conversion of the wave power and the polarization angles for the transmitted wave calculated for the same parameters as in Fig. 1.

phenomenological momentum relaxation time of electrons in the 2D system. The numerical calculations were performed using the parameters characteristic of a 2D electron gas in GaAs-based semiconductor structures.

The complex coefficient of wave conversion defined by expressions (7) were used to calculate the polarization angles ψ_r, ψ_t, Δ_r, and Δ_t defined by the well-known formulas:

$$\tan\psi_r = \left|\frac{r_{sp}}{r_{pp}}\right|, \quad \Delta_r = \arctan\frac{\mathrm{Im}(r_{sp}/r_{pp})}{\mathrm{Re}(r_{sp}/r_{pp})},$$

$$\tan\psi_t = \left|\frac{t_{sp}}{t_{pp}}\right|, \quad \Delta_t = \arctan\frac{\mathrm{Im}(t_{sp}/t_{pp})}{\mathrm{Re}(t_{sp}/t_{pp})}.$$

Figures 1 and 2 show the plots of the coefficients of conversion for the wave power and the polarization angles calculated for a weak magnetic field ($B_0 = 0.5$ T) with neglect of the electron scattering in the 2D system ($1/\tau = 0$) The maximum values of the conversion coefficients for the wave power and the polarization angles ψ_r and ψ_t are obtained for incident waves with the wavelengths corresponding to the case of a half-wave plate $\lambda_N = 2d\sqrt{\varepsilon_s}/N$, where ε_s is the dielectric constant of the substrate plate and N is a nonzero integer.

In the absence of a 2D electron layer, the substrate with a half- wave thickness is completely transparent for the incident electromagnetic wave ($R_{pp} = 0$, $T_{pp} = 1$). The presence of the 2D electron layer somewhat shifts the positions of minimum for the reflection coefficient ($R_{pp} \simeq 0$) and, accordingly, the positions of maximum for the transmission coefficient ($T_{pp} \simeq 1$); on the scale of Figs. 1 and 2, these small shifts and the deviations of R_{pp} and T_{pp} from zero and unity, respectively, are not manifested. For a substrate with the half-wave thickness, the minima in the reflection coefficient R_{pp} appear

as a result of addition of the *p*-polarized waves reflected in the counterphase from the front and rear substrate surfaces.

The phenomenon of polarization conversion in the system under consideration is related to the Hall currents induced by the external wave in the 2D electron system. The oscillating Hall current induces *s*-polarized electromagnetic waves in the structure. The interference between oscillations of the Hall current and the current induced in the 2D electron plasma by the *s*-polarized wave fields (excited by the Hall current in the flat dielectric substrate layer) results in variation of the intensity of the polarization conversion depending on the incident wavelength (or depending on the substrate plate thickness for a fixed wavelength). For a substrate with a half-wave thickness, the *s*-polarized wave reflected from the free surface induces a current in the 2D system plane, which oscillates in phase with the Hall current. The total current in the 2D system excites the *s*-polarized fields with still greater intensity and so on. As a result, the conversion intensity exhibits a tenfold increase as compared to the case when no reflection takes place at the free surface of the substrate. Note that, in practice, the latter situation most frequently takes place due to deviation of the substrate surfaces from the plane-parallel configuration (the corresponding curves of the conversion coefficients are depicted by dashed lines in Figs. 1a and 2a). In the opposite case of a quarter-wave plate, the polarization conversion process is virtually completely suppressed. Note that the phenomenon under consideration does not dependent on whether the 2D electron layer is situated at the front or rear plate surface.

In a substrate with a half-wave thickness, which is completely transparent to the incident electromagnetic wave, the process of polarization conversion proceeds exactly in the same manner as if the 2D electron system would occur in a homogeneous space with the dielectric permittivity $\varepsilon = 1$. In this case, we may readily estimate the efficiency of the polarization conversion. The Hall current $j^{(s)} = -\sigma_\times E_i^{(p)}$ (induced by the electric field $E_i^{(p)}$ of the incident electromagnetic wave) generates the magnetic fields $H_{r,t}^{(s)} = \pm 2\pi\sigma_\times E_i^{(p)}/c$ in the surrounding media. These magnetic fields, in turn, excite the electric vortex fields $E_{r,t}^{(s)} = \pm H_{r,t}^{(s)}$ (in the last two expressions, the superscripts and subscripts refer to the reflected and transmitted waves, respectively). As a result, the 2D electron layer generates the *s*-polarized electromagnetic waves. The energy fluxes of the reflected and transmitted *s*-polarized waves are determined by the following formulas:

$$P_{r,t}^{(s)} = \frac{c}{8\pi}\mathrm{Re}(\mathbf{E}_{r,t}^{(s)} \times \mathbf{H}_{r,t}^{(s)*}) = \frac{\pi}{2c}|\sigma_\times|^2 E_t^{(p)}.$$

Using these expressions, the conversion coefficients (2) can be written as

$$R_{sp} = T_{sp} = \left(\frac{2\pi}{c}\right)^2 |\sigma_\times|^2. \quad (4)$$

The curves determined by expressions (4) are depicted by dashed lines in Figs. 1a and 2a. The results of rigorous calculations coincide with the values given by formula (4) at sufficiently high frequencies $2\pi c/\lambda > (2–3)\omega_c$.

It should be noted that formula (4) is also valid in the presence of electron scattering in the 2D system. This fact may serve a base for a simple method of contactless measurements of the Hall conductivity at high frequencies ($\omega > \omega_c$) in real structures. As the frequency is reduced, the accuracy of formula (4) obtained in the approximation of preset current $j^{(s)}$ decreases. In the general case, the current density $j^{(s)}$ has to be calculated within the framework of the self-consistent approach using the formula $j^{(s)} = -\sigma_\times E_i^{(p)} + \sigma_\perp E_r^{(s)}$.

In the general case, the reflected and transmitted waves are elliptically polarized (Figs. 1c, 1d, 2c, and 2d). In the substrate with half-wave thickness, the polarization of the reflected wave is virtually completely transformed, whereby the polarization plane of this wave is rotated by 90° relative to that of the incident wave (Figs. 1c and 1d).

Acknowledgments. The work was supported by the Federal Target Program "Integration 1997–2000" (project no. 696.3) and the Russian Foundation for Basic Research (project no. 00-02-16440).

REFERENCES

1. R. F. O'Connell and G. Wallace, Phys. Rev. B **26**, 2231 (1982).
2. V. A. Volkov and S. A. Mikhaĭlov, Pis'ma Zh. Éksp. Teor. Fiz. **41**, 389 (1985) [JETP Lett. **41**, 476 (1985)].
3. V. A. Volkov, D. V. Galchenkov, L. A. Galchenkov, *et al.*, Pis'ma Zh. Éksp. Teor. Fiz. **43**, 255 (1986) [JETP Lett. **43**, 326 (1986)].
4. V. V. Popov and T. V. Teperik, Pis'ma Zh. Tekh. Fiz. **25** (21), 21 (1999) [Tech. Phys. Lett. **25**, 855 (1999)].
5. V. V. Popov and T. V. Teperik, Pis'ma Zh. Éksp. Teor. Fiz. **70** (4), 247 (1999) [JETP Lett. **70**, 254 (1999)].
6. V. V. Popov and T. V. Teperik, Pis'ma Zh. Tekh. Fiz. **26** (18), 17 (2000) [Tech. Phys. Lett. **26**, 814 (2000)].
7. R. M. Azzam and N. M. Bashara, *Ellipsometry and Polarized Light* (North-Holland, Amsterdam, 1977; Mir, Moscow, 1981).

Translated by P. Pozdeev

Technical Physics Letters, Vol. 26, No. 12, 2000, pp. 1070–1071. Translated from Pis'ma v Zhurnal Tekhnicheskoĭ Fiziki, Vol. 26, No. 23, 2000, pp. 91–94.

The Optical Absorption of Solid Fractal Structures in Silicon Carbide

I. V. Zolotukhin, S. A. Gribanov, and A. A. Popov

Voronezh State Technical University, Voronezh, Russia;

e-mail: kalinin@nsl.vstu.ac.ru

Received June 12, 2000

Abstract—The silicon carbide particles with solid fractal formed in an electric arc discharge plasma exhibit anomalous optical properties. In the 360–475 nm wavelength range, the level of light absorption in the fractal structures of silicon carbide is 15–30 times that in single-crystalline SiC samples. © *2000 MAIK "Nauka/Interperiodica".*

Solid fractal structures formed as a result of the cluster self-organization processes in open dissipative systems represent essentially a new type of substance in the condensed state. As is known, a fractal structure can only be formed under certain physical conditions. Unfortunately, the conditions required for the formation of such structures in particular substances and the physical properties of the resulting systems are still insufficiently studied and cannot be described within the framework of the existing theories. Recently, [1] we synthesized the fractal structures in carbon by spraying graphite in an electric arc plasma. It was naturally suggested that this method can be employed to obtain fractal structures in other substances as well.

The available (albeit still insufficient) experimental data indicate that the fractal structures may possess unique physical properties. In particular, the fractal structures of some porous materials are characterized by highly developed internal surface (with a specific area of 500 m^2/g and above). The secondary emission current generated in porous dielectrics with a fractal structure bombarded with an electron beam may exceed the primary beam current by three orders of magnitude [2].

We obtained the samples of silicon carbide (SiC) by spraying a mechanical mixture of silicon and carbon (graphite) in the plasma of an electric arc discharge generated at a current density of 1000–1200 A/cm^2 and a voltage of 15–25 V. The SiC particles with a solid fractal structure were obtained in the form of a ring-shaped deposit on a graphite cathode-substrate. The X-ray diffraction analysis showed evidence of a finely dispersed structure of the deposit.

The surface morphology of the deposit was studied in a scanning electron microscope (SEM) of the REM-300 type (Russia). The particle surface (Fig. 1a) exhibited columnar formations with a diameter of 5–20 μm. The columns are composed of spheroidal globules with the average diameter of 0.8–3.0 μm (Fig. 1b) consisting, in turn, of the smaller spheroidal particles sized 0.30–0.45 μm. The latter particles consist of spherical clusters with a still smaller size of 0.03–0.05 μm.

Analysis of the sample structure with the aid of a scanning tunneling microscope showed the latter clusters to be composed of small rounded and elongated clusters 1–5 nm in size. Thus, the deposit exhibits a

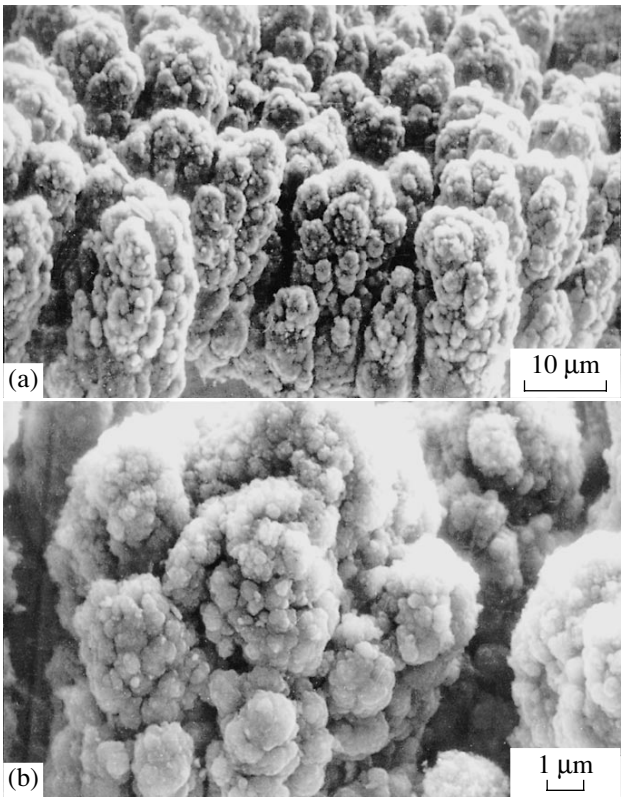

Fig. 1. SEM micrographs showing (a) columnar and (b) spheroidal structure of the surface of SiC particles deposited from an arc discharge plasma.

1063-7850/00/2612-1070$20.00

dimensional and structural hierarchy, which is a characteristic feature of the fractal structures. The deposit had a highly porous structure with extremely developed internal surface (as evidenced by the density amounting to 50–60% of the value for bulk silicon carbide).

The optical absorption of the silicon carbide samples with the fractal and single-crystalline surfaces was studied with an SDL-2 instrument operated in the 360–600 nm wavelength range. Figure 2 shows a plot of the ratio k_1/k_2 of the absorption coefficients of the fractal and single-crystalline SiC, respectively, versus the incident light wavelength. In the wavelength interval from 360 to 475 nm (i.e., for the photon energies exceeding the forbidden band width in SiC), the fractal structures in SiC absorb the electromagnetic waves 15–30 times stronger than does the single-crystalline SiC. In the 475–550 nm interval the optical absorption of SiC fractal structures gradually decreases to reach (at 550–600 nm) a level only 2–3 times that characteristic of the single-crystalline silicon carbide.

The experimental data described above agree with the existing notions about the optical absorption properties of fractal aggregates composed of metal clusters [3]. Indeed, the absorption coefficient of a fractal structure consisting of randomly arranged fractal aggregates independently interacting with the incident electromagnetic waves is described by the formula

$$k = k_0(R/r)^{3-D}, \quad (1)$$

where k_0 is the absorption coefficient of a SiC cluster with the radius r, R is the radius of the fractal aggregate, and D is the fractal dimensionality. The surface fractal dimensionality in our structures was evaluated at 1.73 ± 0.05 and the R/r ratio was abut 10. Substituting these values into formula (1), we obtain $k/k_0 \sim 18$–19, which coincides in the order of magnitude with our experimental data.

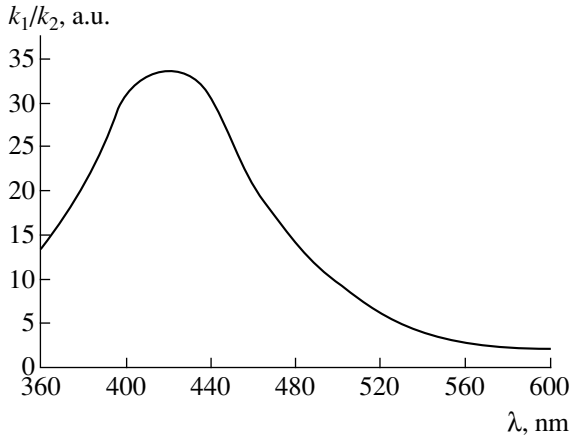

Fig. 2. The plot of k_1/k_2 versus light wavelength in the 360–600 nm spectral range (see the text for explanation).

Thus, the SiC particles with a fractal structure studied represent a nonlinear medium that can be used in absorption elements for the visible spectral range.

REFERENCES

1. I. V. Zolotukhin and Yu. V. Sokolov, Pis'ma Zh. Tekh. Fiz. **23** (13), 71 (1997) [Tech. Phys. Lett. **23**, 525 (1997)].
2. M. P. Lorikyan, Usp. Fiz. Nauk **165** (11), 1323 (1995) [Phys. Usp. **38**, 1271 (1995)].
3. B. M. Smirnov, Usp. Fiz. Nauk **167** (11), 1169 (1997) [Phys. Usp. **40**, 1117 (1997)].

Translated by P. Pozdeev

Technical Physics Letters, Vol. 26, No. 12, 2000, pp. 1072–1074. Translated from Pis'ma v Zhurnal Tekhnicheskoĭ Fiziki, Vol. 26, No. 24, 2000, pp. 1–6.

Effect of the Niobium Pentoxide Powder Dispersity on the Mechanical Properties of Niobate Ferroelectric Ceramics

M. I. Kovalenko, L. A. Reznichenko, O. N. Razumovskaya, and S. O. Kramarov

Institute of Physics, Rostov State University, Rostov-on-Don, Russia;
Rostov State Pedagogical University, Rostov-on-Don, Russia;
e-mail: mary@tdu.donpac.ru
Received April 11, 2000

Abstract—Dispersity of the initial niobium pentoxide powder used in the synthesis of niobate ceramics significantly affects the mechanical properties of these ferroelectric materials. The best mechanical properties were observed in the samples of niobate ceramics characterized by a minimum deformation of the unit cells, corresponding to certain intervals of the specific surface of the initial niobium pentoxide powder. These results must be taken into account in the research, synthesis, and development of niobate ferroelectric ceramics for various applications. © *2000 MAIK "Nauka/Interperiodica".*

Previously [1–3], we established that the mechanical properties of ferroelectric ceramics based on alkali metal niobates (niobate ferroelectric ceramics, NFCs) are significantly affected by crystallochemical properties of their A-cations, the thermodynamic prehistory of a particular material, and the character of the grain structure formed in the course of the heat treatment.

It was established that there are different mechanisms responsible for the self-fracturing of NFCs based on lithium niobate [1] and sodium niobate [2]. In the former case, the fracture is caused by internal mechanical (thermoelastic) stresses acting upon the crystal grains, which are developed as a result of their anisotropic deformation. Here, the cracks propagate predominantly along the intergrain boundaries. In the latter case, the disorder results from the combined action of mechanical stresses of various origin. The internal mechanical stresses determine the formation of cracks of the Griffith type as a result of self-fracturing of the coarsest grains or their aggregates (clusters). The macroscopic stresses, arising as a result of the inhomogeneous composition and temperature gradients developed during rapid cooling of the samples, control propagation of the initial cracks. In this case, the samples exhibit disintegration into rather large, sufficiently strong fragments.

Thus, it was concluded that the mechanical properties of NFCs depend to a considerable extent on the technological regimes and processes involved in their structure formation. In particular, we established an optimum temperature interval for the sintering of NFCs. Going beyond this range toward the higher sintering temperature T_1 causes the development of secondary intermittent recrystallization processes, which is accompanied by the rapid grain growth up to the critical size and by the crack formation.

Another important factor that may also affect the mechanical properties of NFCs is the physicochemical state of their main initial component—niobium pentoxide (Nb_2O_5)—in particular, the granulometric composition (not rated by the existing normative technological documentation). This possibility was indicated by our experimental results revealing a strong effect of the dispersity of the initial Nb_2O_5 powder on the structure, microstructure characteristics, and electrical properties of the final NFCs [4–6]. We have studied the Nb_2O_5 powders of various grades and established the possible intervals of variation of the specific surface S of the initial material, which ensured the obtaining of final NFCs possessing optimum properties.

The purpose of this study was to follow variations in the mechanical properties of NFCs depending on the S value of the initial Nb_2O_5 powder.

The experiments were performed with a PKR-35 material developed by us based on solid solutions of the $(Na,Li)NbO_3$ system [7]. The NFC samples were synthesized using various Nb_2O_5 powders: the commercial NBO-PT grade with S = 449–745 m^2/kg from the Pyshma ceramics plant (V. Pyshma, Urals region), a commercial special purity grade with S = 210–1040 m^2/kg from the Krasnyĭ Khimik plant (St. Petersburg), and a Nb_2O_5 powder (of a special purity type) with S = 1852–5770 m^2/kg prepared by a heterophase method at the Mendeleev University of Chemical Technology (Moscow). The mechanical properties were characterized by the ultimate tensile strength σ, measured using a coaxial bending test, and by a fracture viscosity

1063-7850/00/2612-1072$20.00

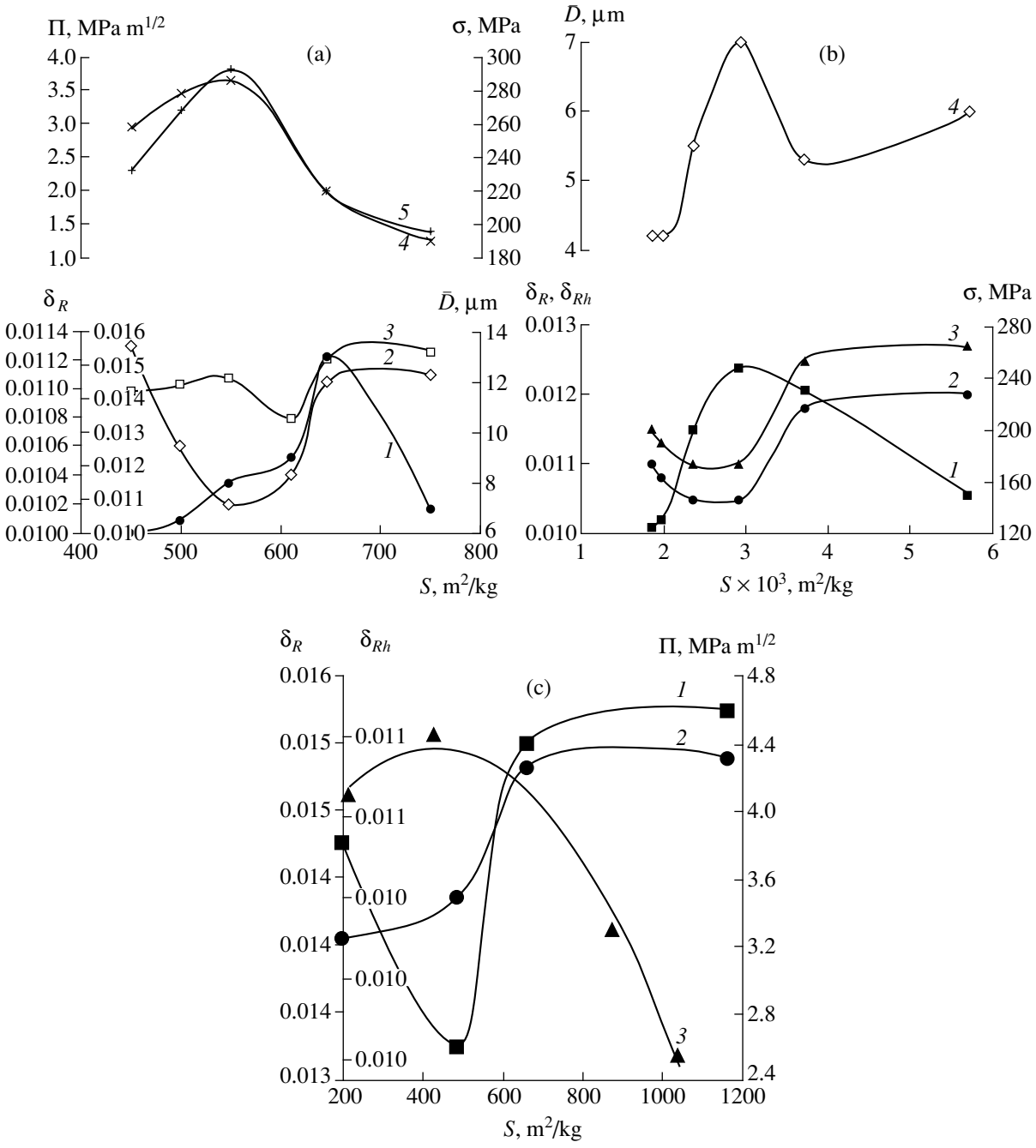

Fig. 1. Plots of the structural parameters, microstructural characteristics, and mechanical properties of NFC samples versus the surface area S of the initial Nb_2O_5 powders of various grades: (a) commercial NBO-PT grade (V. Pyshma, Urals region), (*1*) $\bar{D}$, (*2*) δ_R, (*3*) δ_{Rh}, (*4*) Π, (*5*) σ; (b) special purity grade (Krasnyĭ Khimik plant, St. Petersburg), (*1*) σ, (*2*) δ_R, (*3*) δ_{Rh}, (*4*) $\bar{D}$; (c) special purity type powder prepared by a heterophase method (Mendeleev University of Chemical Technology, Moscow), (*1*) δ_R, (*2*) δ_{Rh}, (*3*) Π.

parameter Π measured by the edge cleavage technique. The tests were performed as described in [8] using disk samples with a diameter of 10 mm and a thickness of 1 mm. The experimental results showing variation of the σ and Π values as functions of the surface area S of the initial powders are presented in Fig. 1 together with data on the parameters of homogeneous deformation of unit cells in the coexisting rhombohedral (δ_R) and orthorhombic (δ_{Rh}) phases, the average ceramic grain size ($\bar{D}$) taken from [4–6]. As seen, the mechanical properties, as well as the parameters of crystal structure and microstructure, exhibit a nonmonotonic variation with an increasing surface area of the initial Nb_2O_5 powder. The positions of maxima in σ and Π are either

the same as in δ_R, δ_{Rh}, and $\bar{D}$ (when the latter extrema coincide) or shifted toward minimum deformations of the unit cell in the dominating rhombohedral R-phase (NBO-PT and special purity grades).

This behavior can be explained by the decrease in internal mechanical stresses in NFC samples with reduced level of spontaneous deformations. Under these conditions, even the growth in $\bar{D}$ does not negatively affect the mechanical properties of niobium ceramics, because the grain size is far from the critical value initiating microcrack formation. A more perfect character of the grain boundaries in the Nb_2O_5 powders with S values falling within the optimum interval leads to a better jointing conditions and, hence, provides for the formation of more compact and stronger ceramics.

Thus, in fabricating piezoelectric NFC articles, it is necessary to take into account a considerable effect of the dispersity of the initial Nb_2O_5 powder on the strength of final ceramics. The articles possessing high mechanical properties can be obtained only using the Nb_2O_5 powders with S values within the optimum range reported in [4–6].

Acknowledgments. The work was partly supported by the Russian Foundation for Basic Research, project no. 99-02-17575.

REFERENCES

1. E. I. Bondarenko, V. D. Komarov, L. A. Reznichenko, *et al.*, Zh. Tekh. Fiz. **58** (9), 1771 (1988) [Sov. Phys. Tech. Phys. **33**, 1071 (1988)].
2. E. I. Bondarenko, V. A. Chernyshkov, and L. A. Reznichenko, in *Piezoelectric Materials and Transducers*, Vol. 9: *Proceedings of the 1st International Interdepartmental Workshop "Physics of Strength of Ferroelectrics and Allied Materials"* (Rostov. Gos. Pedagog. Univ., Rostov-on-Don, 1991), pp. 56–60.
3. L. A. Reznichenko, V. A. Aleshin, V. A. Chernyshkov, *et al.*, in *Semiconductors–Ferroelectrics* (Rostov. Gos. Pedagog. Univ., Rostov-on-Don, 1994), pp. 123–126.
4. L. A. Reznichenko, O. N. Razumovskaya, V. D. Komarov, *et al.*, Izv. Akad. Nauk SSSR, Neorg. Mater. **26** (10), 2184 (1990).
5. L. A. Reznichenko, T. V. Donskova, O. N. Razumovskaya, *et al.*, Izv. Akad. Nauk SSSR, Neorg. Mater. **26** (10), 2190 (1990).
6. L. A. Reznichenko, O. A. Zhelnova, and L. S. Ivanova, Izv. Akad. Nauk SSSR, Neorg. Mater. **29** (6), 862 (1993).
7. A. Ya. Dantsiger, O. N. Razumovskaya, L. A. Reznichenko, *et al.*, in *High-Performance Piezoelectric Materials (Reference Book)* (Kniga, Rostov-on-Don, 1994).
8. V. P. Zatsarinnyĭ, *Strength of Piezoceramics* (Rostov-on-Don, 1978).

Translated by P. Pozdeev

Technical Physics Letters, Vol. 26, No. 12, 2000, pp. 1075–1077. Translated from Pis'ma v Zhurnal Tekhnicheskoĭ Fiziki, Vol. 26, No. 24, 2000, pp. 7–12.

Soft X-rays Generated by the Electron-Cyclotron Resonance Discharge in Heavy Gases Sustained by a High-Power Microwave Beam in a Magnetic Trap

A. V. Vodopyanov, S. V. Golubev, V. G. Zorin, A. Yu. Kryachko, A. Ya. Lopatin, V. I. Luchin, S. V. Razin, and A. N. Smirnov

Institute of Applied Physics, Russian Academy of Sciences, Nizhni Novgorod, Russia;
e-mail: avod@appl.sci-nnov.ru

Received July 4, 2000

Abstract—The soft X-ray line emission from a pulsed electron-cyclotron resonance discharge in argon, maintained by a high-power millimeter-wavelength beam in a magnetic mirror trap, was studied using a multilayer mirror X-ray monochromator. The X-ray spectrum was measured, and the absolute spectral intensity of emission was determined in a 6–17 nm wavelength range. The discharge can be used as an effective source of soft X-rays with an efficiency of the microwave to X-ray power conversion on a level of 10% and a maximum spectral power density of 7.3 kW/nm at a wavelength of 9 nm. © *2000 MAIK "Nauka/Interperiodica".*

Nonequilibrium discharge in a heavy gas (Ar, Kr, etc.) sustained in a magnetic trap by a high-power microwave under the electron–cyclotron resonance (ECR) conditions offers a promising source of the soft X-ray (SXR) radiation ($\lambda \approx 1$–20 nm) [1–4].

The SXR production in this source is determined by the following mechanism. Under significantly nonequilibrium discharge conditions ($T_e \gg T_i$, where T_e and T_i are the electron and ion temperatures in the plasma, respectively), a large number of multicharged ion species are formed, which occur in different charge (ionization) states [5, 6]. The electron-impact excitation of these species followed by their spontaneous radiative de-excitation is just what accounts for the soft X-ray line emission. The radiation intensity is proportional to a product of the electron and multicharged ion concentrations ($I \propto N_e N_i$), that is, to the square of the plasma density N_e^2 (under the quasi-neutrality conditions $N_i \approx N_e/\bar{z}$, where $\bar{z}$ is the mean ion charge in the plasma). In this context, an especially attractive factor is the high-power millimeter-wavelength radiation of modern gyrotrons [7, 8], which may significantly increase the plasma density (to $N_e \sim 10^{14}$ cm^{-3} [9]) and maintain the electron temperature on an optimum level for the formation and excitation of multicharged ions ($T_e \sim$ 1 keV).

Our first experiments with ECR discharge pumped with millimeter-wavelength gyrotron radiation [3, 4] confirmed the high efficiency of the SXR line generation in this system: the microwave to X-ray power conversion efficiency (at an X-ray wavelength on the order of 10 nm) reached 25%. However, the first measurements possessed a preliminary character and were performed without providing for a sufficiently high spectral resolution. The X-ray wavelength was estimated [3, 4] based on analysis of the signals from absolutely calibrated X-ray detectors (SPPD-11-04 pin-diodes) using interchangeable transmission filters made of various materials. This analysis only allowed the soft X-ray spectral range to be roughly estimated as extended from 4.5 to 12 nm.

The microwave to X-ray power conversion efficiency was estimated assuming that the X-ray intensity and the spectral sensitivity of detectors are constant in the range studied. In order to determine more precisely the SXR generation efficiency, it was necessary to study the emission spectrum more thoroughly. For this purpose, we have measured the SXR line spectrum using a monochromator based on a multilayer X-ray mirror.

The experiments were performed on a setup schematically depicted in Fig. 1. The microwave pumping radiation was produced by gyrotron *1* operating at a frequency of 37.5 GHz with a pulse duration of 1 ms and a maximum microwave power of 130 kW. The linearly polarized gyrotron radiation was focused by a dielectric lens *2* into a vacuum discharge chamber *3*, the microwave intensity in the focal plane being no less than 10 kW/cm^2. The working gas (argon) was supplied to the chamber via a pulse valve *4*. The vacuum chamber was placed into an axisymmetric magnetic mirror trap composed of two identical solenoids *5* and *6* connected in series. The magnetic field pulse duration in the trap

1063-7850/00/2612-1075$20.00

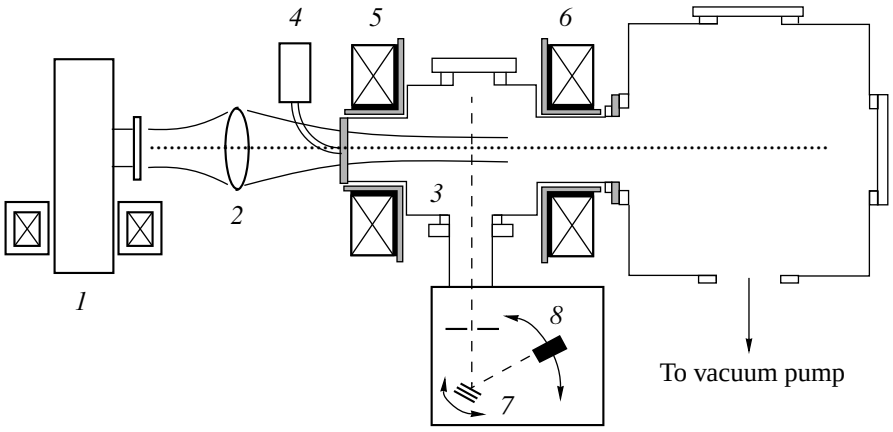

Fig. 1. Schematic diagram of the experimental setup (see the text for explanations).

was 13 ms. The maximum value of the magnetic field strength in the plugs was 2.5 T, the length of the magnetic trap was 25 cm, and the mirror ratio was 3.4.

The SXR line emission intensity was measured with a monochromator employing a multilayer X-ray mirror *7* as the dispersive element and an absolutely calibrated pin-diode *8* of the SPPD-11-04 type as the X-ray detector. The pin-diode input window was protected from visible and UV radiation by a deposited aluminum layer. The X-ray mirror and detector were mounted on a $\varphi - 2\varphi$ goniometer. This scheme, while providing a moderate spectral selectivity, possessed a sufficiently high sensitivity. In our experiments, the multilayer mirrors were based on Mo–B_4C (operating range 6.5–13 nm) and Mo–Si (12.6–20 nm) structures. The mirror reflection factor varied within 0.1–0.4, depending the wavelength range [10]. The instrumental transmission function width, also depending on the wavelength, varied from 1 to 2 nm.

Figure 2 shows the results of our spectral measurements plotted as the SXR line intensity versus wavelength. The data were processed so as to take into account the spectral selectivity of the pin-diode, the reflection factor of the multilayer X-ray mirror, and the width of the instrumental function; the measurements were taken at a maximum microwave power (130 kW) and an optimum argon pressure ($p \approx 2 \times 10^{-4}$ Torr). The spectral resolution was rather low, the system being uncapable of resolving the individual lines of emission from multicharged ions. Nevertheless, the results of these measurements allowed us to determine the total power of SXR radiation generated by ECR discharge at a markedly higher precision as compared to that achieved previously [3, 4].

Under the experimental conditions studied, the size of the plasma region from which the radiation was taken (~6 cm) was markedly smaller than the distance from the plasma to the detector (36 cm). For this reason, the total SXR line emission power was estimated by approximating the discharge with a point X-ray source situated at the center of the magnetic trap. Assuming the X-ray emission distribution to be isotropic, the total SXR power generated by the ECR discharge was evaluated as 16 kW. This allowed us to estimate the microwave to SXR power conversion efficiency as $16/130 \approx 0.12$.

Thus, the results of our experiments confirmed the previous conclusion that the main part of the soft X-ray line emission from an ECR discharge in a heavy gas, sustained by a high-power microwave beam in a magnetic mirror trap, falls within the wavelength interval in the region of $\lambda \sim 10$ nm. The ECR discharge is an effective source of soft X-ray line emission with a microwave to X-ray power conversion efficiency on the level of 10%.

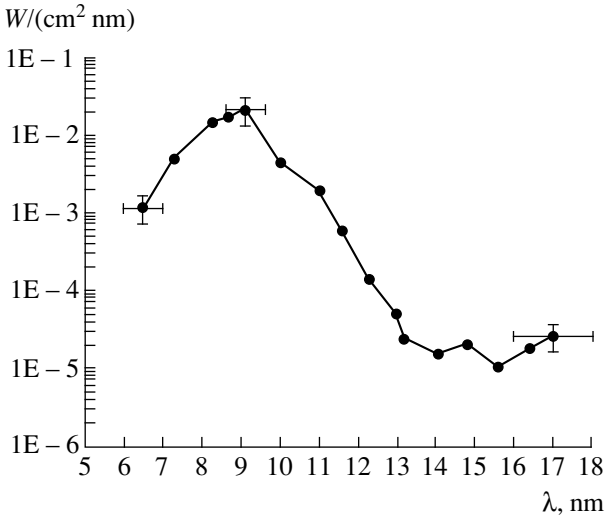

Fig. 2. The plot of absolute spectral intensity versus wavelength for the SXR line emission measured by a pin-diode at a distance of 36 cm from the electron–cyclotron discharge center. The emission was taken from the region accounting for a ≈1/20 of the total plasma volume.

Acknowledgments. The work was supported by the Russian Foundation for Basic Research, project nos. 00-02-16480 and 98-02-16621.

REFERENCES

1. J. H. Booske, F. A. Aldabe, R. F. Ellis, and W. D. Getty, J. Appl. Phys. **64** (3), 1055 (1988).
2. Y. Arata, S. Miyake, H. Kishimoto, *et al.*, Jpn. J. Appl. Phys. **27** (7), 1281 (1988).
3. S. V. Golubev, V. G. Zorin, Yu. Ya. Platonov, and S. V. Razin, Pis'ma Zh. Tekh. Fiz. **20** (4), 7 (1994) [Tech. Phys. Lett. **20**, 135 (1994)].
4. S. V. Golubev, Yu. Ya. Platonov, S. V. Razin, and V. G. Zorin, J. X-ray Sci. Technol. **6**, 244 (1996).
5. R. Geller, in *Electron Cyclotron Resonance Ion Sources and ECR Plasmas* (Inst. of Physics, Bristol, 1996).
6. S. V. Golubev, S. V. Razin, A. V. Vodopyanov, and V. G. Zorin, Fusion Technol. **35** (1T), 288 (1999).
7. A. L. Goldenberg and A. G. Litvak, Phys. Plasmas **2** (6), 2562 (1995).
8. M. Thumm, Appl. Surf. Sci. **111**, 106 (1997).
9. A. V. Vodop'yanov, S. V. Golubev, V. G. Zorin, *et al.*, Pis'ma Zh. Tekh. Fiz. **25** (14), 90 (1999) [Tech. Phys. Lett. **25**, 588 (1999)].
10. S. S. Andreev, S. V. Gaponov, N. N. Salashchenko, *et al.*, Proc. SPIE **3406**, 45 (1998).

Translated by P. Pozdeev

Technical Physics Letters, Vol. 26, No. 12, 2000, pp. 1078–1080. Translated from Pis'ma v Zhurnal Tekhnicheskoĭ Fiziki, Vol. 26, No. 24, 2000, pp. 13–18.

The Noise Characteristics of YBCO Films with Strong Pinning

I. A. Khrebtov*, A. D. Tkachenko*, K. V. Ivanov*, B. Dam, F. E. Klaassen**, and J. M. Huijbregtse****

** Vavilov Optical Institute, State Scientific Center of the Russian Federation, St. Petersburg, 190164 Russia*

*** Vrije University, Amsterdam, Netherlands*

Received June 6, 2000

Abstract—The noise characteristics of $YBa_2Cu_3O_{7-x}$ films prepared by the laser ablation technique on $SrTiO_3$ substrates were studied. The epitaxial YBCO films possess a perfect structure and are characterized by a narrow superconducting transition, strong pinning, and a very small flicker noise. In the normal state, the $1/f$ noise increases with the dislocation density. The minimum noise level with a Hooge parameter of $(2–3) \times 10^{-6}$ was observed at a disc location density of 8–12 μm^{-2}. © *2000 MAIK "Nauka/Interperiodica".*

The investigation of the nature of noise in high-temperature (high-T_c) superconductor (HTSC) films and the study of a relationship between the noise level and parameters of the film deposition technology are important steps on the way to increasing noise threshold characteristics of various cryoelectronic devices such as SQUIDs and IR detectors (including bolometers) [1, 2]. It should be noted that, owing to developments in the HTSC film technology since the discovery of high-temperature superconductivity, the Hooge noise parameter α(100 K) in the normal state of modern materials has been reduced from 10^6 to 10^{-4} [1–3]. Nevertheless, even a minimum α(100 K) value reported for HTSC films is several orders of magnitude higher than the α values typical of semiconductors.

Another point of practical interest are the HTSC films characterized by strong pinning and, accordingly, high values of the critical current density j_c. Recently [4], it was reported that structurally perfect YBCO films were obtained on $SrTiO_3$ substrates and characterized by $j_c = 10^8$ A/cm^2 at $T = 4.2$ K. In this context, it was of interest to study the structural, charge transport, and noise properties of these films simultaneously.

The epitaxial *c*-oriented $YBa_2Cu_3O_{7-x}$ films with a thickness of 160–200 nm were deposited onto (100)$SrTiO_3$ substrates by the laser ablation technique using a pulsed excimer laser [5]. The $SrTiO_3$ substrate plane orientation relative to the *c*-axis varied within 0.078°–0.14°. The YBCO films possessed a highly perfect structure, which was confirmed by a small FWHM value $\Delta\omega$ of the 005 peak on the X-ray rocking curve (see table). The test samples, having the form of bridges (dimensions indicated in the table) between Ag contacts, were prepared by standard photolithographic techniques. The samples were mounted in a vacuum cavity of a liquid-nitrogen cryostat. The structure quality was checked by X-ray diffraction. The dislocation density (*DD*) in the films was controlled by changing

Characteristics of YBCO films

Parameter	Sample				
	11B	67A	13A*	13PA1	13PA2
t, nm	202	154	158	158	158
A, μm^2	6×500	17×50	45×500	17×500	25×500
Rn, Ω	252	32	79	150	100
$\Delta\omega$, deg	0.1	0.14	0.17	0.17	0.17
DD, μm^{-2}	12.5	8.3	99	99	99
$\alpha(300\ K) \times 10^{-4}$	7.0	0.78	220	4.7	8.4
$\alpha(100\ K) \times 10^{-6}$	2.0	3.0	1000	43	160

Notes: * unannealed sample; Rn is the sample resistance in the normal state at $T \sim 100$ K.

1063-7850/00/2612-1078$20.00 © 2000 MAIK "Nauka/Interperiodica"

the substrate temperature in the course of the laser-sputter deposition. The *DD* was determined by chemical etching in combination with the atomic force microscopy, and the critical current density was measured by the torsional-magnetometric technique [4].

The HTSC film noise was measured by connecting the sample bridges in a scheme with load resistor. The signal was transferred to the preamplifier input via a resonance step-up transformer, which provided for a noise level of the measuring circuit on a level of 0.2 nV/Hz$^{1/2}$ at a frequency of f = 12.5 Hz for a bridge resistance of $R_b < 1\ \Omega$ and 1 nV/Hz$^{1/2}$ for $R_b > 30\ \Omega$. The transformer was not used during the noise spectrum measurements in the frequency range from 1 to 80 Hz. In this regime, the sensitivity of the measuring circuit was determined by the preamplifier noise, which amounted to 4 nV/Hz$^{1/2}$ f = 12.5 Hz. Since the films exhibited a very low excess current noise in the normal state, it was necessary to use bias currents with a density of up to 10^6 A/cm^2.

The noise level as a function of the sample resistance and bias current density was studied in the temperature interval from 78 to 300 K. The *DD* value was varied from 8 to 100 μm^{-2}. The temperature dependence of *dR*/*dT* was studied by measuring the YBCO bridge response under modulated IR irradiation. The noise properties of various samples were compared in terms of the well-known Hooge noise parameter $\alpha = V_{1/f}^2 NAft/(IR)^2$, where $V_{1/f}^2$ is the spectral power density of the 1/*f* noise, *I* is the bias current, *N* is the charge current density in the HTSC film (in the normal state, $N = 10^{21}$ cm^{-3}), *A* is the bridge area, *t* is the bridge thickness, and *f* is the frequency [6].

The main results of our investigations are summarized in the table and in Figs. 1 and 2. The YBCO films studied exhibit a narrow superconducting transition at T_c = 89.0 K ($T_c < 0.5$ K). It should be noted that all the bridge samples remained fully superconducting ($R_b = 0$, T = 78 K) at $j = 4 \times 10^6$ A/cm^2, whereby no excess noise was observed above the noise level of the measuring circuit (~0.2 nV/Hz$^{1/2}$). As seen from Fig. 1, the room-temperature noise spectrum of a sample with high dislocation density (*DD* = 99 μm^{-2}) is close to a typical pattern of $1/f^a$ noise with $a \sim 1.1$. At the same time, a sample in the normal state exhibits a weaker frequency dependence at $f < 10$ Hz.

The Hooge noise parameter α(100 K) is markedly smaller for the samples with low dislocation density (*DD* = 8.3–12.5 μm^{-2}) than in those with high *DD* value (99 μm^{-2}). The best samples in the normal state are characterized by α(100 K) = (2–3) × 10^{-6}. For these α values, the current noise exceeds the Johnson noise only by a factor of 1.5–2. In the samples with *DD* = 99 μm^{-2}, the Hooge parameter did not fall below (43–160) × 10^{-6}, and even this level was achieved after an additional annealing that improved the crystal structure of the YBCO film. As a result of this annealing, the α(100 K) value in samples of the 13A type decreased (e.g., by a factor of 23 for 13PA1) but still remained above the noise level observed in the samples with low dislocation density. Apparently, the annealing reduced the density of defects acting as a source of noise. Note

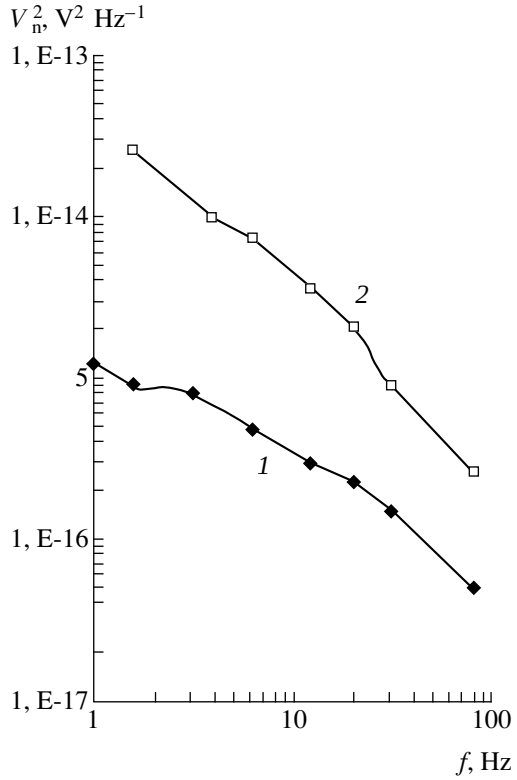

Fig. 1. Noise power density spectrum $V_n^2(f)$ of the 13A sample measured at (*1*) T = 92 K (R_b = 79 Ω; I = 29 mA) and (*2*) T = 300 K (R_b = 222 Ω; I = 13 mA).

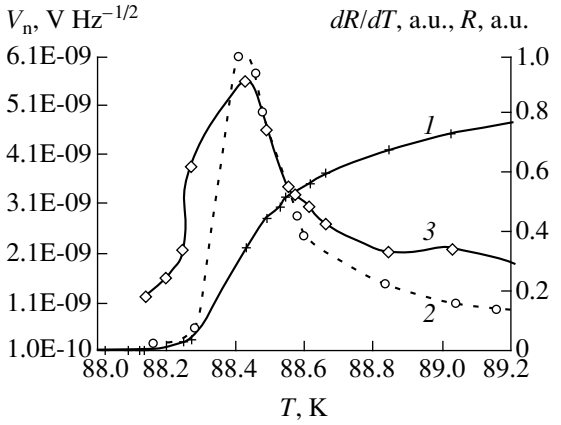

Fig. 2. Temperature variation of (*1*) the sample resistance *R*, (*2*) *dR*/*dT*, and (*3*) the noise voltage V_n at a frequency of f = 12.5 Hz for the 13PA2 sample (I = 8.8 mA; R_b = 100 Ω; TCR = 5.8 K^{-1}).

that the α(100 K) value in annealed samples approached the level typical of samples with a low dislocation density. This experimental fact indicates that the excess noise at room temperature is weakly dependent on the dislocation density. Apparently, there are some other factors (e.g., oxygen transitions between positions 01 and 05 of the CuO planes in the lattice) that play an essential role in the mechanism of the $1/f$ noise in this temperature interval [7].

Figure 2 shows the results of noise measurements performed with one of the bridge samples in the region of the superconducting transitions, where the $2/f$ noise exhibits an extremal shape. As seen, the noise peak coincides in position with the dR/dT maximum. Since no noise spectrum measurements (hindered by the transformer operating in the resonance regime) in the region of the superconducting transition were performed in this stage, we can only make preliminary conclusions concerning the nature of this noise. Not excluding the sources related to equilibrium or local temperature fluctuations [8, 9] or the conductivity fluctuations due to variations of the superconducting phase fraction during the current passage in the transition region [10], we nevertheless believe that the noise peak in the middle of the transition is related to a phonon noise of the HTSC bridge connected to the bottom of the liquid-nitrogen vessel via a thermal conductivity G. This noise component is inherent in bolometers used as thermal radiation detectors. In this case, the thermal regime of the YBCO bridges is the same as that employed in bolometers.

For the 13PA2 sample, the measured characteristics are $R = 35\ \Omega$, $I = 8.8$ mA, $G = 3.5 \times 10^{-3}$ W/K, and the temperature coefficient of resistance (*TCR*) is 5.8 K^{-1}. Taking into account these values and the calculated heat capacity of the $SrTiO_3$ substrate ($5 \times 5 \times 1$ mm), the calculated phonon noise at the point of the superconducting transition (where the *TCR* value is maximum) is 1.1×10^{-8} $V/Hz^{1/2}$ for $f \ll 12.5$ Hz, which is two times the value measured at $f = 12.5$ Hz. For the 11B sample, the discrepancy factor is 4.5. The difference between the measured noise level and the calculated value is probably explained by a large time constant of the "bolometer structure" comprising the bridge and a massive substrate. The calculation did not take into account a decrease in the phonon noise level related to a thermal time constant that was not measured. To elucidate the peak noise mechanism, it is necessary to study the noise of HTSC bridges of smaller size in which the thermal conductivity is determined only by the thermal resistance at the film–substrate boundary, while the effect of the substrate heat capacity upon the phonon nose frequency spectrum can be ignored.

In concluding, it should be pointed out that the YBCO films studied are the first HTSC films characterized by a Hooge noise parameter in the normal state on a level of $\sim 2 \times 10^{-6}$, which is close to the values in crystalline semiconductors. It was established that the excess noise drops with decreasing dislocation density. The record noise characteristics are provided by the perfect structure of the YBCO films grown on high-quality $SrTiO_3$ substrates. The YBCO films grown previously on the $SrTiO_3$ substrates with $\Delta\omega = 0.3$ deg possessed a markedly higher value of the Hooge noise parameter: $\alpha(100\ K) = 3 \times 10^{-4}$ [2].

Acknowledgments. The work was supported by the Russian Federal Program "Superconductivity" (project no. 98031) and by the FOM Program (Netherlands).

REFERENCES

1. L. B. Kiss and P. Svedlindh, IEEE Trans. Electron Devices **41**, 2112 (1994).
2. I. A. Khrebtov, V. N. Leonov, A. D. Tkachenko, *et al.*, Proc. SPIE **3287**, 288 (1998).
3. S. F. Karmanenko, A. A. Semenov, I. A. Khrebtov, *et al.*, Supercond. Sci. Technol. **13**, 273 (2000).
4. B. Dam, J. M. Huijbregtse, F. C. Klaassen, *et al.*, Nature **399**, 439 (1999).
5. B. Dam *et al.*, Appl. Phys. Lett. **65**, 1581 (1994).
6. F. H. Hooge and T. G. Kleinpenning, Rep. Prog. Phys. **44**, 479 (1981).
7. A. V. Bobyl, M. E. Gaevskii, S. F. Karmanenko, *et al.*, J. Appl. Phys. **82**, 1274 (1997).
8. R. F. Voss and J. Clarke, Phys. Rev. B **13**, 556 (1976).
9. V. I. Kozub, Phys. Rev. B **49**, 6895 (1994).
10. Yi Song, Anupam Misra, P. P. Crooker, and J. R. Gaines, Phys. Rev. B **45**, 7574 (1992).

Translated by P. Pozdeev

Technical Physics Letters, Vol. 26, No. 12, 2000, pp. 1081–1083. Translated from Pis'ma v Zhurnal Tekhnicheskoĭ Fiziki, Vol. 26, No. 24, 2000, pp. 19–23.

Mechanical Fracture in Transparent Dielectrics under the Action of a Focused Laser Radiation

V. N. Strekalov

Moscow State University of Technology (STANKIN), Moscow, Russia;
e-mail: stvn@sec.ru

Received July 3, 2000

Abstract—A model is proposed for the process of laser-induced fracture in transparent dielectrics. The fracture occurs when mechanical stresses created in the crystal lattice by a spatially inhomogeneous cloud of nonequilibrium electrons exceed a threshold value. Relationships between of the mechanical stresses, the laser beam parameters and the crystal properties are established. Regions of the most probable primary crack formation are determined. © *2000 MAIK "Nauka/Interperiodica".*

The problem of determining the mechanism of laser-induced damage in solids arose simultaneously with the initial observations of this effect [1]. There are several reviews devoted to this problem [2–6]. In transparent dielectrics, the following destructive mechanisms are considered as most important:

(i) Thermal mechanisms (ohmic losses, heating of the sample up to the melting and evaporation temperatures, formation of thermoelastic stresses, and thermochemical processes).

(ii) Phonon mechanisms (generation of hypersound, optical phonons, and acoustoelastic stresses).

(iii) Mechanisms related to the lattice imperfections (dislocations; residual mechanical stresses; and impurities, which are universally present in pure samples).

(iv) Mechanisms connected with the nonuniformity of laser beam caused by the self-focusing and the generation of ponderomotive forces.

(v) Mechanisms associated with the electron avalanche formation and the multiphoton optical absorption.

Considering various experimental conditions, preference is given to different destructive mechanisms; however, experimental data do not usually agree well with numerical results [4, 5] and the main laser-induced damage mechanism has not been chosen. From time to time, new hypotheses concerning the destructive mechanisms appear, which require experimental verification. Among these, we can mention nonthermal mechanisms of the direct action of intense light on the lattice leading to the defect formation and amorphization of the crystal [7, 8] as well as similar thermal mechanisms [9].

At the same time, the problem of describing the laser-induced damage becomes more topical because of a rapidly increasing number of engineering applications of high-power lasers and utilization of a laser radiation with new parameters (ultraviolet spectral range, femtosecond pulses). In view of the importance of the discussed problem, it would be expedient to recall a mechanical fracture model [10] that takes into account mechanical stresses arising in the crystal due to the scattering of nonequilibrium electrons by the crystal lattice. In [10], a spherically symmetric layer of thickness h enveloping the focal region was considered. A difference between the pressures of light-heated electrons inside and outside the layer causes the extension and, upon exceeding the levels of tolerable mechanical stresses, mechanical fracture of this layer. A model proposed in [10] is not very good because the h-layer is specified arbitrarily. In this paper, we describe a more rigorous model of this type that does not use arbitrarily selected layers and present some numerical results obtained with this model. The results correlate well with known experimental data. The scheme used to obtain these results is as follows:

1. We consider a spherically symmetric cloud of nonequilibrium electrons with the concentration $n_e(r)$ and the "temperature" $T_e(r)$. In the case of transparent dielectrics, this cloud is formed as a result of either a multiphoton optical absorption or an electron avalanche formation (the model can also be extended so as to apply to other objects).

2. We take into account the scattering of nonequilibrium electrons by crystal imperfections, which include phonons, impurities, dislocations, metal inclusions, grain boundaries, and the sample surface. In this study, we restrict our consideration to the scattering of electrons by charged impurities usually present in pure transparent dielectrics.

3. The electron scattering causes the transfer of an excess momentum to the lattice and the appearance of a bulk density of mechanical forces $F(r)$. The forces $F(r)$ have a spherical symmetry whose center coincides

1063-7850/00/2612-1081$20.00

with the center of the focal spot. These forces are directed radially from the focus center and act upon the lattice.

4. Following [11], we can formulate and then approximately solve a differential equation determining mechanical stresses in the sample exposed to forces $F(r)$. In this case, it was found that tangent stresses are extending and are equal to

$$\sigma_{\theta\theta} = \sigma_{\varphi\varphi} \cong \sigma_i n_i n_e T_e \frac{a^2}{8(1-\sigma)}\frac{1}{r} \times\left\{(1-2\sigma)\frac{a^2}{2r^2}(1-e^{\alpha}) + 2\sigma e^{\alpha}\right\}, \quad (1)$$

where n_i and σ_i are the concentration and the cross section of scattering centers (charged impurities); n_e and T_e are the concentration and the "temperature" of nonequilibrium electrons at the center of the focal spot; σ is the Poisson ratio; r is the distance from the spot center to the observation point; $\alpha = -2(r/a)^2$, where a is the Gaussian distribution parameter for the intensity of the laser beam causing the generation and heating of nonequilibrium electrons.

Stresses (1) extend the lattice. They may cause the formation of a primary crack (in this case, the primary crack is a part of the spherical surface centered at the laser beam focus, which agrees with numerous experimental observations, see, e.g., [12]) and the development of this crack up to a macroscopic fracture of the sample. The primary crack is formed if the inequality $\sigma_{\theta\theta} \geq \sigma_{th}$ is satisfied. This inequality represents a natural threshold condition for the mechanical fracture caused by the laser radiation. We do not consider the effects of the radial contraction and extension of the lattice, although these effects are of great interest for the problem of laser-assisted compaction of substances.

5. Upon solving the differential equation, we can find a maximum value of the tangent stress $\sigma_{\theta\theta}$. This maximum occurs at a distance r_0 from the focal spot center, where

$$r_0 \approx a\sqrt{\frac{1-2\sigma}{8\sigma}}\left[1 + \frac{12\sigma}{1-2\sigma}\right]^{\frac{1}{4}}. \quad (2)$$

It is at this distance from the center that we may expect the formation of a primary crack.

The primary crack formation increases the scattering cross section and the local density of forces $F(r)$, which initiates an avalanche destruction.

The primary crack symmetry, the effect of residual stresses (which lower the fracture threshold and can be removed by annealing the sample), similar effects for foreign inclusions and dislocations, the lowering of the fracture threshold upon the passage to a damaged surface layer with decreased value of the threshold stress σ_{th}, and the macroscopic character of the scattering of nonequilibrium electrons by the surface causing the chip-out of a cone-shaped part—all these consequences of a proposed mechanism of the laser-induced fracture agree well with experimental facts (see, e.g., [2]).

In order to derive estimates for assessing the validity of a proposed mechanism of the laser-induced fracture, let us consider a sample (glass) with the Poisson ratio σ of about 0.25 and the ultimate tensile strength σ_{th} of about 300 kgf/cm^2 $\approx 3 \times 10^8$ din/cm^2. In nonmetal samples, the ultimate strength for compression usually substantially exceeds that for tension; therefore, in this study we do not consider problems related to contraction of the sample materials.

The dark electron concentration in pure transparent dielectrics is usually estimated at 10^{14}–10^{15} cm^{-3}. Therefore, we can assume that the concentration n_i of ionized impurities in the final stages of development of the laser-induced avalanche is about 10^{15} cm^{-3}. The cross section for the electron scattering by the impurities (σ_i) can be estimated at 10^{-14} cm^2 (we assume that the scattering cross section is determined by the Debye shielding radius and take into account the effect of the low-frequency permittivity, whose order of magnitude is estimated at 10). At the end of the laser pulse causing the development of the electron avalanche and the mechanical fracture, the concentration n_e of nonequilibrium electrons at the center of the focal spot is assumed to be 10^{22}–10^{23} cm^{-3} and the electron temperature $T_e = 0.5$ eV $= 8 \times 10^{-13}$ erg (probably, the latter value is slightly understated; however, increasing the temperature T_e improves the estimates).

Then, for a laser beam with a Gaussian diameter of $a = 1$ mm, we obtain that $r_0 \approx 0.8a$ and $\sigma_{max} \approx 7 \times 10^8$ din/cm^2. The latter value exceeds the strength threshold σ_{th} even without accounting for the other scattering mechanisms. This means that the proposed mechanism can really account for the laser-induced mechanical fracture in dielectrics.

REFERENCES

1. P. Meiker, R. Terhyun, and S. Sevidg, in *Optical Quantum Generators* (Mir, Moscow, 1966).
2. *Laser Radiation Effect (A Collection of Articles)*, Ed. by Yu. P. Raĭzer (Mir, Moscow, 1968), p. 390.
3. N. Blombergen, Kvantovaya Élektron. (Moscow) **1** (4), 786 (1974).
4. Laser-Induced Damage and Laser Radiation Scattering in Solid Transparent Dielectric, Tr. Fiz. Inst. Akad. Nauk SSSR **101**, 147 (1978).

5. A. A. Manenkov and A. M. Prokhorov, Usp. Fiz. Nauk **148**, 179 (1986) [Sov. Phys. Usp. **29**, 104 (1986)].
6. M. F. Koldunov and A. A. Manenkov, in *Laser-Induced Damage in Optical Materials* (SPIE, Bellingham, 1999), Vol. 21, p. 3578.
7. V. N. Strekalov, Izv. Vyssh. Uchebn. Zaved., Fiz., No. 12, 90 (1988); No. 7, 5 (1989).
8. V. Strekalov, in *Laser-Induced Damage in Optical Materials* (SPIE, Bellingham, 1998), Vol. 20, p. 3244.
9. V. L. Komolov, Zh. Tekh. Fiz. **67** (5), 48 (1997) [Tech. Phys. **42**, 499 (1997)].
10. V. N. Strekalov, Author's Abstracts of Candidate's Dissertation (Moscow Institute of Physics and Technology, Dolgoprudnyĭ, 1975); Tr. MFTI, Ser. Radiotekh. Élektron. **9**, 3 (1975).
11. L. D. Landau and E. M. Lifshitz, *Course of Theoretical Physics*, Vol. 7: *Theory of Elasticity* (Nauka, Moscow, 1965; Pergamon, New York, 1986).
12. J. Martinelli, J. Appl. Phys. **37**, 1939 (1966).

Translated by A. Kondrat'ev

Technical Physics Letters, Vol. 26, No. 12, 2000, pp. 1084–1086. Translated from Pis'ma v Zhurnal Tekhnicheskoĭ Fiziki, Vol. 26, No. 24, 2000, pp. 24–30.

Long Periods in Oriented Semicrystalline Polymers at Low Temperatures

B. M. Ginzburg* and N. Sultanov**

** Institute of Machine Science, Russian Academy of Sciences, St. Petersburg, Russia*

*** Tajik State University, Dushanbe, Tajikistan*

Received June 19, 2000

Abstract—The reflection peak intensity in the small-angle X-ray scattering (SAXS) curves of oriented semicrystalline isotactic poly(propylene) and low-density poly(ethylene) films exhibits a reversible severalfold decrease upon cooling the samples to –90°C. At the same time, the other supermolecular structure parameters (long periods and the longitudinal dimensions of crystallites and amorphous regions, etc.) remain unchanged. The observed reversible SAXS peak intensity variations are explained by the fact that a part of the polymer chains penetrate from inter- to intrafibril (amorphous) regions or return back into the interfibril (crystalline) regions. © *2000 MAIK "Nauka/Interperiodica".*

X-ray investigations of the effect of temperature on the supermolecular structure of polymers were previously restricted for the most part to determining changes in the long period *d*. It was established that the *d* value increases with the temperature [1–3]. Much less of the researchers' attention was devoted to studying changes in the intensity I_m of the small-angle X-ray reflections, although this value was known either to increase with the temperature or exhibit a maximum [3]. These changes in I_m were explained by transformations of the supermolecular structure related either to the surface fusion of crystallites (a decrease in I_m) or to an additional crystallization (increase in I_m). It was assumed that no changes at all take place in the supermolecular structure at temperatures markedly lower than the annealing temperature [3]. However, our results reported below disprove this assumption.

The purpose of this work was to use the X-ray diffraction method for detecting and studying reversible changes in the supermolecular structure of oriented semicrystalline polymers at temperatures markedly lower than the temperature of preceding annealing.

Materials and methods. The samples of highly oriented films made of a commercial isotactic poly(propylene) (IPP) of the Moplen type were stretched to 400% at 120°C and annealed with free ends for 1 h at 150°C.

The films of highly oriented commercial low-density poly(ethylene) (LDPE) with a viscosity-average molecular mass of $M = 25 \times 10^3$ were uniaxially stretched to 350% at 85°C. Then the samples were studied either in the unannealed state or upon a 1-h annealing at 100°C with fixed ends.

The X-ray diffraction patterns of the samples with free ends were obtained in a laboratory chamber. The small-angle X-ray scattering (SAXS) curves were measured using a KRM-1 camera-monochromator, while the wide-angle X-ray scattering (WAXS) measurements were performed with a DRON-2.0 diffractometer (Burevestnik enterprise, St. Petersburg). Both SAXS and WAXS measurements were conducted using Ni-filtered CuK_α radiation.

Experimental results and discussion. Figure 1a shows a series of SAXS curves for IPP measured on decreasing the sample temperature from room temperature to –90°C. Analogous curves obtained in the course of subsequent heating exhibited reversible

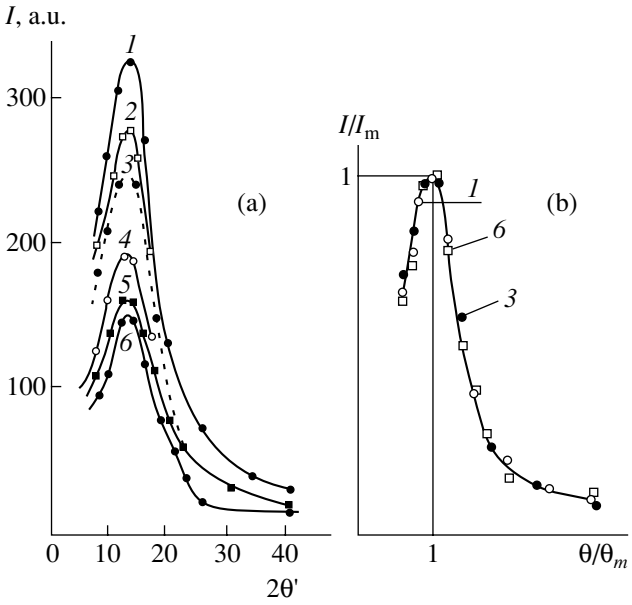

Fig. 1. SAXS curves measured for IPP films at low temperatures (reversible variation) plotted in (a) usual coordinates for T = 25 (*1*), 0 (*2*), –20 (*3*), –40 (*4*), –70 (*5*); –90°C (*6*) and (b) in the reduced coordinates (for curves *1*, *3*, and *6* from part a).

1063-7850/00/2612-1084$20.00 © 2000 MAIK "Nauka/Interperiodica"

behavior. As seen in Fig. 1a, the reflection intensity decreases to less than half of the initial value without significantly changing in shape. Moreover, the decrease in intensity with the temperature is nonuniform.

Analogous measurements were conducted for LDPE. The intensity of the SAXS reflections in these samples also dropped to about half of the initial level.

The constant shape of the SAXS intensity distribution profile was confirmed by constructing the curves in the reduced coordinates I/I_m and θ/θ_m, where I and θ are the intensity and the half-angle of scattering, respectively, and the subscript "m" refers to values corresponding to the maximum reflection intensity (Fig. 1b). The reflection shape being constant in the reduced coordinates implies that the intensity variations are caused only by changes in the difference of densities of the crystalline and amorphous regions ($\Delta\rho = \rho_a - \rho_b$).

Using the transformed curves, we have calculated the structural parameters of polymer fibrils using a method developed in [4].

It is interesting to note that neither the long period nor the longitudinal dimensions of crystalline and amorphous regions exhibit any significant changes within the error of measurements. The unchanged crystallite dimensions determined from the SAXS intensity distributions was confirmed by the constant meridional refection profiles observed for the wide-angle X-ray scattering.

A decrease in the density difference $\Delta\rho = \rho_a - \rho_b$ observed in the course of cooling may be related either to a decrease in the density of the crystal lattice or to an increase in the density of amorphous regions. A decrease in the crystal lattice density on cooling is rare in solids and is never detected in polymers. On the contrary, polymers exhibit a decrease in the crystal lattice density on heating and an increase in the density, on cooling [3]. Thus, a severalfold decrease in the SAXS peak intensity can be explained only by the increasing density in the amorphous regions.

A simple numerical estimate obtained taking into account that the SAXS peak intensity in polymers is proportional to $(\Delta\rho)^2$ and the density of amorphous regions amounts to 0.9 of the crystallite density, shows that a 2- to 3-fold change in the reflection intensity requires a 3–5% increase in the density of amorphous regions. This increase may be related to a part of the polymer chains penetrating into these regions from the interfibril space. The reverse process, whereby the chains return back to the interfibril space on heating, would account for the increase in intensity of the SAXS peaks.

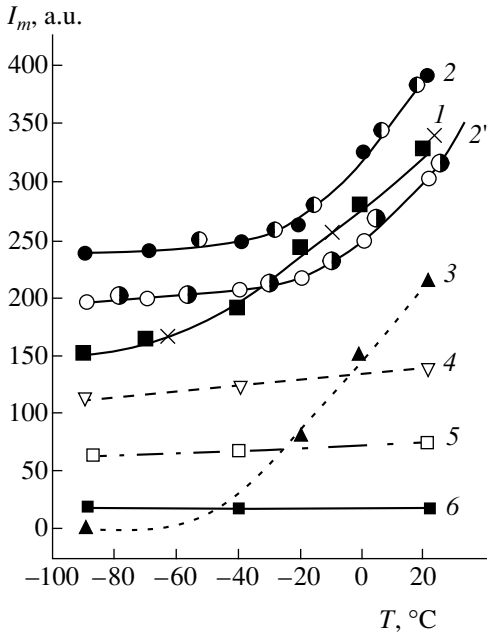

Fig. 2. The curves of SAXS peak intensity I_m vs. temperature: (*1*) IPP; (*2*) annealed IPP; (*2*') unannealed IPP (different symbols on each curve represent data measured for the sample on cooling to –90°C and the subsequent heating to room temperature).

Figure 2 shows the pattern of variation in I_m depending on the temperature. Note that the curves exhibit changes predominantly within a certain temperature interval. For LDPE, the reflection intensity I_m ceases to change below –40°C (curve *2*), although the glass transition temperature in this polymer is about –123°C. It is also interesting to note that the same LDPE not subjected to annealing behaves in the same manner, but the curve shifts down toward lower I_m values (curve *2*'). This fact probably indicates that the behavior of LDPE in the temperature range below –40°C is independent of a particular supermolecular structure and is determined entirely by the polymer nature.

For IPP, the curve exhibits variations within approximately the same temperature interval extending down to –40 to –60°C (Fig. 2, curve *1*), although the glass

The parameters of one-dimensional polymer lattices with long periods (LPs) in oriented films of isotactic poly(propylene) (IPP) and low-density poly(ethylene) (LDPE) calculated as described in [4]

Polymer	Temperature interval, °C	LP (d, Å)	LP dispersion (Δ_d)	Crystallite fraction (a) in LP	Crystallite length dispersion (Δ_a)	Transitional region fraction (t) in LP	Parameter of Γ-distribution of amorphous region length (m)
LDPE	–90–25	241	0.43	0.4	0.08	0.08	2
IPP	–90–25	354	0.38	0.5	0.13	0	2

transition temperature in this polymer is markedly higher (0°C) as compared to that in LDPE. Moreover, the I_m value in IPP keeps changing when the temperature is decreased below –60°C.

Thus, the experimental data (albeit few) indicate that the values of "reduced" characteristic temperatures obtained from SAXS measurements are not related to the glass transition temperature. We may suggest that these values reflect a retardation of the cooperative motion of the parts of numerous chains connecting fibrils with the interfibril space. Therefore, the SAXS peak intensity in the highly oriented semicrystalline LDPE and IPP films may considerably change in a reversible manner in a wide temperature range below the annealing temperature, not being accompanied by significant variation in the other characteristics of the diffraction patterns such as the long periods, the longitudinal dimensions of crystallites and amorphous regions, their size distributions, etc. The reversible changes in the SAXS peak intensities can be interpreted as being due to variations in the density of amorphous intrafibril regions caused by penetration of a part of the polymer chains into these regions from the interfibril space or the reverse process, whereby the chains return back to the interfibril space on heating. This possibility was previously discussed based on a model of fibrils with amorphous bundles [5].

For a given polymer, there exist a certain characteristic temperature T_l at which the temperature-induced variation of the SAXS peak intensity exhibits rather sharp changes. The region below T_l is characterized by decrease in the rate of supermolecular structure variation. At the same time, the T_l value is not related to the glass transition in the given polymer.

REFERENCES

1. P. H. Geil, *Polymer Single Crystals* (Interscience, New York, 1963; Khimiya, Leningrad, 1968).
2. B. Wunderlich, *Macromolecular Physics*, Vol. 2: *Crystal Nucleation, Growth and Annealing* (Academic, New York, 1976; Mir, Moscow, 1983).
3. V. A. Marikhin and L. P. Myasnikova, *Supermolecular Structure of Polymers* (Khimiya, Leningrad, 1977).
4. B. A. Asherov and B. M. Ginzburg, Vysokomol. Soedin., Ser. B **20** (4), 894 (1978).
5. B. M. Ginzburg, K. B. Kurbanov, and Yu. V. Brestkin, Vysokomol. Soedin., Ser. A **13** (8), 1749 (1971).

Translated by P. Pozdeev

Technical Physics Letters, Vol. 26, No. 12, 2000, pp. 1087–1090. Translated from Pis'ma v Zhurnal Tekhnicheskoĭ Fiziki, Vol. 26, No. 24, 2000, pp. 31–38.

Nondestructive Diagnostics of Microchannel (Macroporous) Silicon by X-ray Topography

E. V. Astrova, A. D. Remenyuk, A. G. Tkachenko, and I. L. Shul'pina

Ioffe Physicotechnical Institute, Russian Academy of Sciences, St. Petersburg, 194021 Russia

Received August 9, 2000

Abstract—It is demonstrated that X-ray topography can be used for imaging the boundary between a microchannel silicon layer and a substrate, evaluating the quality of this interface, determining the channel depth, and revealing mechanical stresses. This technique can be used for nondestructive monitoring of the structure of a microchannel layer at a spatial resolution of ≥5 μm. *© 2000 MAIK "Nauka/Interperiodica".*

The production technology and applications of microchannel (macroporous) silicon (MCS) belong to extensively developing and expanding fields [1–11]. Until recently, the quality and parameters of the porous silicon layer were determined by examining the sample cross section using optical or scanning electron microscopy (SEM) techniques. Both methods imply destructive sample preparation procedures, which is frequently undesired or even impossible. Below, we propose a method of nondestructive diagnostics of the quality of MCS layers based on the X-ray topography method.

The MCS samples were prepared using phosphorus-doped (100)-oriented silicon wafers with a diameter of 25 mm, polished from both sides to a total thickness of 300 μm. The wafers were thermally oxidized in water vapors in order to obtain a silicon oxide mask using templates with different patterns (see table). The samples with masks were subjected to a standard anisotropic etching procedure to form a surface relief with etch pits in the form of pyramids on the face side. This was followed by a photoelectrochemical etching process originally proposed by Lehmann and Foll [1], which resulted in the formation of deep pores (channels). The etching was performed in a cell schematically depicted in Fig. 1a filled with a 4% aqueous HF solution containing ethanol additives.

The cell geometry was such that the diameter D_1 of a region in contact with electrolyte was greater than the diameter D_2 of the illuminated region. This allowed us to avoid the formation of an edge groove but, instead, led to the appearance of a transitional region between microchannel (macroporous) and peripheral (nonporous) regions of the sample (Fig. 1b). The stable formation of channels (at a rate of ~0.6 μm/min) was observed for a current density of $j = 3$ mA/cm^2. Figure 1c shows a SEM micrograph of the typical sample cross section (for the 9H9 sample). The parameters of MCS samples studied are summarized in the table.

The nondestructive sample diagnostics was performed by the method of X-ray diffraction topography developed previously for determining the positions of internal interphase boundaries in heterostructures [12]. The X-ray topograms, conditionally called the sectional topograms, were obtained in the Bragg geometry as depicted in Fig. 2a for the 9H9 sample. The measurements were conducted using a symmetric 400 reflection from the back side of the sample. The topograms are called conditionally sectional because the image is obtained from an immobile sample using a relatively narrow (collimated) X-ray beam. An X-ray topogram represents essentially a projection image of the crystal cross section (Fig. 1b).

In the case under consideration, the bottom parts of the channels form a common internal boundary of the porous layer in a silicon crystal waver. This boundary can be imaged with a narrow X-ray beam using properly selected diffraction topography conditions [12]. In the general case, the boundary depth (measured from the back side of the wafer) is determined by the formula $\Delta = h\sin(\theta + \alpha)/\sin 2\theta$, where θ is the Bragg angle for a given reflection, α is the angle between the reflecting plane and the sample surface, and h is the distance mea-

Characteristics of microchannel silicon samples

Sample	ρ in, Ω cm	Template type	Template pattern	Macroporous region diameter, mm	Channel diameter d, μm	Channel spacing, μm	Channel length l, μm
907	60	AT-1	Square	20	9	30	220–250
9H9	15	AT-3	Triangle	14	3	12	200 ± 5

1063-7850/00/2612-1087$20.00 © 2000 MAIK "Nauka/Interperiodica"

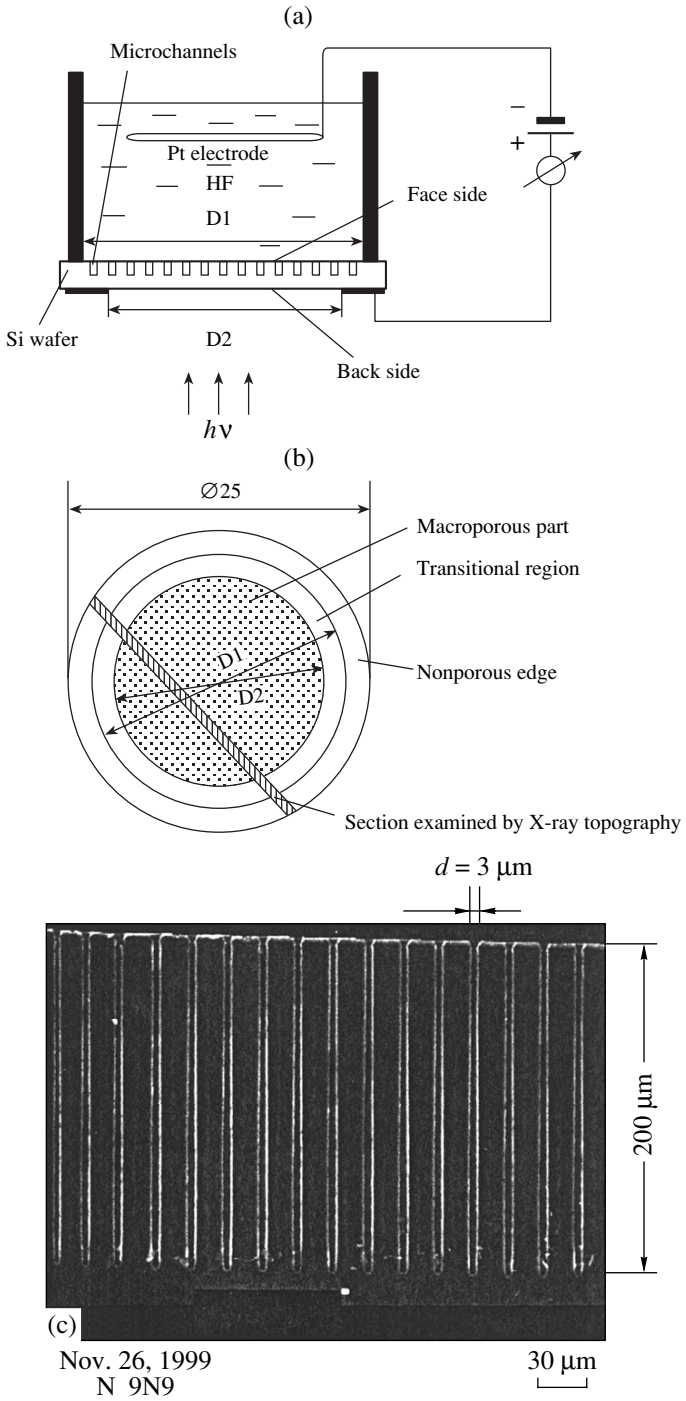

Fig. 1. Schematic diagrams illustrating the preparation technology and the structure of microchannel silicon wafers: (a) cell for the photoelectrochemical etching of channels; (b) sample configuration (dashed band indicates the position of a possible X-ray topogram cross section); (c) SEM image of channels in the sample cross section.

sured on the topogram. For the topogram in Fig. 2a, $\alpha = 0$ and $\theta = 15.5°$.

Using X-ray topograms of the type described above, it is possible to obtain useful information on the porous layer boundary and the whole layer structure provided that $\Delta \leq t$, where t is the penetration depth for X-ray beams contributing to the diffraction image. In the general case, the latter value can be estimated using formulas derived in [12], according to which $t = 200$ μm for the MoK_α and 50 μm for the CuK_α radiations.

An analysis of the X-ray topogram obtained for the 9H9 sample gave $\Delta = 102 \pm 5$ μm, which agrees with

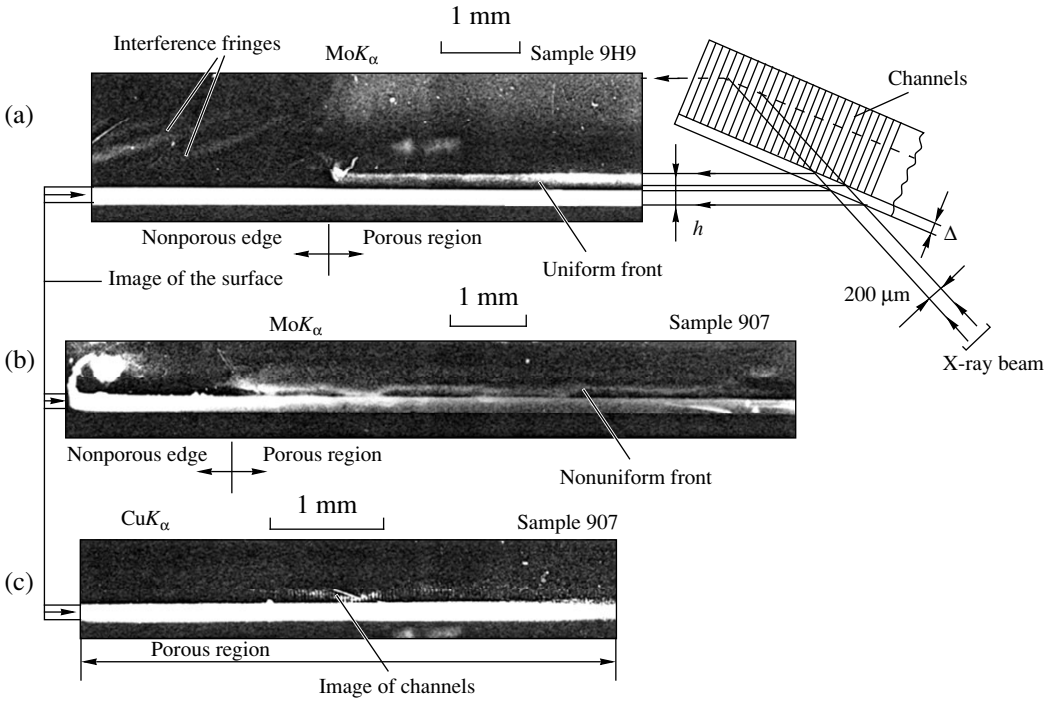

Fig. 2. Fragments of the typical X-ray topograms of microchannel silicon wafers and (the inset in a) a schematic diagram of the X-ray topography arrangement for the nondestructive diagnostics of channels in macroporous silicon: (a) sectional topogram of the sample 9H9 measured in the 400 reflection (Mo$K\alpha$ radiation); (b) sectional topogram of the sample 907 (Mo$K\alpha$ radiation); (c) topogram of the sample 907 measured using the bicrystal technique (Cu$K\alpha$ radiation).

the channel depth l = 200 μm determined using the SEM image of the cleaved sample cross section (cf. Fig. 1c), $l + \Delta$ = 300 μm. The quality of the channels can be judged by deviation from the line parallel to the sample surface (imaged by a bright line). As seen in the SEM micrograph of the 9H9 sample (Fig. 1c), the boundary is sufficiently flat. The sample is flat in the porous region and is slightly bent at the nonporous edge, which is manifested by interference bands in the topogram of Fig. 2a. The shape of these bands (the slope with respect to the surface, different thicknesses at the surface and in the bulk) indicates that the edge bending is caused by stresses arising at the boundary of the microchannel (macroporous) region as a result of the density gradient. Viewing from the back side, the nonporous edge appears as concave relative to the porous region.

In addition, the topogram shows that X-ray scattering in the microchannel (macroporous) region is more pronounced than that in the perfect (nonporous) edge region and is less pronounced than the scattering (with a typically kinematic character) at the back side. The topograms in Fig. 2 are presented in the positive contrast, whereby the maximum X-ray scattering intensity corresponds to the bright field. The images of separate channels in the porous part of the sample are not resolved, while the image of the whole macroporous region exhibits a diffuse character. The diffuse character is apparently related to a special structure of this region, which resembles to certain extent a periodic relief on the sample crystal surface.

Figure 2b shows an analogous topogram for the sample 907. As is seen, the porous layer boundary in the sample cross section is uneven: the boundary depth measurements gave a scatter in Δ from 50 to 80 μm. Here, the channel images were partly resolved by means of a low-dispersion bicrystal X-ray topography scheme using CuK_α radiation [13]. The X-ray radiation was monochromated and collimated by a perfect silicon crystal in the 331 Bragg reflection, while the sample was studied using the symmetric 400 reflection from the back side.

Figure 2c shows a fragment of the topogram obtained by this technique. As is seen, the images of channels are formed predominantly by their side surfaces (walls). The topogram reveals weak inhomogeneous stresses in the crystal lattice within the porous region, which are probably related to the uneven front of the channels. This front (i.e., the bottom boundary of the porous layer) is not revealed in the image because of the diffraction geometry employed and a strong absorption of the CuK_α radiation. The channel image resolution and the contrast of weak stresses in the crystal lattice in the porous region are obtained at the expense of using the long-wavelength radiation (CuK_α against MoK_α) and good collimation of the X-ray

beam. Both these factors are known to increase resolution and sensitivity of the X-ray topography.

Thus, we have studied applicability of the experimental method of conditionally sectional X-ray topography to nondestructive diagnostics of the porous structure of microchannel silicon wafers. Using this technique, it is possible to determine the depth of the macroporous layer and the channel spacing, to assess the quality of a boundary between the macroporous layer and single-crystalline substrate, and to reveal weak mechanical stresses in the samples. These results are of considerable practical value for the technology of heterostructures based on macroporous silicon.

Acknowledgments. The work was supported in parts by the Russian Foundation for Basic Research (project no. 98-02-18309) and by a grant from the Ministry of Science and Higher Education of the Russian Federation (project no. 99-1107).

REFERENCES

1. V. Lehmann and H. Foll, J. Electrochem. Soc. **137**, 653 (1990).
2. U. Gruning, V. Lehmann, S. Ottow, *et al.*, Thin Solid Films **276**, 151 (1996).
3. U. Grunig, V. Lehmann, and C. M. Engelhardt, Appl. Phys. Lett. **66**, 3254 (1995).
4. P. Kleinman, J. Linros, and S. Peterson, Mater. Sci. Eng. **B69**-**B70**, 29 (2000).
5. A. Birner, U. Gruning, S. Ottow, *et al.*, Phys. Status Solidi A **165**, 111 (1998).
6. K. Bush and J. Sajeev, Phys. Rev. Lett. **83** (5), 967 (1999).
7. U. Gruning, V. Lehmann, S. Ottow, *et al.*, Appl. Phys. Lett. **68**, 747 (1996).
8. J. S. Foresi, P. L. Villeneuve, J. Ferrara, *et al.*, Nature **390**, 143 (1997).
9. S. P. Beetz, Jr., R. W. Boerstler, J. Steinbeck, *et al.*, US Patent No. 5997713 (December 7, 1999).
10. E. V. Astrova, I. V. Grekhov, A. V. Naschekin, *et al.*, in *Frontiers of Nano-Optoelectronic Systems*, Ed. by L. Pavesi and E. Buzaneva (Kluwer, Boston, 2000), NATO Sci. Ser., Ser. II: Math., Phys., Chem., Vol. 6, Abstract FNOE-1.
11. E. V. Astrova, V. B. Voronkov, I. V. Grekhov, *et al.*, Pis'ma Zh. Tekh. Fiz. **25** (23), 72 (1999) [Tech. Phys. Lett. **25**, 958 (1999)].
12. I. L. Shul'pina, Kristallografiya **37** (2), 451 (1992) [Sov. Phys. Crystallogr. **37**, 234 (1992)].
13. D. K. Bowen and B. K. Tanner, *High Resolution X-ray Diffractometry and Topography* (Taylor and Francis, London, 1998).

Translated by P. Pozdeev

Technical Physics Letters, Vol. 26, No. 12, 2000, pp. 1091–1092. Translated from Pis'ma v Zhurnal Tekhnicheskoĭ Fiziki, Vol. 26, No. 24, 2000, pp. 39–42.

Effect of an Electron Beam Extracted into Gas Through a Gasodynamic Window on the Pressure Drop

L. N. Orlikov and N. L. Orlikov

Tomsk State University of Control Systems and Radioelectronics, Tomsk, 634050 Russia;
e-mail: ufo@muma.tusur.ru

Received July 25, 2000

Abstract—It is theoretically demonstrated for the first time that an electron beam extracted into gas through a gasodynamic window with a differential pumping stage produces a predictable effect (positive versus negative) on the pressure drop across the window. *© 2000 MAIK "Nauka/Interperiodica".*

As is known [1–3], an increase in the energy of electron beam extracted into gas must favor a higher pressure difference between the electron source and the gas chamber. However, in practice the beam does not change the pressure difference nor even negatively affect this parameter.

The pattern of changes in the gas flow parameters upon the electron beam extraction in a system featuring the gas (air) efflux between diaphragms *1* and *4* of a gasodynamic window [4, 5] is illustrated by a semisymmetric one-dimensional scheme depicted in the figure. A supersonic underexpanded stream of gas flows at a rate Q into a gasodynamic window with the formation of hanging (*2*) and transverse (*3*) shock waves. In the region before the transverse shock wave (Mach disk), the gas flow exhibits acceleration and the flow velocity coefficient λ increases (λ is the ratio of gas velocities in the flow to the speed of sound at the hole exit). At the gasodynamic window entrance, the flow velocity is equal to the speed of sound ($\lambda = 1$). Then the flow is accelerated again to reach the value λ_a determined by the ratio of pressure between diaphragms (P_1) to that in the gas chamber (P_0). In the limiting case, $\lambda_a = (k + 1)/(k - 1)$ (for air, $\lambda_a = 2.5$). Upon passing the Mach disk, the flow decelerates so that $\lambda_d = 1/\lambda_a$. The distance X_m to the Mach disk in a free gas stream is determined by the formula [4]

$$X_\mathrm{m} = 0.7d(kP_\mathrm{j}/P_1)^{0.5}, \quad (1)$$

where d is the gas exit hole (diaphragm) diameter; k is the gas adiabate parameter (for air, $k = 1.4$); and P_j, P_1 are the gas pressures at the diaphragm *1* exit and between the two diaphragms. Relationships between the hole capacity (conductivity) U, gas flow rate Q, the flow velocity coefficient λ, and the ability of a gas to heat up to a temperature T are as follows [4]:

$$U \sim (T/M)^{0.5}, \quad (2)$$

$$T_\mathrm{h}/T_\mathrm{c} = (1 + \lambda_\mathrm{c})^2/4\lambda_\mathrm{c}^2, \quad (3)$$

$$Q_\mathrm{c}/Q_\mathrm{h} = [2T_\mathrm{h}/T_\mathrm{c} - 1]^{0.5}, \quad (4)$$

where M is the molecular weight of the gas, and the subscripts "h" and "c" refer to the hot and cold gas, respectively.

In the working (gas) chamber, the flow velocity coefficient tends to zero and, according to relationship (3), the temperature difference tends to infinity ($\lambda \longrightarrow 0$; $T_\mathrm{h}/T_\mathrm{c} \longrightarrow \infty$). According to relationship (2), the conductivity U (on the side of the gas entrance) of the hole with the diameter d is constant, while the change in the temperature and, hence, the flow velocity coefficient tend to unity ($\lambda \longrightarrow 1$; $T_\mathrm{h}/T_\mathrm{c} \longrightarrow 1$; $U = \mathrm{const}$). As indicated above, the gas flow accelerates (so that the gas pressure drops) before and decelerates after passing by the Mach disk. According to relationship (2), this results in heating up the flow and increasing the conductivity of diaphragm *4* ($\lambda_d \longrightarrow 0$; $T_\mathrm{h}/T_\mathrm{c} \longrightarrow \infty$;

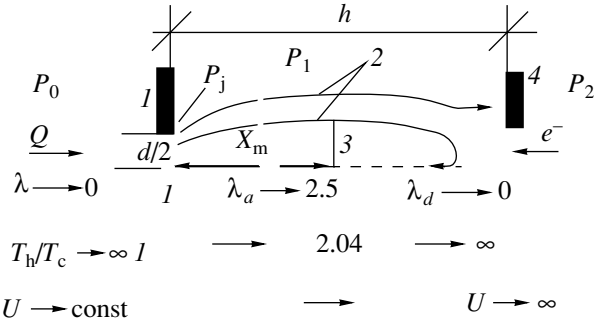

Schematic diagram illustrating changes in the gas flow parameters upon the electron beam extraction through a gasodynamic window.

1063-7850/00/2612-1091$20.00 © 2000 MAIK "Nauka/Interperiodica"

$U \longrightarrow \infty$). According to formula (3), a limiting change in the gas temperature before reaching the Mach disk may vary from 1 to 2.04. Formula (4) indicates that a drop in the gas flow rate as a result of the beam-induced gas heating cannot exceed certain value (for air, 1.75).

The coefficient δ describing the electron beam effect upon the pressure drop P_0/P_2 is determined from analysis of the function of the total heating-induced pressure variation $f(\lambda)$ determined by the formula

$$f(\lambda) = (\lambda^2 + 1)[1 - (k-1)/(k+1)]^{1/(k-1)}. \quad (5)$$

The values of this function for various velocity coefficients in air are as follows [4]:

λ	0	0.5	1	1.5	2	2.4	2.5
$f(\lambda)$	1	1.12	1.27	1.1	0.32	0.002	0

Since the total pressure drop across the gasodynamic window (P_0/P_2) is equal to the product of the drops across each diaphragm, the coefficient of the beam-induced pressure variation can be expressed through the corresponding products of the function $f(\lambda)$ in the vicinity of diaphragm *1* and in the regions in front of and behind the Mach disk:

$$\delta = [f(0)/f(1)][f(1)/f(\lambda_a)][f(\lambda_a)/f(1)] \approx f(\lambda_d)/f(\lambda_a). \quad (6)$$

Thus, a positive effect of the beam upon the pressure drop P_0/P_2 corresponds to the condition $f(\lambda_d) > f(\lambda_a)$, while a negative effect corresponds to $f(\lambda_d) < f(\lambda_a)$.

We have studied the beam effect upon the pressure drop using an electron source based on a high-voltage glow discharge [6]. Three electron beams generated at a voltage of 15–30 kV, a beam current of up to 60 mA, and a discharge pressure of 50 Pa were extracted through 0.9-mm-diam holes into a working chamber with a pressure of P_0 10 kPa. The gasodynamic window and the source were independently evacuated with pumps of the NVPR-16 type.

It was found that the electron beam negatively affects the pressure drop in a system with small distance between diaphragms ($h < X_m$), where the gas flow consists predominantly of the subsonic region in which the degree of heating and, hence, the conductivity of diaphragm *4* are large. For $h = X_m$, the pressure drop in the system with and without the beam were affected neither by the accelerating voltage nor by the discharge current. For $h = 2X_m$ ($P_0/P_1 \sim 100$; $\lambda_a = 2.15$; $\lambda_d = 0.46$), the electron beam favored a decrease in pressure in the electron source from 50 to 10 Pa. The results of direct measurements showed that, in the presence of the beam, the gas flow rate decreased by a factor of almost 1.3. A change in the pressure drop upon interruption of the beam (e.g., as a result of breakdown in the source) predicted by formula (6) is close to the experimental value:

$$\delta = f(0.46)/f(2.15) = 1.1/0.14 = 7.85.$$

Thus, the above results indicate that the electron beam effect upon the pressure drop is determined by a change in the gas flow parameters on passing by the Mach disc region and can be either positive, negative, or neutral.

REFERENCES

1. B. W. Schumacher, in *Transactions of the 8th National Vacuum Symposium and 2nd International Congress on Vacuum Science and Technology, 1961* (Washington, 1962), pp. 1192–1200.
2. A. Hershcovitch, J. Appl. Phys. **78** (9), 5283 (1995).
3. S. Schiller, V. Heising, and G. Jasch, Schweisstechnik (Berlin) **21**, 11 (1971).
4. G. N. Abramovich, *Applied Gas Dynamics* (Nauka, Moscow, 1976).
5. L. N. Orlikov and E. V. Chikin, Prikl. Mekh. Tekh. Fiz. **26** (2), 3 (1985).
6. Yu. I. Bychkov, Yu. D. Korolev, G. A. Mesyats, *et al.*, Pis'ma Zh. Tekh. Fiz. **4** (9), 515 (1978) [Sov. Tech. Phys. Lett. **4**, 206 (1978)].

Translated by P. Pozdeev

Technical Physics Letters, Vol. 26, No. 12, 2000, pp. 1093–1095. Translated from Pis'ma v Zhurnal Tekhnicheskoĭ Fiziki, Vol. 26, No. 24, 2000, pp. 43–49.

Enhancing the Spatial Resolution of Photothermal Microscopy

A. Yu. Luk'yanov

Institute of Physics of Microstructures, Russian Academy of Sciences, Nizhni Novgorod, 603600 Russia;
e-mail: luk@ipm.sci-nnov.ru

Received May 31, 2000

Abstract—It is demonstrated theoretically that the spatial resolution of the photothermal microscopy can be increased to the level of optical microscopy if the image is produced by a spatially modulated heating laser beam. © *2000 MAIK "Nauka/Interperiodica".*

It was recently demonstrated that photothermal microscopy can be remarkably effective in areas where conventional optical techniques cannot work, for example, in nondestructive evaluation of the thermal properties of various materials and structures, subsurface imaging, flaw detection, etc. [1–4].

The photothermal microscopy principle consists in the excitation and detection of thermal waves in an object absorbing time-modulated heating radiation. Accordingly, the spatial resolution in the lateral (x) direction is limited by the heating beam diameter plus the sum of the thermal diffusion lengths in the right-hand and the left-hand regions. The resolution can be improved by increasing the modulation frequency so as to reduce the thermal diffusion length. On the other hand, this also results in a lower signal amplitude and impaired sensitivity.

Alternatively, a photothermal image can be produced by modulating the position rather than the intensity of the heating beam [5]. It was shown theoretically that the image size is proportional to the derivative of the ordinary photothermal image, provided that the spatial modulation amplitude is not too large [6]. Furthermore, if the object has periodically distributed defects, the detected signal is stronger when the spatial frequency of the modulation equals that of the defects.

It must be also pointed out that the spatial resolution of the alternative approach is limited only by the heating beam diameter, which may be smaller than the thermal diffusion length. This can be demonstrated using a simple example. Consider a thin wire irradiated by a heating beam (Fig. 1). Let the beam power be distributed according to the Gaussian law and sinusoidally modulated with respect to time:

$$P_1(x, x_1, t) = \frac{P_0}{a\sqrt{\pi}}\exp\left[-\frac{(x-x_1)^2}{a^2}\right]\cos(\Omega t) = \mathrm{Re}(P(x, x_1)\exp(i\Omega t)). \quad (1)$$

We assume that the wire is thin in thermal terms, its thermal properties exhibit steps at $x = 0$, the incident power is absorbed totally, and the absorption occurs on the sample surface only. The complex amplitude of the time-dependent temperature at the frequency Ω obeys the heat transfer equation

$$\frac{d^2\tilde{T}}{dx^2} - \frac{i\Omega}{\chi}\tilde{T} = -\frac{1}{K}P(x). \quad (2)$$

The respective solutions for regions I and II are

$$\tilde{T}^I = C\exp\left(\sqrt{\frac{i\Omega}{\chi_1}}x\right) + \frac{P_0}{4K_1}\sqrt{\frac{\chi_1}{i\Omega}}\exp\left(\frac{i\Omega a^2}{4\chi_1}\right)$$

$$\times\left\{\exp\left(-\sqrt{\frac{i\Omega}{\chi_1}}(x-x_1)\right)\mathrm{erfc}\left(-\left(\frac{x-x_1}{a}\right)+\sqrt{\frac{i\Omega}{\chi_1}}\frac{a}{2}\right)\right. \quad (3)$$

$$\left. + \exp\left(\sqrt{\frac{i\Omega}{\chi_1}}(x-x_1)\right)\mathrm{erfc}\left(\frac{x-x_1}{a}+\sqrt{\frac{i\Omega}{\chi_1}}\frac{a}{2}\right)\right\},$$

$$\tilde{T}^{II} = A\exp\left(-\sqrt{\frac{i\Omega}{\chi_2}}x\right) + \frac{P_0}{4K_2}\sqrt{\frac{\chi_2}{i\Omega}}\exp\left(\frac{i\Omega a^2}{4\chi_2}\right)$$

$$\times\left\{\exp\left(-\sqrt{\frac{i\Omega}{\chi_2}}(x-x_1)\right)\mathrm{erfc}\left(-\left(\frac{x-x_1}{a}\right)+\sqrt{\frac{i\Omega}{\chi_2}}\frac{a}{2}\right)\right. \quad (4)$$

$$\left. + \exp\left(\sqrt{\frac{i\Omega}{\chi_2}}(x-x_1)\right)\mathrm{erfc}\left(\frac{x-x_1}{a}+\sqrt{\frac{i\Omega}{\chi_2}}\frac{a}{2}\right)\right\},$$

where $\chi = K/(\rho c)$, the coefficients $A = \Delta_A/\Delta$ and $C =$

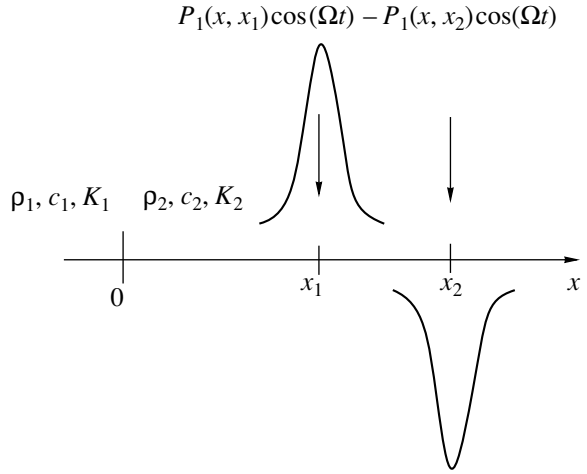

Fig. 1. Geometry of the problem.

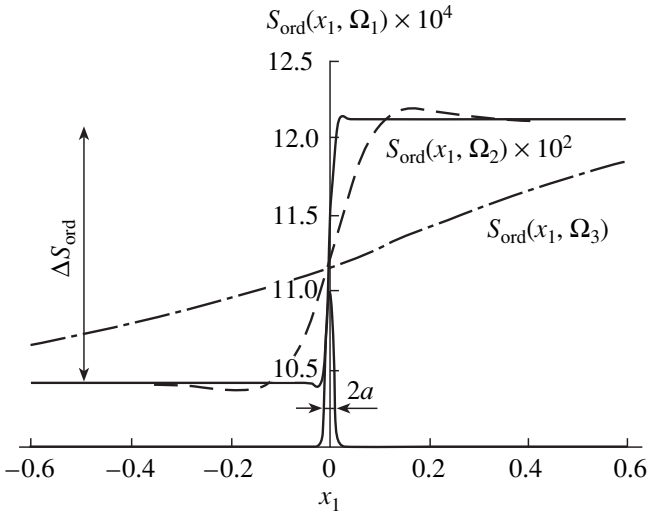

Fig. 2. Amplitude of the ordinary photothermal signal vs. the position of the heating beam for different values of the modulation frequency: $\Omega_1 = 1000$ Hz, $\Omega_2 = 10$ Hz, and $\Omega_3 = 0.1$ Hz. The other parameters are as follows: $K_1 = 8.2 \times 10^{-4}$ W/(cm K), $\rho_1 = 1.6$ g/cm^3, $c_1 = 0.6$ J/(g K), $K_2 = 5.6 \times 10^{-4}$ W/(cm K), $\rho_2 = 1.1$ g/cm^3, $c_2 = 0.75$ J/(g K), and $a = 0.01$ cm.

Δ_C/Δ being obtained from the boundary conditions

$$\tilde{T}^{I,II}\big|_{x=\pm\infty} = 0, \quad \tilde{T}^{I}\big|_{x=0} = \tilde{T}^{II}\big|_{x=0}, \qquad K_1\frac{\partial\tilde{T}^{I}}{\partial x}\bigg|_{x=0} = K_2\frac{\partial\tilde{T}^{II}}{\partial x}\bigg|_{x=0}. \tag{5}$$

Here,

$$\Delta_A = \frac{P_0}{2\sqrt{i\Omega}}\exp\left(\frac{i\Omega a^2}{4\chi_1} + \sqrt{\frac{i\Omega}{\chi_1}}x_1\right)\operatorname{erfc}\left(\frac{x_1}{a} + \sqrt{\frac{i\Omega}{\chi_2}}\frac{a}{2}\right)$$

$$+ \frac{P_0}{4\sqrt{i\Omega}}\exp\left(\frac{i\Omega a^2}{4\chi_2}\right)\left\{\exp\left(-\sqrt{\frac{i\Omega}{\chi_2}}x_1\right)\operatorname{erfc}\left(-\frac{x_1}{a} + \sqrt{\frac{i\Omega}{\chi_2}}\frac{a}{2}\right)\right.$$

$$\times\left(1 - \frac{\sqrt{K_1\rho_1c_1}}{\sqrt{K_2\rho_2c_2}}\right) - \exp\left(\sqrt{\frac{i\Omega}{\chi_2}}x_1\right)\operatorname{erfc}\left(\frac{x_1}{a} + \sqrt{\frac{i\Omega}{\chi_2}}\frac{a}{2}\right)$$

$$\left.\times\left(1 + \frac{\sqrt{K_1\rho_1c_1}}{\sqrt{K_2\rho_2c_2}}\right)\right\}, \tag{6}$$

$$\Delta_C = \frac{P_0}{2\sqrt{i\Omega}}\exp\left(\frac{i\Omega a^2}{4\chi_2} + \sqrt{\frac{i\Omega}{\chi_2}}x_1\right)\operatorname{erfc}\left(\frac{x_1}{a} + \sqrt{\frac{i\Omega}{\chi_2}}\frac{a}{2}\right)$$

$$+ \frac{P_0}{4\sqrt{i\Omega}}\exp\left(\frac{i\Omega a^2}{4\chi_1}\right)\left\{\exp\left(\sqrt{\frac{i\Omega}{\chi_1}}x_1\right)\operatorname{erfc}\left(-\frac{x_1}{a} + \sqrt{\frac{i\Omega}{\chi_1}}\frac{a}{2}\right)\right.$$

$$\times\left(1 - \frac{\sqrt{K_2\rho_2c_2}}{\sqrt{K_1\rho_1c_1}}\right) - \exp\left(-\sqrt{\frac{i\Omega}{\chi_1}}x_1\right)\operatorname{erfc}\left(-\frac{x_1}{a} + \sqrt{\frac{i\Omega}{\chi_1}}\frac{a}{2}\right)$$

$$\left.\times\left(1 + \frac{\sqrt{K_2\rho_2c_2}}{\sqrt{K_1\rho_1c_1}}\right)\right\}. \tag{7}$$

To a good accuracy, the amplitude $S(x_1)$ of the measured photothermal signal is

$$S(x_1) \approx \operatorname{Abs}\left[\int_{-\infty}^{+\infty}\tilde{T}(x, x_1)dx\right],$$

$$S(x_1) \approx \operatorname{Abs}\left[\frac{P}{2i\Omega\rho_1c_1}\operatorname{erfc}\left(\frac{x_1}{c}\right) + \frac{P}{2i\Omega\rho_2c_2}\operatorname{erfc}\left(-\frac{x_1}{a}\right)\right.$$

$$+ \frac{P}{2i\Omega}\frac{1}{\sqrt{K_2\rho_2c_2} + \sqrt{K_1\rho_1c_1}}\left(\frac{1}{\rho_1c_1} - \frac{1}{\rho_2c_2}\right)$$

$$\times\left\{\exp\left(\frac{i\Omega a^2}{4\chi_2} - \sqrt{\frac{i\Omega}{\chi_2}}x_1\right)\operatorname{erfc}\left(\frac{x_1}{a} + \sqrt{\frac{i\Omega}{\chi_2}}\frac{a}{2}\right)\sqrt{K_1\rho_1c_1}\right. \tag{8}$$

$$\left.\left.- \exp\left(\frac{i\Omega a^2}{4\chi_1} - \sqrt{\frac{i\Omega}{\chi_1}}x_1\right)\operatorname{erfc}\left(\frac{x_1}{a} + \sqrt{\frac{i\Omega}{\chi_2}}\frac{a}{2}\right)\sqrt{K_2\rho_2c_2}\right\}\right].$$

Of course, the accuracy depends on the detection technique employed.

Figure 2 depicts $S(x_1)$ for different values of Ω. As expected, the size of the discontinuity region equals the heating beam diameter plus the sum of the thermal diffusion lengths for regions I and II.

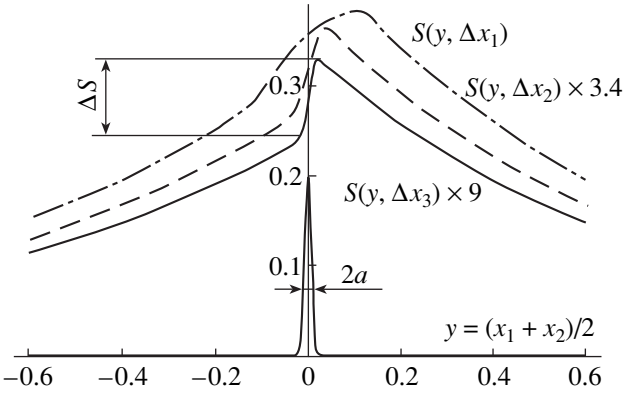

Fig. 3. Amplitude of the photothermal signal vs. the center-of-mass coordinate of the component heating beam for different values of the beam half-spacing Δx: $\Delta x_1 = 0.12$ cm, $\Delta x_2 = 0.03$ cm, and $\Delta x_3 = 0.01$ cm. The other parameters are as follows: $K_1 = 8.2 \times 10^{-4}$ W/(cm K), $\rho_1 = 1.6$ g/cm^3, $c_1 = 0.6$ J/(g K), $K_2 = 5.6 \times 10^{-4}$ W/(cm K), $\rho_2 = 1.1$ g/cm^3, $c_2 = 0.75$ J/(g K), $a = 0.01$ cm, and $\Omega_1 = 0.1$ Hz.

Now, let us add the second heating beam:

$$P_2(x, x_2, t) = -P(x, x_2)\cos\Omega t. \quad (9)$$

Figure 3 shows the amplitude of the total photothermal response as a function of the beam center-of-mass coordinate $y = (x_1 + x_2)/2$ subject to $\Delta x = (x_1 = x_2)/2$. Note that the size of the discontinuity region tends to $2a$ as x approaches zero. Let us compare the behavior of ΔS (Fig. 3) to that of its counterpart ΔS_{ord} for the ordinary photothermal microscopy:

$$\Delta S \sim \Delta x(\rho_1 c_1 - \rho_2 c_2)(K_1 - K_2)/\sqrt{\Omega}, \quad (10)$$

$$\Delta S_{ord} \sim (\rho_1 c_1 - \rho_2 c_2)/\Omega. \quad (11)$$

It is seen that one can enhance either the sensitivity or the lateral resolution in some cases by adjusting Δx and Ω.

To sum up, the spatial modulation sometimes offers considerable advantages over the ordinary modulation, especially for the photothermal (photoacoustic) microscopy of ultimate spatial resolution.

Acknowledgments. The author is grateful to M.A. Novikov for fruitful discussions that inspired this work.

REFERENCES

1. *Proceedings of the 5th International Topical Meeting on Photoacoustic and Photothermal Phenomena, Heidelberg, 1987*, Ed. by P. Hess and J. Pelzl (Springer-Verlag, Berlin, 1987).
2. A. Mandelis, *Principles and Perspectives of Photothermal and Photoacoustic Phenomena* (Elsevier, New York, 1992).
3. M. Reichling *et al.*, Opt. Eng. **33** (4), 1334 (1994).
4. K. L. Muratikov, A. L. Glazov, D. N. Rose, *et al.*, Pis'ma Zh. Tekh. Fiz. **23** (5), 44 (1997) [Tech. Phys. Lett. **23**, 188 (1997)].
5. R. S. Quimby and Z. M. Liu, Can. J. Phys. **64**, 1276 (1986).
6. A. L. Glazov and K. L. Muratikov, Zh. Tekh. Fiz. **57** (11), 2184 (1987) [Sov. Phys. Tech. Phys. **32**, 1320 (1987)].

Translated by A. Sharshakov

Technical Physics Letters, Vol. 26, No. 12, 2000, pp. 1096–1097. Translated from Pis'ma v Zhurnal Tekhnicheskoĭ Fiziki, Vol. 26, No. 24, 2000, pp. 50–55.

The Effect of Laser Radiation on the Conductivity of Poly(diacetylene)

A. B. Pavlinov and I. P. Raevskiĭ

Shakhty Branch, South-Russia State Technical University, Shakhty, Russia

Received April 4, 2000

Abstract—It is demonstrated that an increase in the dark conductivity of poly(diacetylene) (PDA) upon laser irradiation in oxygen-containing media is determined by the formation of thin conducting surface layers. Pulsed laser irradiation at an energy of 0.04 J, a wavelength of 530 nm, and a pulse duration of 20 ns increases the conductivity of the surface PDA layers by four orders of magnitude. It is supposed that the laser-induced degradation and the subsequent stabilization of the surface PDA layers are mainly determined by photooxidation.

The studies of the theoretical and practical aspects of the laser processing of polymers are important for their modification [1], technology [2, 3], and surface processing [4]. Poly(diacetylene) (PDA) represents a polymer structure based on disubstituted diacetylenes with conjugated triple bonds:

$$R - C = C - C = C - R'.$$

The value of the PDA conductivity allows one to classify this substance as a dielectric. The dark conductivity of PDA samples synthesized from various initial monomers ranges from 10^{-16} to 10^{-10} Ω^{-1} cm^{-1}. The dark current is determined by the quality and surface characteristics of crystals, the environment, and the concentration and degree of ionization of the local centers. It was demonstrated [5] that PDA conductivity changes under the action of a pulsed laser radiation in the region of strong absorption as a result of the laser-induced degradation of the surface layer by a mechanism depending on the experimental conditions.

In this paper, we present data regarding the effect of the laser irradiation in various media on the conductivity and the thickness of modified PDA surface layers. The experiments used samples representing rhomboid single crystals with planar Aquadag electrodes deposited near the rhomb vertices. The electric field could be applied in the direction either parallel or perpendicular to the axis of the polymer backbone oriented along the large diagonal of the rhomb.

The samples were irradiated from the side of the contact surface as described in [6]. The treatment was performed in the atmosphere of oxygen, air, nitrogen, or in vacuum at a residual pressure of about 0.1 Pa. A dc voltage of 300 V was applied to the sample connected in series with a resistor of markedly small resistance. We monitored the sample resistance before and after irradiation; the laser-induced current in the sample circuit; and the thickness, optical density, and color of the conducting layer emerging at the irradiated surface. The experiments used laser pulses with an energy of about 0.04 J, a wavelength of 530 nm, and a duration of 20 ns. The laser-induced current pulse and the steady-state resistance were measured by a memory oscilloscope and a teraohmmeter with a constant input voltage, respectively.

Prior to laser irradiation of the samples, we compared their dark conductivities measured in vacuum and in the atmosphere of nitrogen or air. Before these measurements, the samples were kept in the corresponding medium for a long time until the conductivity stabilized. The results of experiments showed that the dark conductivity in vacuum is smaller than that in air by several orders of magnitude. The samples exhibit the same decrease in conductivity when the air is replaced by nitrogen. Storing the samples in vacuum or nitrogen leads to a gradual decrease in the dark current to a constant level.

The dark current (both in vacuum and nitrogen) obeys the Ohm law, with the conductivity exponentially depending on the temperature. The studies of the temperature dependence of the conductivity showed that the free charge carriers are mainly generated by local centers with the activation energy ΔE = 0.8–1.0 eV regardless of the polymer chain axis orientation relative to the electric field.

It was demonstrated that the sample resistance reaches a stationary value in about 1 ms after the laser pulse action. Figure 1 demonstrates the estimates of the stationary conductivity and the thickness of the laser-modified surface layer. Figure 1a shows a plot of the quantity q, representing the logarithm of the ratio of the conductivity after irradiation in oxygen Σ to the initial (dark) value Σ_0, versus the number n of the laser pulses. Laser irradiation in air yields nearly the same result. It is seen that Σ exhibits nearly exponential growth with increasing n. For $n \geq 3$, $\Sigma/\Sigma_0 \geq 10$ and we can assume that the total conductivity is determined by that of the

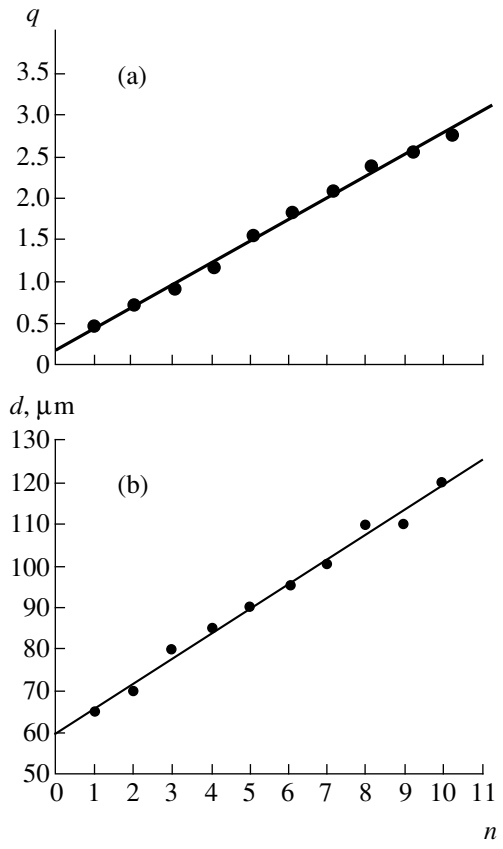

Fig. 1. Plots of (a) the logarithm of the total conductivity of a PDA sample (in relative units) and (b) the laser-modified PDA layer thickness versus the number of laser pulses.

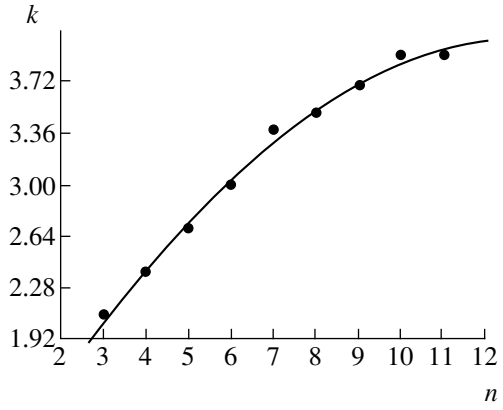

Fig. 2. A plot of the logarithm of PDA conductivity σ (in relative units) vs. the number of the laser pulses.

surface layer modified by the laser action. The results of experiments with mechanical or chemical removal of the surface layers and the optical measurements showed nearly linear dependence of the conducting layer thickness d on the number of pulses n (Fig. 1b). Note that the removal of the surface layer almost completely restores the initial state of the illuminated sample.

Let us estimate the effect of the laser irradiation on the conductivity σ. Assume that the conducting layer thickness is approximately equal to $\approx d$, the conductivity can be represented as

$$\sigma/\sigma_0 = (\Sigma/\Sigma_0)(d_0/d),$$

where σ_0 and d_0 are the conductivity and the thickness of the initial layer, respectively. Figure 2 shows a plot of the quantity k representing a logarithm of the ratio of the modified layer conductivity σ after illumination to the initial (dark) value σ_0 versus n for $n \geq 3$ (when the shunting effect of the sample is negligible).

Note that the conducting layers produced and stored in oxygen exhibit stability of the conductivity in time. However, the conductivity of layers obtained by the laser irradiation in air decreases in time, approaching the initial level (the resistance of the sample accordingly increased). The rate of these relaxation processes increases on illumination by an incandescent lamp.

The laser irradiation of the samples in vacuum or nitrogen results in a drop in the resistance followed by its recovery within about 1 ms, which can be explained by the nonstationary thermal processes. Therefore, in this case the laser irradiation does not produce any irreversible changes in the conductivity.

Thus, the effect of the laser irradiation on the PDA conductivity is explained by the formation of conducting surface layers in the oxygen-containing media. Based on the stability of such layers formed and stored in oxygen, we assume that their formation is related to the laser-induced oxidation of the PDA surface layer. The color of the irradiated surface differs from the initial one: it becomes almost red after multiply repeated exposures. The laser-induced changes in the structure of surface layers lead to a significant increase in the optical density of the samples in the wavelength range of 500–700 nm (by approximately 1.0).

REFERENCES

1. N. J. Pool *et al.*, J. Mater. Sci. **21** (2), 507 (1986).
2. H. Masuhara *et al.*, Chem. Phys. Lett. **135** (1-2), 103 (1987).
3. R. Srinivasan, Polym. Degrad. Stab. **17** (3), 193 (1987).
4. Y. Huang, Q. Lou, J. Xu, *et al.*, Chin. J. Lasers A **26** (8), 745 (1999).
5. A. B. Pavlinov, T. L. Traĭduk, T. S. Zhuravleva, and A. V. Vannikov, Khim. Vys. Énerg. **23**, 181 (1989).
6. A. B. Pavlinov, Izv. Vyssh. Uchebn. Zaved. Sev.-Kavk. Reg., Estestv. Nauki, No. 2, 90 (2000).

Translated by A. Chikishev

Technical Physics Letters, Vol. 26, No. 12, 2000, pp. 1098–1101. Translated from Pis'ma v Zhurnal Tekhnicheskoĭ Fiziki, Vol. 26, No. 24, 2000, pp. 56–63.

The Electron Paramagnetic Resonance in Copper-Modified Amorphous Carbon

T. K. Zvonareva, V. I. Ivanov-Omskiĭ, B. P. Popov, and K. F. Shtel'makh

Ioffe Physicotechnical Institute, Russian Academy of Sciences, St. Petersburg, 194021 Russia

St. Petersburg State Technical University, St. Petersburg, Russia

Received June 29, 2000

Abstract—Room-temperature EPR spectra of copper-modified α-C:H films exhibit signals due to the isolated paramagnetic copper centers and dangling carbon bonds. An analysis of variation of the EPR signal intensity depending of the annealing temperature ($T_a \le 300$°C) and relaxation of the EPR and IR absorption signals upon annealing indicates that the annealing-induced modification of the α-C:H films involves hydrogen and oxygen impurities in the amorphous carbon matrix. © *2000 MAIK "Nauka/Interperiodica".*

Owing to the unique ability of carbon to form hybridized valence orbits of different types, the atomic structure of hydrogenated amorphous carbon (α-C:H) is capable of accommodating foreign inclusions such as metal nanoclusters. This circumstance allows the amorphous carbon matrix to be used as a medium for encapsulating metal nanoclusters in order to protect them from aggressive ambient media [1]. An important question in this process is what is the character of interaction between a given metal and the carbon–hydrogen matrix. Answering this question is essentially equivalent to judging on the possibility of encapsulating the metal in the matrix without undesired carbide formation.

Below, we report on the results of the EPR study of the paramagnetic centers in α-C:H films prepared by co-sputtering graphite and copper in an argon–hydrogen plasma. The process of sample preparation is described in detail elsewhere [2]. The main task of the EPR measurements was to reveal changes in the paramagnetic states upon annealing. The samples were annealed for 1 h in vacuum. Data on the concentrations of the main components in the α-C:H films determined by the method of Rutherford backscattering (RBS) are presented in the table.

The EPR measurements were carried out at room temperature on a Se/X-2534 spectrometer. In order to increase the sample film volume in the ampules, the samples were prepared by collecting the material deposited on a substrate area of ~10 cm^2.

EPR spectra of the initial samples. Figure 1 shows a typical EPR spectrum of the copper-modified α-C:H films. As seen, the spectrum is essentially a superposition of wide and narrow components. The narrow component, characterized by the parameters $g = 2.0027 \pm 0.0006$ and $\Delta H = 11$ G, represents the well-known EPR spectrum of dangling carbon bonds [3]. The wide component can be considered as a superposition of at least two signals from axially distorted copper centers. The g values corresponding to these magnetic sates of copper are as follows: $g_\parallel = 2.36 \pm 0.06$, $g_\perp = 1.99 \pm 0.05$ and $g_\parallel = 2.71 \pm 0.08$, $g_\perp = 1.99 \pm 0.05$.

The local concentration of paramagnetic copper centers can be roughly (by the order of magnitude) estimated using the line width ΔH. The latter can be evaluated from the high-field wing as $\Delta H \sim 100$ G. Assuming that the observed line width is determined by an unresolved hyperfine structure (HFS) of signals from the copper ions, we may estimate the local concentration of copper centers to within the order of magnitude. We assume that the implicit HFS is due to four transitions related to the nuclear spin of copper $I = 3/2$ (the isotope composition ignored), with the distance between the HFS components on the order of the dipole broadening of a single transition $\Delta H_{dip} \cong g\beta S/r^{-3} \cong g\beta S n_{Cu}$ (here, $g \cong 2$ is the g value of the copper state, β is the Bohr magneton, and $S = 1/2$ is the spin of the Cu^{2+} ion). The local concentration of copper atoms estimated in this way is $n_{Cu} \sim 10^{21}$ cm^{-3} [5].

By doubly integrating the EPR spectrum, we may also estimate the ratio of concentrations of the paramagnetic copper centers and dangling carbon bonds. This ratio was estimated at 380 ± 20.

The effect of annealing. Data on the effect of vacuum annealing on the EPR signal intensity are presented in Fig. 2. An increase in the annealing temperature T_a from room temperature to 100°C leads to a

Elemental compositions of the copper-modified α-C:H films

Element	Cu	O	N	H
Concentration, at. %	22	18	1	24

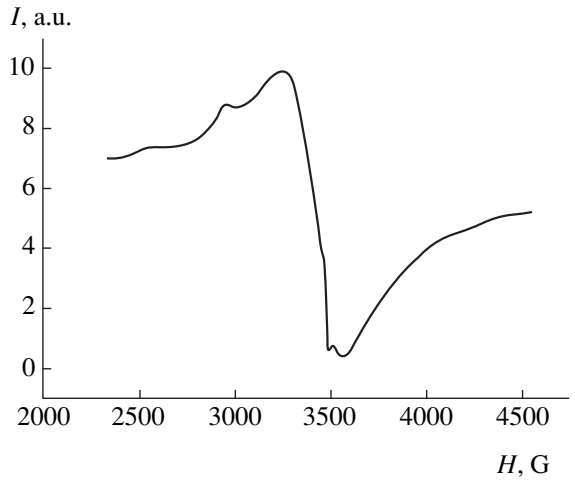

Fig. 1. Typical EPR spectrum of copper-modified α-C:H films. The ratio of concentrations of the paramagnetic copper centers and dangling carbon bonds is 380.

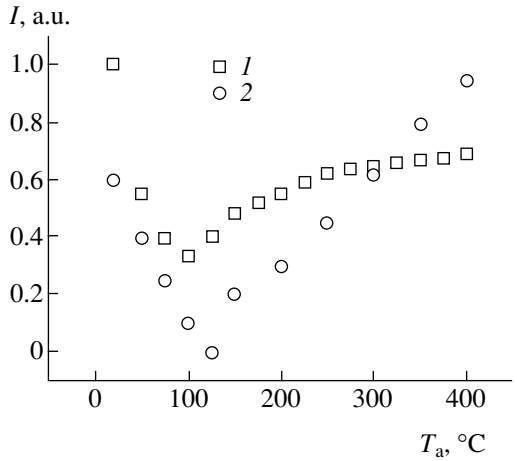

Fig. 2. Intensity of the EPR signal components from copper-modified α-C:H films versus the annealing temperature (annealing time, 1 h): (*1*) copper centers; (*2*) dangling carbon bonds.

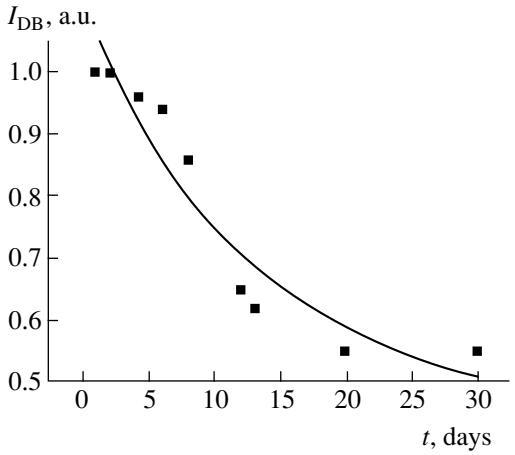

Fig. 3. Post-annealing relaxation of the EPR signal due to the dangling carbon bonds. The results were processed and approximated by a sum of two exponents with the characteristic times (a) 7.6 days and (b) 15.9 days.

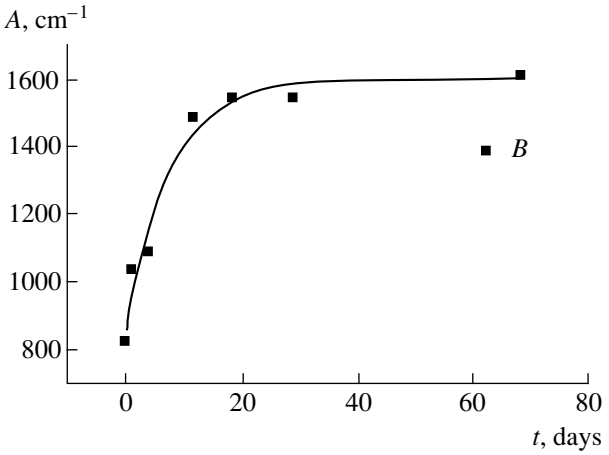

Fig. 4. Post-annealing relaxation of the IR absorption signal due to the dangling carbon bonds. The characteristic relaxation time 7.3.

decrease in intensity of the signal from copper ions (relative to the initial value), while no significant changes are observed in either shape or width of the line. As the annealing temperature increases above 100°C, the EPR line intensity begins to increase and stabilizes on a constant level of 0.7 at $T_a \sim 300$°C. At the same time, the intensity of the signal due to the dangling carbon bonds in the matrix increases almost linearly with the annealing temperature above 100°C.

Post-annealing relaxation of the paramagnetic states. We have studied time variation of the EPR signal due to dangling carbon bonds in a sample annealed at $T_a = 400$°C and then stored in an open ampule at room temperature in air. The signal intensity was found to decrease with a characteristic time of $\tau \cong 2$ weeks to reach the initial level (Fig. 3). This behavior is in satisfactory agreement with the pattern of relaxation observed for the IR absorption due to the dangling carbon bonds (Fig. 4) measured on an analogous sample. No post-annealing variation was observed in intensity of the EPR signal due to the Cu^{2+} ions.

Discussion of results. The above data indicate that copper atoms are capable of forming the paramagnetic centers of two types in hydrogenated amorphous silicon films. These centers exhibit different charged and magnetic states characterized by the configurations $3d^{10}$ (nonmagnetic state) and $3d^9$ (magnetic state).

Let us consider the effect of annealing on the magnetic states of copper and carbon bonds. First, note that most chemically active elements contained in the samples are oxygen and hydrogen (see table). The latter element is capable of forming nonmagnetic states by chemically binding (in an atomic state) to carbon and,

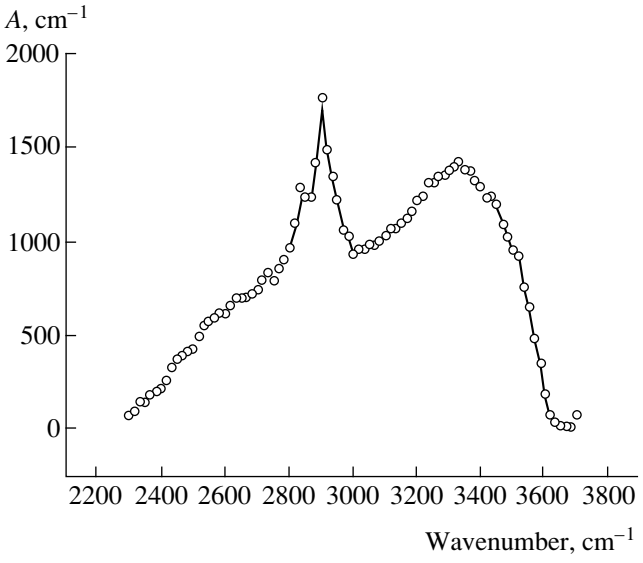

Fig. 5. The IR absorption spectrum (*A* is the absorption coefficient) showing a signal due to hydroxy groups formed in annealed copper-modified α-C:H films.

in addition, may occur in the matrix in the form of distorted (stretched) H_2 molecules bound by the van der Waals forces [5]. The simultaneous existence of these hydrogen states at room temperature in the system studied indicates that there is no significant difference between their total energies and, under certain conditions, the two states may transform into one another.

Note a correlation between variations in the intensities of both EPR signals observed on changing the annealing temperature (Fig. 2). This behavior may be evidence of a relationship between the concentrations of paramagnetic states due to the copper ions and the dangling carbon bonds.

A very small difference between the temperature of sample storage and the temperatures corresponding to decay in the EPR signal intensity (Fig. 2) indicates that the most probable factor responsible for the initial decrease in the concentration of dangling bonds is the transition of hydrogen from the molecular state (H_2 molecules) into the state bound to terminal atoms in the carbon film structure [5].

Whether the atomic hydrogen can affect the magnetic state of copper atoms is unclear if the consideration is based on the primitive structure of the copper center directly bound to carbon. However, the results of most investigations devoted to the copper atoms entering into coordination compounds show that these atoms are usually built into molecules via bridges of various types [6]. In particular, oxygen may be the bridging element. In this case, the effect of hydrogen upon the magnetic (and charged) state of copper may be related to the hydrogen–oxygen interaction with the formation of hydroxy groups, the traces of which are observed in the IR spectra of hydrogenated amorphous carbon (Fig. 5). As a result, the oxygen-bridged copper atoms acquire the $3d^{10}$ electron configuration and become nonmagnetic. One possible variant of this state was recently considered in [7].

In this context, some increase in concentration of the magnetic copper centers observed on increasing the annealing temperature from 100 to 400°C can be explained by the increasing activity of oxygen. As a result, oxygen restores to a certain extent the broken bridges between copper atoms (thus converting copper into a paramagnetic state), compensates for the effect of liberated hydrogen, and interacts with hydrogen bound to the terminal carbon atoms (Fig. 6). This circumstance may well explain the permanent growth in concentration of the magnetic states of carbon atoms with dangling bonds observed on increasing the annealing temperature (Fig. 2). The proposed structural model also readily explains relaxation of the signal of dangling carbon bonds by their interaction with hydrogen retained in the film [5].

Conclusions. The results of our investigation of the effect of vacuum annealing on the paramagnetic states show that copper in hydrogenated amorphous carbon films may occur in at least two charged states, one of these being paramagnetic. The annealing-induced modification of these copper states probably involves hydrogen and oxygen impurities present in the films.

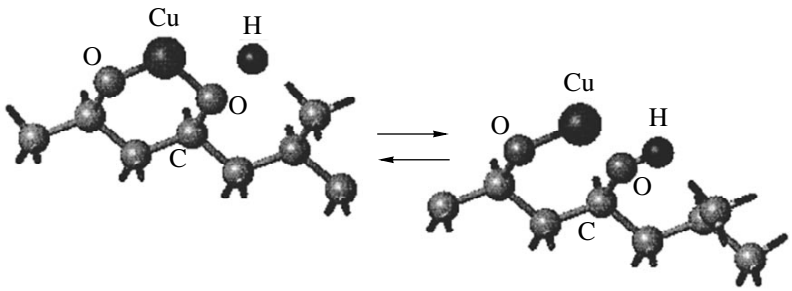

Fig. 6. A schematic diagram illustrating the main stages of formation of the paramagnetic and nonmagnetic states—involving copper, oxygen, and hydrogen atoms—in the course of annealing and relaxation of the dangling carbon bonds.

Acknowledgments. The work was partly supported by the Russian Foundation for Basic Research, project no. 00-02-17004.

REFERENCES

1. J. Jiao and S. Seraphin, J. Appl. Phys. **83** (5), 2442 (1998).
2. V. I. Ivanov-Omskiĭ, V. I. Siklitskiĭ, and S. G. Yastrebov, Fiz. Tverd. Tela (St. Petersburg) **40**, 568 (1998) [Phys. Solid State **40**, 524 (1998)].
3. D. J. Miller and D. R. McKenzie, Thin Solid Films **108**, 257 (1983).
4. S. A. Al'tshuler and B. M. Kozyrev, *Electron Paramagnetic Resonance in Compounds of Transition Elements* (Nauka, Moscow, 1972; Halsted, New York, 1975).
5. V. I. Ivanov-Omskiĭ, M. P. Korobkov, B. R. Namozov, *et al.*, J. Non-Cryst. Solids 627 (1998).
6. Yu. V. Yablokov, V. K. Voronkova, and L. V. Mosina, *Paramagnetic Resonance of Exchange Clusters* (Nauka, Moscow, 1988).
7. V. I. Ivanov-Omskiĭ and É. A. Smorgonskaya, Fiz. Tekh. Poluprovodn. (St. Petersburg) **32** (8), 931 (1998) [Semiconductors **32**, 831 (1998)].

Translated by P. Pozdeev

Technical Physics Letters, Vol. 26, No. 12, 2000, pp. 1102–1104. Translated from Pis'ma v Zhurnal Tekhnicheskoĭ Fiziki, Vol. 26, No. 24, 2000, pp. 64–69.

A Kinetic Scheme of the High-Energy Action upon a Methane Flow

Yu. G. Tynnikov and V. N. Genkin

Sibur-NN Fuel Company, Nizhni Novgorod, Russia;

e-mail: siburl@kis.ru

Received June 30, 2000

Abstract—The possible energy contributions to a gas flow, achievable under the blocking conditions, were determined in a quasi-one-dimensional approximation. The features of gas dynamics in flow reactors are considered and the conditions for obtaining various products at the reactor output are analyzed. © *2000 MAIK "Nauka/Interperiodica".*

Methods based on the high-energy (mostly, plasma) action upon a methane flow have been extensively elaborated for a long time [1, 2]. However, neither a complete kinetic scheme of such a process nor an effective practical scheme of a flow reactor has been developed. The plasmachemical reactors, used mostly for the production of acetylene from methane, were operating with the initial gas–plasma mixtures at pressures close to 0.1 MPa and temperatures in the 2000–3000 K range. The kinetic models of these processes [2, 3] were restricted to the dehydrogenation scheme including 5–10 reactions. Recently, Borisov *et al.* [4] proposed a kinetic scheme for analysis of the methane combustion process, which includes the radical formation and secondary reactions between the products (more than 80 reactions involving hydrocarbons).

In addition to the above-mentioned plasma heating, there are other methods of the high-energy action: electron and laser beams, electric heating, and so on. Weill *et al.* [5] studied the process of methane heating up to 1500 K by the Joule heat evolution in poorly conducting silicon-carbide-based elements situated in the flow. Irrespective of the means of the energy supply, it is convenient to divide the reactor into two regions in the flow direction, representing the energy deposition zone and the reaction zone. This approach, albeit rather conditional, is still useful for analysis of the features of gas dynamics in the flow reactors.

In the case of a plasmachemical reactor, this division is close to a real situation because no reactions with significant energy effect take place in the zone of energy deposition (or the gas mixing with plasma jet). When the heat is supplied to the gas by special thermal elements (as, e.g., in [5]) or by walls, the energy deposition zone may be rather extended and some energy-consuming chemical reactions may take place in this region as well. In this case, a rigorous analysis must take into account both the energy supplied by external factors and the energy effect of reactions occurring in the system.

Figure 1 shows an example of the supersonic jet flow organization, including the energy deposition and reaction zones. The latter zone is situated in the nozzle part of the gas path, which allows the flow rate (and, hence, the necessary reactor length) to be reduced. For a supersonic jet flow in a channel of constant cross section, the energy deposition zone imposes a limitation on the maximum power q supplied to the flow, which is related to the supersonic jet flow blocking effect [6]:

$$\left(\frac{q}{C_pT_0}\right)_{\max} = \frac{1}{4}\left(\lambda_1 - \frac{1}{\lambda_1}\right)^2,$$

where C_pT_0 is the enthalpy of the flow retardation at the entrance of the energy deposition zone and λ_1 is the flow velocity coefficient. For example, in a system with $\lambda_1 = 2.4$, the proposed method allows the flow enthalpy to be doubled. Similar restrictions exist for a subsonic flow.

In a supersonic reactor, we must also take into account the total pressure drop in the energy deposition

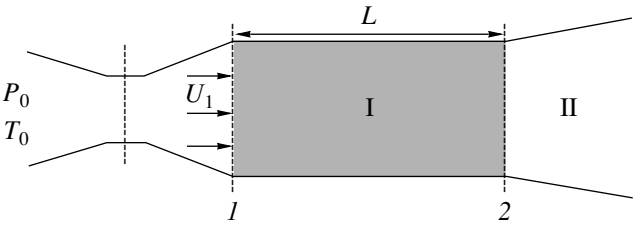

Fig. 1. Schematic diagram of a reactor channel showing the zones of (I) energy deposition and (II) reactions (nozzle region).

1063-7850/00/2612-1102$20.00 © 2000 MAIK "Nauka/Interperiodica"

zone. The change in the total pressure across this zone amounts to

$$\frac{P_{02}}{P_{01}} = \left(\frac{k+1}{2}\right)^{\frac{1}{k-1}} \frac{1+\lambda_1^2}{2}\left(1 - \frac{k-1}{k+1}\lambda_1^2\right)^{\frac{1}{k-1}},$$

where k is the isentrope coefficient. For methane with $k = 1.1$, the total pressure ratio at $\lambda_1 = 2.4$ is 0.43. This means that the pressure restores in the nozzle part of the channel to a level that is significantly lower than the initial gas pressure. Moreover, the total pressure may additionally drop on the shock waves generated in the case of strong retardation in the supersonic part of the flow.

In the case of subsonic flows (especially in systems with a sufficiently large channel expansion in the energy deposition zone), the above effects of the total pressure drop are absent and no boundary layer separation problems are encountered (the subsonic flow is accelerated rather than retarded). Nevertheless, processes in the supersonic reactors should be also considered because these systems make it possible to obtain a gain in the energy per unit mass of the final product yield as compared to the subsonic reactors (the gain is achieved at the expense of the work performed by pressure forces). In addition, the supersonic flow regimes may be most effective under conditions where the energy can be supplied only at a comparatively small pressure (relative to the initial gas pressure).

In order to take into account the joint action of the gasodynamic and kinetic effects in high-velocity flows, we use a system of equations describing the gas dynamics in a reacting mixture in a quasi-one-dimensional approximation:

$$\frac{dU}{dx} = \frac{U}{M^2-1}\left(\frac{1}{F}\frac{dF}{dx} - \frac{1}{G}\frac{dG}{dx} - \frac{k-1}{a^2 G}\frac{dW}{dx} - \frac{1}{R}\frac{dR}{dx} + \frac{k(k-1)}{a^2}\frac{F}{G}\sum\left(\frac{dN_i}{dt}\right)Q_i\right), \quad (1)$$

$$\frac{dR}{dx} = \frac{R_0}{\rho U}\sum\left(\frac{dN_i}{dt}\right),$$

$$\frac{dN_i}{dx} = -N_i\left(\frac{1}{U}\frac{dU}{dx} + \frac{1}{F}\frac{dF}{dx}\right) + \frac{1}{U}\left(\frac{dN_i}{dt}\right), \quad (2)$$

$$\frac{dP}{dx} = -\rho U\frac{dU}{dx},$$

$$\frac{1}{\rho}\sum N_i C_i\frac{dT}{dx} = \frac{1}{G}\frac{dW}{dx} - U\frac{dU}{dx} - \sum\frac{F}{G}\left(\frac{dN_i}{dt}\right)Q_i.$$

In Eq. (1), a is the speed of sound, k is the isentrope coefficient, M is the Mach number, and dW/dx is the energy deposition per unit channel length. The mass flow rate G may change as a result of gas admission or evacuation via the channel walls. In Eq. (2), the quantities U, P, ρ, R, and T are the velocity, pressure, density, gas constant, and temperature of the flow, respectively; R_0 is the universal gas constant; F is the channel cross section; and N_i, C_i, and Q_i are the volume concentrations (kmol/m^3), molar heat capacities, and enthalpies of formation of the components. The volume concentrations N_i are described by the transfer Eq. (2) including the term dN_i/dt representing a chemical source (or sink); the dN_i/dt values are determined for hydrocarbon reactions [4].

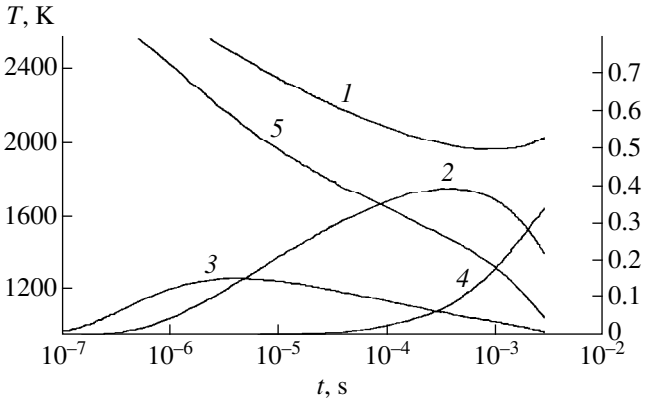

Fig. 2. The results of model calculations [1] showing time variation of the (*1*) temperature and the concentrations of (*2*) C_2H_2, (*3*) C_2H_4, (*4*) C, and (*5*) CH_4.

Figure 2 shows the results of model experiments [1] for a methane–hydrogen mixture at atmospheric pressure and an initial temperature of 3000 K. The mode was described using the above gasodynamic system and a system of kinetic relationships for the hydrocarbon components [4] supplemented by the reactions involving carbon [2]. In addition, we took into account the reactions of radicals [2] missing in the system considered in [4]. The rates of these additional reactions (Table 1) were somewhat modified (in comparison with those used in [2]).

As seen from Fig. 2, the carbon reactions must be taken into account because a decrease in the yield of acetylene is related with an increase in the amount of free carbon. A description based on a more complete system of kinetic equations reveals (in contrast to the

Table 1. Preexponential terms (A) and activation energies (E_a) for additional model reactions

Reaction	A, m^3/(kmol s)	E_a, kJ/mol
$C_2 + M \longrightarrow C + C + M$	$10^{12.6}$	651
$H + C + M \longrightarrow CH + M$	2×10^9	0
$C + C + M \longrightarrow C_2 + M$	2×10^7	0
$C_2H_2 \longrightarrow C + C + M$	9×10^5	125.6
$CH + CH \longrightarrow C_2H_2$	5×10^{10}	0
$CH_3 + CH_3 \longrightarrow C_2H_4 + H_2$	5×10^{10}	0

Table 2. The results of process calculations

Weight fractions of components	CH_4	C_2H_2	C_2H_4
P = 1 MPa Degree of conversion, 0.77; specific energy, 15.4 MJ/(kg C_2H_4)	0.200	0.168	0.518
P = 2 MPa Degree of conversion, 0.81; specific energy, 13.4 MJ/(kg C_2H_4)	0.165	0.124	0.595

simplified scheme [1, 2]) some new effects at pressures above the atmospheric pressure level. For 1–10 MPa, the calculations (for both super- and subsonic regimes) indicate that the yield of ethylene dominates over the yield of acetylene. Table 2 presents the results of process calculations for a reactor with an initial flow velocity of U_1 = 100 m/s and an energy deposition zone length of L = 0.2 m operating without an additional hydrogen supply. As seen, an increase in the pressure leads to a higher weight fraction of ethylene and a decrease in the specific energy consumption (per kilogram ethylene).

REFERENCES

1. *Kinetics and Thermodynamics of Chemical Reaction in Low- Temperature Plasma* (Nauka, Moscow, 1965).
2. *Processes and Apparatuses of Plasmachemical Technology* (Vishcha Shkola, Kiev, 1979).
3. Yu. P. Yampol'skiĭ, in *Elementary Reactions and Mechanism of Hydrocarbon Pyrolysis* (Khimiya, Moscow, 1990).
4. A. A. Borisov, G. I. Skachkov, and K. Ya. Troshin, Khim. Fiz. **18** (9), 45 (1999).
5. J. Weill, F. Chevron, C. Raimbault, *et al.*, Rev. Inst. Fr. Pet. **47** (2) (1992).
6. G. G. Chernyĭ, *Gas Dynamics* (Nauka, Moscow, 1988).

Translated by P. Pozdeev

Technical Physics Letters, Vol. 26, No. 12, 2000, pp. 1105–1107. Translated from Pis'ma v Zhurnal Tekhnicheskoĭ Fiziki, Vol. 26, No. 24, 2000, pp. 70–75.

An Experimental Investigation of the Physical Effects in a Dynamic Magnetic System

V. V. Roshchin and S. M. Godin

Institute of High Temperatures, Russian Academy of Sciences, Moscow, Russia;
e-mail: rochtchin@mail.ru
e-mail: smgodin@online.ru

Received June 16, 2000

Abstract—It is demonstrated that a magnetic system based on rare-earth magnets is capable of converting various forms of the energy, provided that certain critical operating regime is set. As the critical regime is attained, the experimental setup becomes energetically fully autonomous. This is accompanied by local variations in the total structure weight, a decrease in the surrounding air temperature, and the formation of concentric "magnetic walls" at a distance of up to 15 m from the experimental setup. *© 2000 MAIK "Nauka/Interperiodica".*

Introduction. We have experimentally studied the physical effects in a system based on rotating permanent magnets [1]. Below, we describe the technology of manufacture; assembly; and the results of testing this experimental setup, which is referred to as the converter.

Technological description. The converter comprises an immobile stator and a rotor moving around the stator and carrying fixed magnetic rollers. The magnetic system of the working body of the converter has a diameter of about 1 m. The stator and magnetic rollers were manufactured from separate magnetized segments made of rare-earth magnets (REMs) with a residual magnetization of 0.85 T, a coercive force of $[Hc] \sim 600$ kA/m, and a specific magnetic energy of $[W] \sim 150$ J/m^3. The segments were magnetized by a conventional method based on a discharge of a capacitor bank through an inductor coil. Then the magnetized segments were assembled and glued together in a special mounting stage, which provided for the necessary tolerance in positioning the segments and for the removal of magnetic energy. Using this mounting stage, it was possible to glue the elements into the common unit. The stator incorporated REMs with a total weight of 110 kg and the rollers contained 115 kg of the same REM material.

The magnetic system elements were assembled into a single structure on a special platform made of nonmagnetic structural alloys. The platform construction was provided with springs and shock absorbers and allowed the converter setup to move in the vertical direction on three slides. The motion was monitored by an inductive transducer, which allowed changes in the platform weight to be determined in the course of the experiment. The total weight of the platform with the magnetic system in the initial state was 350 kg.

Description of observed effects. The converter was installed in a 2.5-m-high laboratory room using three concrete supports on a ground level. In additional to the ordinary steel-reinforced concrete ceiling blocks, the converter environment featured a usual electrodynamic generator and an electric motor, with a total iron weight of a several dozen kilograms (only these parts could, in principle, introduce distortions into the electromagnetic field pattern observed).

The converter was set to operation by the electric motor. The motor speed was gradually increased until the amperemeter connected in the motor circuit showed zero consumed current and the current direction reversal. This state corresponded to a rotor speed of approximately 550 rpm, but the motion transducer began to indicate a change in the platform weight already at 200 rpm. Then the electric motor was disconnected using an electromagnetic overrunning clutch, and a usual electrodynamic generator was connected instead to the main shaft of the converter via another electromagnetic clutch. On attaining the critical regime (~550 rpm), the rotor exhibited a sharp increase in the rotation speed; this was accompanied by a slow-down in the rate of the current weight variation. At this instant, the first 1 kW load was connected to the system. Immediately upon this connection, the rotation speed began to decrease, while the ΔG value kept increasing, and so on, as depicted in figure.

The system weight variations depend both on the power consumed by the active load (the load consisted of ten ordinary 1-kW heating elements) and on the polarization voltage applied. For the maximum consumed power (7 kW), a change in the total platform weight reached 35% of the initial value in the immobile state (350 kg), which corresponded to 50% of the pure weight of the working body of the converter. An increase in the load power above 7 kW led to a gradual

1063-7850/00/2612-1105$20.00

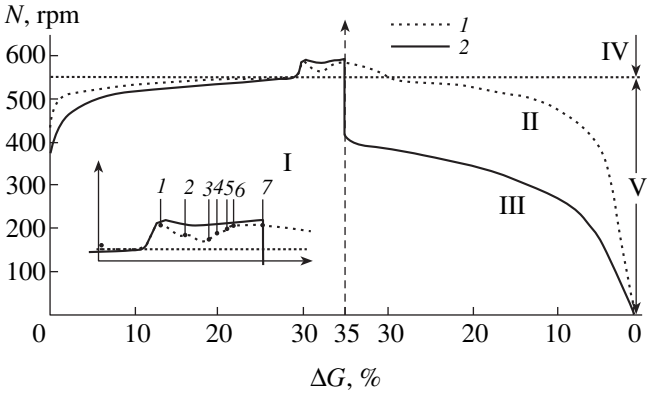

A diagram illustrating various operation regimes of the magnetogravitational converter showing (I) load power (kW) and system weight variation; (II) 7-kW load (high voltage off); (III) 7-kW load (high voltage on); (IV) supercritical regime; (V) subcritical regime (*1*, high voltage off; *2*, high voltage on).

decrease in the rotor speed and, eventually, to the system going out of the self-generation regime and the rotor speed decreasing until the full stop.

The platform weight could be controlled by applying a high-voltage signal to the cellular ring electrodes situated 10 mm above the external roller surface. Upon applying a 20-kV signal (negative polarity on the electrodes), an increase in the load power consumption above 6 kW did not affect the ΔG value even when the rotor speed decreased down to 400 rpm. This was equivalent to "prolongation" of the effect and was accompanied by phenomena of the "remanent induction" type with respect to ΔG. The converter operation in various experimental regimes is illustrated in the figure.

The effect of the system weight variation is reversible with respect to the direction of rotor motion and exhibits certain hysteresis. For the clockwise rotation, the critical regime is observed in the region of 550 rpm and is accompanied by development of the force acting against the gravity vector. For the counterclockwise rotation, the onset of the critical regime is observed at approximately 600 rpm and the extra force coincides in direction with the gravity vector. The onset of the critical regime exhibited a scatter within 50–60 rpm. It should be noted that some other critical resonance regimes may exist which correspond to higher rotor speeds and markedly greater useful load levels. Proceeding from the general theoretical considerations, the output mechanical energy must nonlinearly depend on the internal parameters of the converter magnetic system and the rotor speed, so that the observed effects are likely to be far from optimum. Establishing the maximum output power, maximum weight variation, and the converter energy resource is of considerable theoretical and practical interest.

Besides the phenomena described above, a number of other interesting effects were observed in the system studied. In particular, the converter operation in the dark is accompanied by a corona discharge with a pinkish blue light emission and by the ozone production. The ionization cloud is formed around the stator and rotor, acquiring a toroidal shape. The general corona discharge background is superimposed with a wavy pattern corresponding to the surface of rollers: the zones of increased emission intensity are distributed along the roller height in a manner similar to that observed for the high-voltage microwave induction energy storage in the prebreakdown state. These zones appeared yellowish white, but the emission was not accompanied by sounds characteristic of the arc discharge. We also did not observe any visible erosive damage on the stator and rotor surfaces.

One more effect which was never reported previously is the appearance of vertical "magnetic walls" surrounding the setup. We have detected and measured an anomalous constant magnetic field around the converter. The measurements revealed zones of increased magnetic field strength on the order of 0.05 T arranged coaxially relative to the system center. The direction of the magnetic field vector on the "walls" coincides with that in the rollers. The structure of these magnetic zones resembles the pattern of circular waves on the water surface. No anomalous field is detected by a mobile magnetometer, employing the Hall effect transducer, in the areas between zones. The layers of increased magnetic field strength are propagating with virtually no attenuation to a distance of 15 m from the converter center and then rapidly decayed at the boundary of this 15-m area. Each layer zone is 5–8 cm thick and exhibits sharp boundaries. The layers are spaced by 50–60 cm, the spacing slightly increasing with the distance from the converter center. A stable pattern was also observed at a height of 5 m above the setup (the measurements were conducted in a second-floor room above the laboratory; no tests were performed on a higher level).

Another interesting phenomenon consists in an anomalous temperature drop in the immediate vicinity of the converter. At a general room temperature level in the laboratory +22°C (±2°C), the temperature at the converter surface was 6–8°C lower. Similar temperature variations were detected in the vertical magnetic "walls." The temperature changes in the walls were detected by an ordinary alcohol thermometer with a reading set time of 1.5 min. The temperature variations in the magnetic "walls" can be even sensed by the human body: a hand placed inside the "wall" immediately feels cold. The same pattern was observed at a height of 5 m above the setup in a second-floor room above the laboratory (despite the steel-reinforced concrete blocks separating the rooms).

Discussion of results. All the experimental results described above are very unusual and need some theoretical rationalization. Unfortunately, attempts at interpreting the obtained results within the framework of the

existing physical theories showed that no one of these models can explain the whole set of experimental data.

Recently, Dyatlov [2] attempted to combine the concepts of electricity and gravity by introducing the so-called electrogravitation and magnetic-spin coefficients into the Heaviside gravity equations and the Maxwell field equations. This provides for a relationship between the gravitational and electrical components, as well as between the magnetic and rotational components in a given medium. The assumptions are built around a special model of inhomogeneous physical vacuum, called the vacuum domain model [2]. It is suggested that the extra relationships are absent outside the vacuum domain. Although it is difficult to imagine a long-living vacuum domain, the proposed model provides for a satisfactory explanation (at least on a qualitative phenomenological level) for the appearance of emission, the system weight variations, and the conversion of energy taken from the surrounding medium into the rotational mechanical moment of the rollers. Unfortunately, the theory cannot provide a physical pattern of the observed phenomena.

Conclusion. At present, the works on a developed variant of the converter are in progress at the Glushko "NPE Énergomash" stock company (Moscow). This setup would allow a deeper insight into the physics of observed phenomena. Another aim is the creation of commercial samples for various practical applications.

REFERENCES

1. J. A. Thomas, Jr., in *ANTI-GRAVITY: The Dream Made Reality: The Story of John R. R. Searl* (Direct International Science Consortium, London, 1994), Vol. VI, Iss. 2.
2. V. L. Dyatlov, *Polarization Model Heterogeneous Physical Vacuum* (Inst. Mat., Novosibirsk, 1998).

Translated by P. Pozdeev

Technical Physics Letters, Vol. 26, No. 12, 2000, pp. 1108–1109. Translated from Pis'ma v Zhurnal Tekhnicheskoĭ Fiziki, Vol. 26, No. 24, 2000, pp. 76–79.

Effect of the Pressure on the Type of Mixing in a Three-Component Gas Mixture Containing a Component Possessing the Properties of a Real Gas

Yu. I. Zhavrin, V. N. Kosov, D. U. Kul'zhanov, and K. K. Karataeva

Institute of Experimental and Theoretical Physics, Kazakh State University, Almaty, Kazakhstan

Received August 1, 2000

Abstract—Evolution of the mass transfer regime in a three-component gas mixture in the course of transition from molecular diffusion to the diffusion instability development and the convective mixing driven by the partial pressure difference was experimentally studied. It is demonstrated that the mixtures containing a component possessing the properties of a real gas may exhibit various types of mixing and the corresponding transition regimes. *© 2000 MAIK "Nauka/Interperiodica".*

Experimental investigations of the process of isothermal molecular diffusion in three-component gas mixtures showed that instability of the mechanical equilibrium in such systems may be observed for various thermodynamic parameters, geometric characteristics of the mass transfer channel, and directions of the total density gradient [1–3]. However, some special features in these experiments allowed a change in the mass transfer regime from molecular diffusion to concentration convection to be studied only for a preset direction of the total density gradient in the gas mixture. This circumstance made it impossible to follow the sequence of transitions from molecular diffusion to diffusion instability and gravitational concentration convection in a particular system depending on a single variable parameter.

Below, we report on the results of experimental investigation of the evolution of some characteristic features of the mass transfer regime in three-component gas mixtures in the course of transitions from molecular diffusion to the diffusion instability and the ordinary convective mixing as a result of the partial pressure difference. The conditions for these transitions can be provided if one of the gas mixture components exhibits pressure-dependent variations in the partial density according to the real gas laws. For example, when a binary mixture with the composition 0.4163 H_2 + 0.5837 N_2O (molar fractions) diffuses into nitrogen at T = 298 K and a pressure close to the atmospheric pressure, the density of the binary mixture is lower than that of nitrogen. As the pressure increases, the two densities exhibit leveling (at $P \sim 1.5$ MPa) and then the gas mixture density exceeds that of the nitrogen.

The mass transfer experiments were conducted in a two-compartment diffusion setup comprising the upper and lower vessels with equal volumes $V_1 = V_2 = 55$ cm^3 and a diffusion channel with a diameter of 4.0 mm and a length of 70.0 mm. The temperature in all experiments was 298 K and the diffusion time was 30 min. The experimental procedure was analogous to that described in [1–3].

The procedure was essentially as follows. The binary gas mixture 0.4163 H_2 + 0.5837 N_2O was always charged into the upper compartment (irrespective of the pressure-dependent density) and nitrogen was admitted to the lower compartment. Then the compartments were connected and the process of gas mixing in the system was studied at various pressures. The figure shows the experimental data on the concentrations of hydrogen and nitrous oxide in the system. The third component (nitrogen) concentration can be calculated using the balance condition $\sum_{i=1}^{3} c_i = 1$, where c_i is the molar fraction of the ith component.

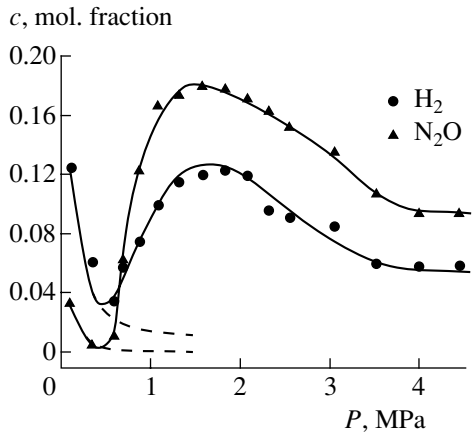

The amounts of hydrogen and nitrous oxide passing from upper to lower vessel in various mixing regimes depending on the pressure. Points present the experimental data, solid curves show the results of approximation by model polynomials, and dashed curves are calculated using the Stephan–Maxwell equations assuming stable diffusion.

1063-7850/00/2612-1108$20.00 © 2000 MAIK "Nauka/Interperiodica"

An analysis of the experimental data allowed the characteristic transition regimes to be revealed. In the interval of pressures from atmospheric (~0.093 MPa) to about 0.4 MPa, behavior of the component concentrations is characteristic of the molecular diffusion. This is confirmed by coincidence of the experimental data with the results of calculations according to the Stephan–Maxwell equations [4]. The further increase in the pressure leads to the development of instability in the mechanical equilibrium of the gas mixture under the negative density gradient conditions. The change from molecular diffusion to the diffusion instability is related to a transition from the molecular mechanism of mass transfer between the mixture components to the structurized convective flows that can be predicted within the framework of the model proposed in [5]. As the pressure keeps growing, the system exhibits a pattern of developed convective flows with a clearly pronounced effect of the heavy component separation from hydrogen, a highly mobile gas [6]. Here, the experimental values of the component concentrations markedly exceed those calculated using the Stephan–Maxwell equations assuming stable diffusion. At a pressure of about 1.5 MPa, the density of the binary mixture becomes equal to that of the pure component (nitrogen) and the intensity of mixing reaches a maximum. The rate of the component mass transfer by molecular diffusion is lower by more than one order of magnitude as compared to the rate of the convective transfer.

The subsequent increase in the pressure from 1.5 to 3.0 MPa leads to a change in the sign of the density gradient, which is accompanied by competition of the convective flows caused both by the diffusion instability and by the traditional convective mixing. Above 3.0 MPa, the mixture is transferred as a whole, as can be judged from the final ratio of the hydrogen and nitrous oxide concentrations, which is approximately equal to the initial value. In the regime of convective mixing, a reason for the absence of component separation is that a nonideal behavior of the binary mixture components (nitrous oxide) results in creating a density gradient such that a contribution due to the diffusion instability is small as compared to the transfer due to the gravitational concentration convection.

Thus, the results of our investigation show that three-component gas mixtures containing a component possessing the properties of a real gas may exhibit various types of mixing and the corresponding transition regimes depending on a thermodynamic parameter such as the pressure.

REFERENCES

1. Yu. I. Zhavrin, N. D. Kosov, S. M. Belov, and S. B. Tarasov, Zh. Tekh. Fiz. **54** (5), 943 (1984) [Sov. Phys. Tech. Phys. **29**, 561 (1984)].
2. Yu. I. Zhavrin and V. N. Kosov, Teplofiz. Aéromekh. **2** (2), 145 (1995).
3. Yu. I. Zhavrin and V. N. Kosov, Pis'ma Zh. Tekh. Fiz. **19** (10), 18 (1993) [Tech. Phys. Lett. **19**, 301 (1993)].
4. Yu. I. Zhavrin, N. D. Kosov, V. N. Kosov, *et al.*, Available from KazgosINTI No. 6239 (Kazakh. Univ., Almaty, 1995).
5. V. N. Kosov, V. D. Seleznev, and Yu. I. Zhavrin, Inzh.-Fiz. Zh. **73** (2), 313 (2000).
6. V. N. Kosov, V. D. Seleznev, and Yu. I. Zhavrin, Zh. Tekh. Fiz. **68** (5), 14 (1998) [Tech. Phys. **43**, 488 (1998)].

Translated by P. Pozdeev

Technical Physics Letters, Vol. 26, No. 12, 2000, pp. 1110–1113. Translated from Pis'ma v Zhurnal Tekhnicheskoĭ Fiziki, Vol. 26, No. 24, 2000, pp. 80–88.

Vacant Electron State Manifestations in the Electron-Beam-Induced Current Spectra of Macromolecular Films

S. A. Komolov, N. B. Gerasimova, A. G. Sidorenko, and Yu. G. Alyaev

Institute of Physics, St. Petersburg State University, St. Petersburg, Russia

Received June 7, 2000

Abstract—The vacuum-deposited films of corbatin (CRB) and perylene tetracarboxy dianhydride (PTCDA) were studied *in situ* by method of total electron-beam-induced current (EBIC) spectroscopy. The results are interpreted within the framework of the model of vacant electron states (VES) above the energy level of vacuum. For PTCDA samples, the VES density determined from the EBIC measurements shows a good agreement with the available NEXAFS data. For CRB films, the VES density above the vacuum level is reported for the first time. *© 2000 MAIK "Nauka/Interperiodica".*

Introduction. In the past decades, there was increasing interest of researchers in the study of the electron properties of layered structures, which was mostly related to the development of microelectronics. A special effort was devoted to searching for and characterizing of new materials offering an alternative to the existing structures based on inorganic semiconductors. Thin films of organic macromolecules are among the materials showing considerable potential for the application in electronics. This is due to fact that some of these films possess semiconductor properties. In addition, the properties of organic materials can be modified in a controlled manner both during the synthesis of macromolecules and in the course of subsequent technological processes. The good prospects for the macromolecular organic layer structures become more evident from the standpoint of miniaturization of the electronic devices and the development of molecular electronics.

Below, we report on the results of investigation of the properties of thin organic films prepared by vacuum deposition of corbatin (CRB) and perylene tetracarboxy dianhydride (PTCDA) onto (0001)ZnO single crystal substrates. Both organic compounds studied possess semiconductor properties and are stable under high vacuum conditions. PTCDA, which is capable of forming ordered layers [1, 2], is used for the fabrication of light-emitting devices; CRB was also reported to exhibit important effects such as photo emf [3] and photoconductivity [4, 5].

The experiments were performed using the total electron-beam-induced current (EBIC) spectroscopy technique. This method, based on a nondestructive monitoring of the sample surface with an electron beam at an electron energy of 0–30 eV and a beam current on the order of 10 nA, provides information on the electron density of states and their dispersion, as well as on the surface potential [6].

Experimental. The sample films were deposited and studied *in situ* in an ultrahigh vacuum (UHV) system evacuated to a residual working pressure of 5×10^{-8} Pa). The system was equipped with various secondary-electron surface analytical facilities. A four-grid electron energy analyzer allowed (besides the EBIC measurements) the sample surface composition to be studied by Auger electron spectroscopy (AES). In the EBIC mode, a parallel electron beam was incident onto the sample film surface and the total current $I(E)$ in the sample circuit was measured as function of the electron beam energy (provided that both secondary and reflected electrons were completely separated) [6].

The probing electron beam energy was varied from 0 to 30 eV. The fine structure of the EBIC spectra was revealed by measuring the first derivative of the total current with respect to energy [$S(E) = dI/dE$], which was provided by using a lock-in detector and modulating the primary electron beam energy (modulation frequency, 1600 Hz; modulation amplitude, 0.1 eV). The electron beam, incident along the normal to the sample surface, was focused to a spot size of 0.2–0.4 mm. The primary electron peak in the EBIC spectrum corresponds to the vacuum energy level E_{vac} of the surface studied. In the course of the sample material processing, this peak may shift in response to the surface work function variations.

The fine structure of the EBIC spectra is determined by the energy dependence of electron reflection coefficient, the latter representing a sum of the coefficients of elastic and inelastic reflection. For small primary electron energies (E < 20–25 eV), the elastic component can be assumed to dominate [6–8]. The energy dependence of the elastic reflection coefficient is closely

related to the energy band structure in the interval of energies corresponding to that of the primary electrons [6–8]. In the class of molecular solids, to which the substances studied belong [9], the elastic reflection coefficient varies predominantly by a mechanism depending on the density of vacant electron states (VES) above the vacuum level. This density corresponds to the energy of primary electrons exhibiting stronger refection in the region of forbidden bands and weaker reflection and, hence, a greater current in the sample circuit in the vicinity of allowed states.

The peaks in the EBIC spectrum registered in the $S(E) = dI/dE$ mode correspond to energy positions of the VES bands, while the maxima of $(-dS/dE)$ indicate the energy positions of the VES density maxima. Thus, the derivative of the EBIC spectrum (taken with the opposite sign) is better suited for comparison to the VES density values calculated theoretically or determined by other independent methods. Owing to the weak intermolecular interaction, the spectrum of electron states measured in solids differs but little from the corresponding molecular spectrum, while the surface electron structure is virtually identical to the bulk structure.

Prior to the sample film deposition, the ZnO substrate surface was cleaned by heating in high vacuum to 1000 K with short-time flashing to 1100 K. The surface cleanness was checked by the AES spectra, which revealed only the signals from zinc and oxygen. The signal from carbon was below the level of spectrometer sensitivity, so that the concentration of carbon atoms on the surface was less than 1/100 of that for the other components. The EBIC spectrum of the ZnO substrate corresponded to that reported in [10] for the (0001) face of a zinc oxide single crystal.

The films were deposited by thermally evaporating the PTCDA and CRB powers. The structural formula of these compounds are depicted in Fig. 1. Note that the main structural component in both molecules is the aromatic carbon nucleus, which determines the general character of the valence and conduction band structure of the compounds studied. The initial substances were evaporated from thoroughly outgassed Knudsen cells. The evaporation temperatures were 600 K (PTCDA) and 670 K (CRB).

The EBIC spectra recorded in the course of the film growth reflected gradual disappearance of the features related to the substrate and the build-up of those corresponding to the film structure. In the initial deposition stage, no additional features were observed that could distinguish the electron structure of the very first layer from that of the bulk solid compound. This is indicative of the absence of chemical reactions between ZnO substrate and deposited substances. Simultaneously, the work function variation was monitored by measuring the position of the primary electron peak. The work function gradually increased with the EBIC spectrum formation in the case of PTCDA and decreased in CRB. The deposition process was terminated when the EBIC spectra ceased to change.

Figure 2 shows the typical EBIC spectra of CRB (curve *1*) and PTCDA (curve *2*). The main peaks in the spectrum of CRB are observed at 0.8, 2.5, 5.1, 7.3, and 8.6 eV, while the PTCDA samples are characterized by the peaks at 1.4, 5.0, 9.6, and 14.3 eV. The results obtained for PTCDA agree well with the data reported in [11] for the films deposited onto passivated silicon substrates.

Discussion of results. As noted above, the principal mechanism responsible for the EBIC spectrum formation in molecular solids consists in variation of the elastic reflection coefficient depending on the density of VES situated above the vacuum level. The EBIC spectra immediately reveal the total density of vacant electron states reflecting the contributions both from various elements entering into the structure of molecules and from the molecular orbitals of various types (for macromolecules, predominantly of the π^* and σ^* orbitals).

A similar mechanism of the EBIC spectrum formation was reported in graphite single crystals [12, 13], where the VES peaks due to the π^* and σ^* orbitals were resolved and it was found that the former orbitals dominate in the energy range below 6 eV, while the latter are

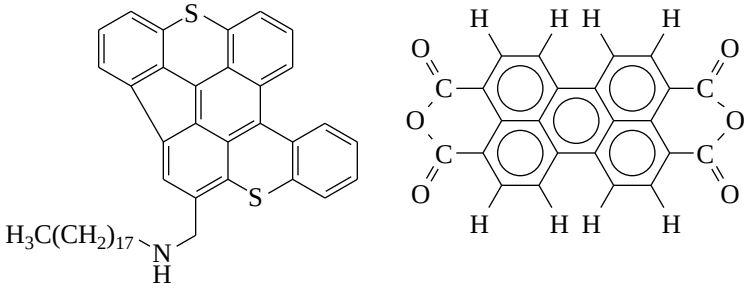

1 *2*

Fig. 1. Structural formulas of the organic compounds studied: (*1*) CRB; (*2*) PTCDA.

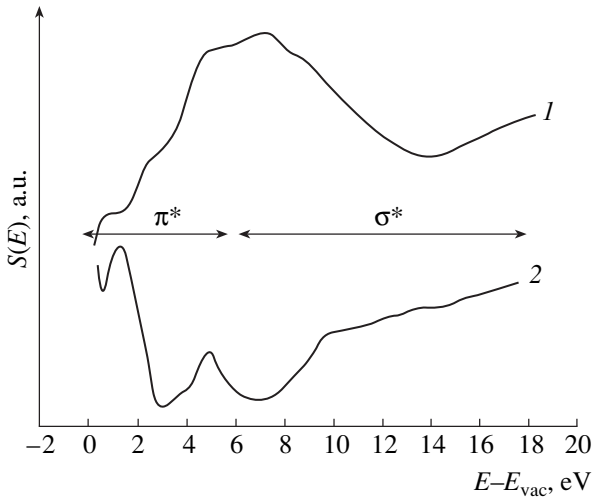

Fig. 2. The EBIC spectra of (*1*) CRB and (*2*) PTCDA. Errors indicate the probable energy intervals of predominant contributions due to the π* and σ* orbitals.

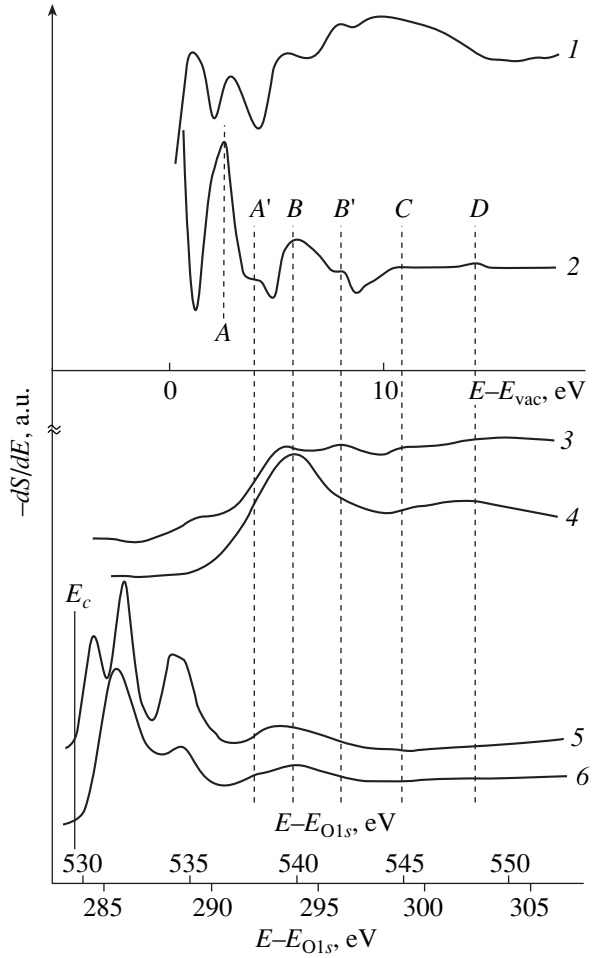

Fig. 3. Identification of the VES density peaks above the vacuum level for CRB and PTCDA molecules using the EBIC spectra of (*1*) CRT and (*2*) PTCDA and the NEXAFS (*3*, *5*) C1*s* and (*4*, *6*) O1*s* spectra of PTCDA measured for (*3*, *4*) normal and (*5*, *6*) glancing incidence of the primary X-ray beam. The EBIC and NEXAFS energy axes are matched as described in the text.

dominating at higher energies (these intervals are indicated by arrows in Fig. 2). Taking into account that the base fragments of molecules studied in this work are represented by the aromatic carbon nuclei analogous to layer fragments in the graphite structure, the above boundary energy value dividing the VES levels between π* and σ* states can be also used as a rough estimate in interpreting the EBIC spectra of PTCDA and CRB.

In order to determine the positions of maxima in the VES density structure above the vacuum level, the EBIC spectrum should be differentiated and the derivative taken with the opposite sign. The results of this processing are presented in Fig. 3. As seen, the VES density peaks for PTCDA (curve *2*) are observed at 2.5, 4.3, 5.8, 8.1, 10.6, and 14.4 eV (peaks *A*, *A*', *B*, *B*', *C*, and *D*, respectively), while CRB (curve *1*) is characterized by the VES density peaks at 1.0, 2.8, 5.5, 7.9, and 9.6 eV.

Figure 3 (curves *3*–*6*) also presents data on the nonextended X-ray absorption fine structure (NEXAFS) of PTCDA taken from [14], which provides additional information on the VES density. As is known from the NEXAFS spectroscopy principles, the normally incident X-ray beam most probably excites the electron transitions into σ* states represented by curves *3* and *4* [14]. It should be noted that the NEXAFS exhibits a more developed pattern for excitation of the C1*s* level (curve *3*) than for the O1*s* level (curve *4*), this fact being indicative of a difference in the local VES density in the vicinity of carbon and oxygen atoms. The curves *5* and *6* measured at a glancing incidence of the primary X-ray beam mostly reflect the structure of the π* states localized in the range of lower energies [14].

In order to compare the EBIC spectra measured in this work to the NEXAFS data, it was necessary to match the energy axes. For this purpose, we determined the position of the conduction band bottom by the onset of the X-ray absorption (E_c in Fig. 3). As is known, the vacuum level (the origin on the EBIC energy scale) differs from this level by a value equal to the electron affinity χ (4.1 eV for PTCDA [9, 15]). As seen from Fig. 3, the matched energy axes provide for a good correspondence between the EBIC ad NEXAFS curves in both positions and shapes of their characteristic features except for peaks A and A'. The comparison shows that the features denoted by B, B', C, and C' refer to the σ* states. The A and A' peaks probably correspond to the higher π* states that are shifted downward in the NEXAFS spectra. This can be explained by influence of the hole formed on the 1*s* level (from which the electron was excited) upon the energy positions of orbitals [14, 16].

As follows from the comparison of EBIC and NEXAFS data in Fig. 3, the former spectrum reflects the total VES density, whereas the latter exhibits certain limitations related to the selection rules. This circumstance probably also accounts for a difference observed

in the NEXAFS spectra for electrons excited from the 1*s* levels of various elements. Owing to the fact that carbon atoms in the PTCDA molecule occur in various nonequivalent states, the electrons may exhibit transitions to a greater number of orbitals in the conduction band. This fact explains the more developed structure of the C1*s* NEXAFS spectra. At the same time, all the peaks observed in the C1*s* spectra are also present in the O1*s* spectra, which is indicative of a hybridization of the orbitals of oxygen and carbon atoms or, in other words, of a delocalized character of the electron states in the conduction band.

As for CRB, we may suggest that the first two low-energy peaks are of the π^* nature, while the remaining three peaks possess the σ^* character. This hypothesis is based on the general considerations, concerning energy positions of the VES density maxima in compounds with the structures built around the nuclei of aromatic carbon rings, which proved to be valid in the case of PTCDA. We also took into account the peak shapes: the π^* orbitals correspond to narrower, more clearly pronounced features than the σ^* orbitals.

Conclusion. The results of the *in situ* investigation of the electron structure of PTCDA and CRB films by the method of electron-beam-induced current showed that features in these spectra reflect the energy dependence of the density of vacant electron states above the vacuum level. The VES density peaks were observed at the following energies: 2.5, 5.8, 10.6, 14.4 eV (PTCDA) and 1.0, 2.8, 5.5, 7.9, 9.6 eV (CRB). The peaks are divided into two groups corresponding to orbitals of the π^* and σ^* nature.

A comparison of the EBIC spectrum of PTCDA to the NEXAFS spectrum of this compound showed good coincidence of the spectral features. It was demonstrated that the EBIC technique provides information on the total VES density above the vacuum level, including contributions both from various elements entering into the composition of molecules and from the electron orbitals of various types (for macromolecules, predominantly of the π^* and σ^* orbitals). Hypotheses concerning the possible reasons for some distinctions between the two methods were formulated.

Acknowledgments. The authors are grateful to D.R.T. Zahn for kindly providing a PTCDA sample for this investigation and to V.A. Novolodskiĭ for fruitful discussions of results.

The work was supported by the Russian Foundation for Basic Research (project no. 99-03-33427) and by the Federal Program "Surface Atomic Structures" (project no. 4.3.99).

REFERENCES

1. U. Zimmermann, G. Shnitzler, N. Karl, *et al.*, Thin Solid Films **175**, 85 (1989).
2. K. Glöcker, C. Seider, A. Soukopp, *et al.*, Surf. Sci. **405**, 1 (1998).
3. K. Schaumburg, S. A. Komolov, N. B. Gerasimova, *et al.*, Thin Solid Films **299**, 161 (1997).
4. A. Komolov, K. Schaumburg, and N. Harrit, Thin Solid Films **299**, 159 (1997).
5. A. Komolov, K. Schaumburg, and V. Monakhov, Phys. Low-Dimens. Semicond. Struct. **1-2**, 135 (1999).
6. S. A. Komolov, in *Integral Secondary-Electron Spectroscopy of the Surface* (Leningr. Gos. Univ., Leningrad, 1986).
7. S. A. Komolov and V. N. Strocov, Phys. Status Solidi B **167**, 605 (1991).
8. V. N. Strocov and H. I. Stranberg, Phys. Rev. B **52**, 8759 (1995).
9. H. Ishii, K. Sugiyama, E. Ito, *et al.*, Adv. Mater. **11** (8), 605 (1999).
10. P. J. Möller, S. A. Komolov, and E. F. Lazneva, J. Phys.: Condens. Matter **11**, 9581 (1999).
11. A. O. Morozov, T. U. Kampen, and D. R. T. Zahn, Surf. Sci. **446**, 193 (2000).
12. A. Dittmar-Wituski, M. Naparty, and J. Skonieczny, J. Phys. C **18**, 2563 (1985).
13. I. Shäfer, M. Shlüter, and M. Skibowski, Phys. Rev. B **35** (14), 7663 (1987).
14. J. Taborski, P. Väterlein, H. Dietz, *et al.*, J. Electron Spectrosc. Relat. Phenom. **75**, 129 (1995).
15. S. R. Forrest, M. L. Kaplan, and P. H. Schmidt, J. Appl. Phys. **55**, 1492 (1984).
16. R. A. Rosenberg, P. J. Love, and V. Rehn, Phys. Rev. B **33** (6), 4034 (1986).

Translated by P. Pozdeev

Technical Physics Letters, Vol. 26, No. 12, 2000, pp. 1114–1116. Translated from Pis'ma v Zhurnal Tekhnicheskoĭ Fiziki, Vol. 26, No. 24, 2000, pp. 89–94.

Electron Beam Formation in an Open Discharge

A. R. Sorokin

Institute of Semiconductor Physics, Siberian Division, Russian Academy of Sciences, 630090 Novosibirsk, Russia

Received July 5, 2000

Abstract—The results of calculations reported for the first time indicate that the electron emission from a cathode, which is necessary to explain the main properties of an open discharge, is stimulated by the cathode bombardment by fast atoms rather than by photons (as was believed for a long time). The calculations are based on the results of measurements of the electric field strength in the discharge region and of the coefficient of electron emission from a cathode bombarded by helium atoms and ions. It is also demonstrated that the efficiency of the gas ionization by fast atom bombardment is significant at a voltage of several keV and becomes comparable with the electron-impact ionization in the anode plasma at a voltage equal to a few tens of keV. © *2000 MAIK "Nauka/Interperiodica".*

1. It was believed for a long time [1] that an open discharge (a kind of the confined discharge) is initiated and sustained by photoemission from the cathode, which is related to the radiative de-excitation of atoms excited in the drift space by an electron beam penetrating into this region from the discharge gap via the anode grid.

However, subsequent experiments [2–4] demonstrated that the photoelectron-stimulated open discharge mechanism contradicts the experimental data. Indeed, effects such as the current build-up depending on the gap width d [4] or the field sagging in the grid holes [3] cannot be explained within the framework of the photoelectron-stimulated discharge model. These effects are obviously related to ionization processes in the discharge. Moreover, typical oscillograms indicate that the beam current begins to drop under conditions that are the most favorable for the beam-induced excitation of atoms, that is, when the efficiency of photoemission could be expected to grow sharply [2]. Neither these arguments nor other similar considerations were taken into account in some communications published later [5, 6].

Apparently, this situation is explained by the absence of calculations that would directly confirm that some mechanism other than photoelectron may account for the open discharge formation. The main factor hindering such calculations was the lack of reliable measurements of the electric field strength in the discharge gap.

The purpose of this study was to solve this task based on the results of measurements of the electric field distribution reported in [5] and the data on the coefficients of electron emission from a cathode bombarded by helium ions and atoms [7].

2. Consider the ions generated in the middle of a weak-field region in the gap (Fig. 1), for example, at $x/d = 0.65$. The ions move toward the cathode, exhibiting multiple recharge events ($\sigma_{ct} \sim 1.2 \times 10^{-15}$ cm^2 [7]), and participate in the cathode bombardment together with the fast atoms formed in these events. For the conditions described by curve *1* (Fig. 1), the total electron emission coefficient calculated using the data from [7] is $\gamma = \gamma_a + \gamma_{aw} + \gamma_+ = 6.7$, where $\gamma_a = 6$, $\gamma_{aw} = 0.4$ is the contribution due to fast atoms generated within and behind the cathode fall (CF) region, and $\gamma_+ = 0.3$ is the contribution due to the primary ion. The efficiency of the electron beam production is $\xi = \gamma(\gamma + 1)^{-1} = 0.87$ (for curve *2*, $\xi = 0.84$).

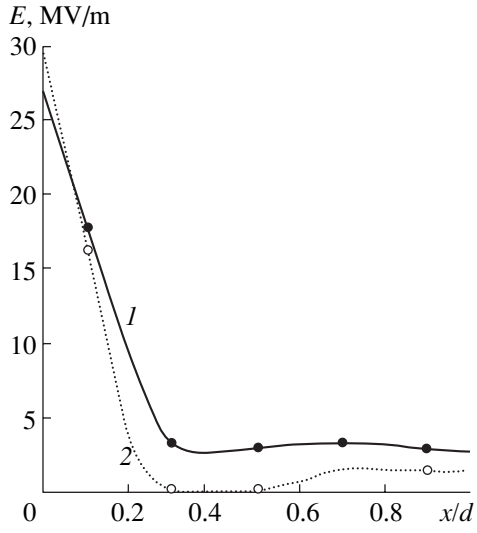

Fig. 1. Electric field strength distribution in a discharge gap with $d = 1.2$ mm [5]: (*1*) at a maximum current $j = 45$ A/cm^2 ($U = 7.8$ kV); (*2*) in the middle of the current fall ($U = 5.1$ kV). Helium pressure $p = 20.5$ Torr; current pulse duration ~50 ns.

1063-7850/00/2612-1114$20.00 © 2000 MAIK "Nauka/Interperiodica"

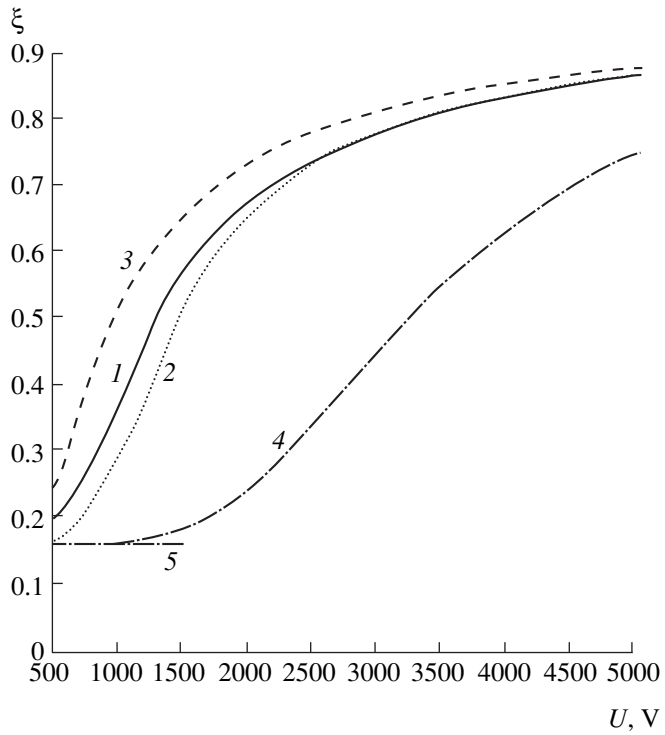

Fig. 2. Plots of the electron beam production efficiency ξ vs. the voltage U across the discharge gap: (*1*) quasi-stationary stage of the anomalous discharge; (*2–4*) a discharge with weakly distorted electric field in the gap, $pd = pl_m$ (*2*); $0.5pl_m$ (*3*); $3pl_m$ (*4*); $3pl_m$ (for $\gamma_a = 0$) (*5*).

Thus, bombardment of the cathode with heavy particles can provide for a high efficiency of the electron beam production under typical open discharge conditions. It should be emphasized that the above calculation employed only the experimental data.

In order to compare the obtained ξ value to the quantity used to characterize the electron beam production efficiency in experiment $\eta = I_c(I_c + I_a)^{-1}$ (where I_c and I_a are the collector and anode currents), we must take into account that the beam is partly trapped by the anode grid. Depending on the degree of discharge confinement, a part of the beam passing by the grid characterized by the geometric transparency factor μ may vary from 1 to μ [4] (in a strongly confined discharge, the current on the grid connector is zero).

In a strongly anomalous discharge, the value of l_c (the cathode fall length) tends to the limit $l_m = 0.37(pl_c)_n p^{-1}$, where $(pl_c)_n$ corresponds to the normal glow discharge. The limiting current conditions are always reached in a typical open discharge. However, even in the quasi-stationary open discharge sages, the confinement is completely removed for the d values markedly greater than l_m (e.g., for $d > 2l_m$ [4, Fig. 4]), after which η becomes equal to μξ. Note that the measurements of l_c under the conditions of $d \sim l_m$ may lead to understated values $l_c < l_m$ [4] because of a strong field sagging in the grid holes. Apparently, a reasonable criterion for the completely removed discharge confinement ($l_c = l_m$) is provided by correspondence of the discharge voltage U to the anomalous discharge parameter j/p^2 [8].

The discharge confinement is not removed under the conditions characterized by Fig. 1, where $l_c = 0.36$ mm > $l_m = 0.23$ mm and the current observed even on the decay branch of U (curve *2*) is only about one-sixth of the value necessary for the anomalous discharge. Therefore, we have to conclude that η falls within the interval from μξ to ξ, that is, from 0.65 to 0.87 (μ = 0.75). Thus, the average value is $\eta \approx 0.75 = \mu$, which is usually achieved under the optimum open discharge conditions.

3. Using the data from [7], we may derive sufficiently simple formulas for γ and, hence, for ξ in a more general case. For example, considering the case of the anomalous discharge ($l_c = l_m$), assuming that all the voltage drops across the CF region with a linear field distribution falling to zero in the direction outward the cathode, and taking U = 1.5–5 kV, we obtain for the total emission coefficient $\gamma = \sum_{i=1}^{N=18} \gamma_{ai} + \gamma_+ = -0.84 + 1.43 \times 10^{-3}U + 1.35 \times 10^{-8}U^2$ [$N = l_m/\lambda_{ct} = 1.18 \times 10^{16}(pl_c)_n\sigma_{ct} \approx 18$ for helium, since $(pl_c)_n = 1.3$ Torr cm].

In a discharge with slightly distorted field $E \approx$ const (Fig. 2, curves *2–4*), the electron beam production efficiency can be either greater or smaller than the ξ value for the anomalous discharge (curve *1*). As the parame-

ter *pd* grows, the efficiency drops (for a given *U*). The transition to a discharge sustained only by a low efficiency ion–electron emission mechanism takes place at greater *U* vales (Fig. 2, curves *4* and *5*).

In the approximation adopted for the anomalous discharge ($E = 0$ outside CF region), the electron beam production efficiency is independent of the *pd* value. Actually, the field outside the CF region can be (even in a quasi-stationary case) greater than that necessary for the escape of electrons [9]. Therefore, an increase in the *pd* value will result in that a greater part of *U* would drop behind the CF region and the discharge conditions would approach to those described by curve *4* (Fig. 2) with reduced efficiency. Therefore, curve *1* for an anomalous discharge is closer to the conditions of $pd \sim pl_m$.

A decrease in the beam current (by a factor of 1.6) observed by Kolbychev *et al.* [5] was attributed by these authors to a transition from photoelectron-stimulated to anomalous upon a change in the *d* value from 0.5 to 1 mm (all the other discharge parameters, including the total current $I_e + I_a$, remained unchanged). The above analysis provides a simple alternative explanation. Note that, as was pointed out in [2], "in the model, processes in the discharge gap may only affect the anode current and the total efficiency, but not the electron beam proper." For the photoelectron-stimulated open discharge model, the *d* value also cannot influence the compensation currents in the drift space (the related emission was suggested [6] to maintain the discharge). Moreover, the open discharge parameters are not affected when the compensation currents pass to the collector or the anode only or when these currents are absent (e.g., in the case when the collector is close to the anode).

The analysis would be incomplete without evaluating the role of ionization due to the fast atom bombardment. The coefficient of charge multiplication per ion, calculated using the cross sections taken from [7], is 0.15 for curve *1* in Fig. 1 and reaches unity for the anomalous discharge at $U \approx 40$ kV.

It should be noted that our calculations employed the data from [7] obtained for a gold cathode. However, the curves reported in [7] also well descried the data obtained with a copper cathode. Uttrerback and Miller [10] established that the results coincided for gold, brass, and tantalum cathodes. The results of the $U(j/p^2)$ measurements for Al, Mo, and steel cathodes reported in [8] also fit to the same curve. Therefore, the open discharge parameters are weakly dependent on the cathode material. This fact justified the use of data from [7] in our calculations.

4. The main conclusions of this study are as follows:

(i) The model of photoelectron-stimulated open discharge leads to serious unexplainable discrepancies with experiment.

(ii) The calculations and estimates of the efficiency of electron beam production well agree with the experimental data reported for both the open discharge and the high-voltage glow discharges of other types [11]. This fact confirms that the principal mechanism of the electron emission from cathode in these discharges is the cathode bombardment with atomic species.

(iii) The gas ionization by fast atom bombardment is significant at a voltage of several keV and becomes comparable with the electron-impact ionization in the near-anode plasma at a voltage equal to a few dozen kiloelectronvolts.

REFERENCES

1. P. A. Bokhan and A. R. Sorokin, Zh. Tekh. Fiz. **55** (1), 88 (1985) [Sov. Phys. Tech. Phys. **30**, 50 (1985)].
2. A. R. Sorokin, Pis'ma Zh. Tekh. Fiz. **21** (20), 37 (1995) [Tech. Phys. Lett. **21**, 832 (1995)].
3. A. R. Sorokin, Pis'ma Zh. Tekh. Fiz. **22** (13), 17 (1996) [Tech. Phys. Lett. **22**, 526 (1996)].
4. A. R. Sorokin, Zh. Tekh. Fiz. **68** (3), 33 (1998) [Tech. Phys. **43**, 296 (1998)].
5. G. V. Kolbychev and I. V. Ptashnik, Opt. Atmos. Okeana **12** (11), 1070 (1999).
6. G. V. Kolbychev, Izv. Vyssh. Uchebn. Zaved., Fiz. **11**, 84 (1999).
7. H. C. Hayden and N. G. Utterback, Phys. Rev. **135** (6A), 1575 (1964).
8. K. A. Klimenko and Yu. D. Korolev, Zh. Tekh. Fiz. **60** (9), 138 (1990) [Sov. Phys. Tech. Phys. **35**, 1084 (1990)].
9. V. P. Demkin, B. V. Korolev, and S. V. Mel'nichuk, Fiz. Plazmy **21** (1), 81 (1995) [Plasma Phys. Rep. **21**, 76 (1995)].
10. N. G. Utterback and G. H. Miller, Rev. Sci. Instrum. **32**, 1101 (1961).
11. M. A. Zav'yalov, Yu. E. Kreĭndel', A. A. Novikov, and L. P. Shanturin, *Plasma Processes in Technological Electron Guns* (Énergoatomizdat, Moscow, 1989).

Translated by P. Pozdeev